Torstein Bye

Capture Mechanisms of Mercury in Arctic Snow

Masteroppgave i Industriell kjemi og bioteknologi
Veileder: Øyvind Mikkelsen
Juni 2019

Masteroppgave

NTNU
Norges teknisk-naturvitenskapelige universitet
Fakultet for naturvitenskap
Institutt for kjemi

NTNU
Norwegian University of
Science and Technology

UNIS
The University Centre in Svalbard

Torstein Bye

Capture Mechanisms of Mercury in Arctic Snow

Masteroppgave i Industriell kjemi og bioteknologi
Veileder: Øyvind Mikkelsen
Juni 2019

Norges teknisk-naturvitenskapelige universitet
Fakultet for naturvitenskap
Institutt for kjemi

NTNU
Norwegian University of
Science and Technology

Summary

Elemental concentrations in snow sampled from different periods in Longyearbyen and Ny-Ålesund, Svalbard, have been determined. Samples were taken to investigate the effect of atmospheric mercury deposition events on surface snow in Svalbard, and to look into capture mechanisms of mercury during and after AMDEs. Fieldwork for this thesis was carried out in March 2019, and several data sets from other periods were provided for comparison. The aim of this project has been to find evidence supporting theories on AMDEs, look into capture mechanisms of mercury by natural organic matter in surface snow, and to investigate sources of common elements and pollutants found in Svalbard snow.

A highly varying amount of mercury was found in samples during the AMDE period, and the sampling days in Ny-Ålesund were found to be placed during depletion events by investigating a plot of GEM concentrations. Lower concentrations of mercury were found in snow sampled in other seasons. A principal component analysis revealed a clear seasonal variation in the elemental composition, whereas samples from March 2019 showed the most prominent deviation.

A relatively low amount of organic matter was found in Svalbard snow, and SUVA-values indicate the organic compounds found consist mainly of non-humic matter. No correlation was found between natural organic matter and mercury, which indicates that complexation of mercury with organics do not happen the way it does in aquatic systems such as effluent waters, or that the concentrations are too low for complexation to occur. A strong correlation found between mercury and chlorine and bromine could indicate mercury retention in snow by halogens. This could be a factor in the capture mechanisms of mercury in Svalbard snow.

Oppsummering

Elementkonsentrasjoner i snøprøver fra forskjellige perioder i Longyearbyen og Ny-Ålesund, Svalbard, har blitt bestemt. Prøvene ble tatt for å undersøke effekten av episoder av atmosfærisk uttømming av kvikksølv på overflatesnø på Svalbard, og for å se på fangstmekanismene av kvikksølv under og etter AMD episoder. Feltarbeid for prosjektet ble utført i mars 2019, og datasett fra feltarbeid i andre perioder ble hentet inn for sammenligning. Hovedobjektet i denne oppgaven har vært å finne bevis som støtter teoriene om AMD episoder, se på fangsmekanismene for kvikksølv med tanke på naturlig organisk materiale i overflatesnø, og undersøke kildene for elementer og forurensninger i snø fra Svalbard.

En fluktuerende mengde kvikksølv ble funnet under AMDE perioden i mars. Tall på GEM viste at det skjedde en rask nedgang i konsentrasjon av kvikksølv i gassform i løpet av feltarbeidsdagene. Andre perioder hadde lavere konsentrasjon kvikksølv i snøen. PCA viste at det var en klar tidsavhengigg variasjon i elementkomposisjon, der prøvene fra mars 2019 viste prominent forskjell fra de andre prøvetakingsperiodene.

Det var en relativ lav mengde organisk materiale i snø fra Svalbard, og SUVA-verdier indikerer at det organiske stoffet er stort sett ikke-humisk materiale. Det ble ikke funnet en korrelasjon mellom naturlig organisk materiale og kvikksølv, som kan indikere at kompleksering av kvikkølv med NOM ikke skjer på samme måte i snø som i vannsystemer med flytende vann, eller at konsentrasjonene er for små for at kompleksering skjer. Det ble funnet en sterk korrelasjon mellom kvikksølv, klor og brom, som kan indikere at halogener hindrer kvikksølv i å fordampe. Dette kan være en faktor i fangstmekanismene av kvikksølv.

Acknowledgements

This thesis is the final product of the Master's degree programme "Chemical Engineering and Biotechnology" with specialisation in Analytical Chemistry at Institute of Chemistry, Norwegian University of Science and Technology (NTNU). A lot of people who deserve acknowledgement were involved to realise this project. I would like to thank:

UNIS and Helena Reinardy, for accepting me as a guest master student at UNIS and giving me access to laboratory and practical facilities while performing field work in Longyearbyen;

Oda Siebke Løge and Ida Byrkjeland, for excellent assistance during fieldwork in Longyearbyen which made for an unforgettable snowmobile adventure in addition to sampling;

Norwegian Polar Institute, for granting working facilities and supplies for the fieldwork in Ny-Ålesund;

Kings Bay and the Ny-Ålesund community, for accommodation and facilitating to an amazing stay in Ny-Ålesund;

Syverin Lierhagen, for performing ICP-MS analyses and helping me with the freeze-drier;

Katrine Aspmo Pfaffhuber from NILU, for providing GEM data from the Zeppelin Observatory;

all my friends and family, for great support and motivation, and some social interactions in between the writing;

and of course my supervisor Øyvind Mikkelsen, for giving me the opportunity to travel and experience Svalbard, and for helping me with sampling, TOC/DOC and IC analysis, and excellent guidance and feedback throughout the whole process.

Figure 1: Sunset in Fardalen (Photo: Torstein Bye).

Contents

List of Tables

List of Figures

Abbreviations

GEM	=	Gaseous Elemental Mercury
AMDE	=	Atmospheric Mercury Depletion Event
RGM	=	Reactive Gaseous Mercury
PHg	=	Particulate Mercury
NOM	=	Natural Organic Matter
PCA	=	Principal Component Analysis
TOC	=	Total Organic Carbon
DOC	=	Dissolved Organic Carbon
POC	=	Particulate Organic Carbon
HA	=	Humic Acid
FA	=	Fulvic Acid
ICP-MS	=	Inductively Coupled Plasma Mass-Spectrometry
RSD	=	Relative Standard Deviation
PC	=	Principal Component
SUVA	=	Specific UV Absorption
ACN	=	Acetonitrile
MA	=	Monosaccharide Anhydride
UPLC	=	Ultra-Performance Liquid Chromatography
CEF	=	Crustal Enrichment Factor
LOD	=	Limit of Detection
LOQ	=	Limit of Quantification

Chapter 1

Introduction

Elevated levels of mercury have been observed in species of higher trophic levels in the Norwegian Arctic, such as polar bears and seals. High levels of mercury in animal tissue may display signs of toxic effects, such as changes in behaviour, reproduction rates, and population decline. Mercury is introduced into the food chain by a transformation of Hg^{2+}-species to methylated mercury. Methylated mercury is an organic mercury compound and is a bioavailable species of mercury, which means it's significantly more inclined to enter living organisms. Bioavailable mercury has a tendency of staying in the organism, causing bioaccumulation of the toxic compound, which will lead to biomagnification of the compound in the Arctic food chain. Ultimately, top predators will generate an elevated level of toxic mercury, which might lead to a change in behaviour in the animals and other signs of toxic effects. The elevated level of mercury in top predators and the indigenous Arctic people living off animals from a local source compared to subjects in other regions raise the question of why increased mercury pollution occur in the Arctic (Outridge et al., 2011).

Mercury monitoring in air, snow, and soil has revealed an increase in gaseous elemental mercury (GEM) in the Arctic atmosphere during the dark winter season, prior to a frequent fluctuation in GEM in the early spring. The decreases in GEM has been found correlating with an increasing concentration of divalent mercury in snow and soil (Skov et al., 2006). This is the result of a process called atmospheric mercury depletion events (AMDEs). It is thought mercury vapour Hg^0 is involved in photochemically initiated reactions resulting in reactive gaseous mercury (RGM). Ultimately, the mercury will be deposited onto the snow through dry or wet deposition mainly as a Hg^{2+}-species (Outridge et al., 2011; Schroeder and Munthe, 1998).

Despite this, little progress has been made considering the capture mechanisms of Hg^{2+}-species in snow. Suggested explanations for mercury capture are either chemical complexation with compounds in the snow or a mechanical capture through the thaw-freeze cycle, if not a combination of both. One of the key features of divalent mercury in terms of chemical transformation is its ability to form complexes with natural organic matter (NOM) (Gu et al., 2011). NOM is a term used to describe a mix of complex organic compounds found in the environment. NOMs are the decomposed remnants

of organisms and their waste products, modified by environmental processes. NOM consists of decomposed carbohydrates, fatty acids and proteins, which will result in different compounds with various functional groups, molecular weights and reactivities. The main fraction of aquatic NOMs consists of humic and fulvic acids, differentiated by aromaticity, oxygen and carbon content, and molecular weight. Humic acids contain a large variety of functional groups, including hydroxyls, carbonyls, aromatic and phenolic units (Sillanpää et al., 2015).

The metal binding of mercury to organic matter is in environmentally relevant conditions determined by functional groups (Aiken et al., 2011). GEM is relatively inert in this case, and will not undergo chemical complexation with organic matter on its own, and has little to no affinity to snow surfaces in general (Bartels-Rausch et al., 2008). Stephens et al. (2012) suggest that a series of photochemically initiated reactions involving halogen radicals is the initial pathway responsible for the oxidation of GEM, creating RGM-species (R. Stephens et al., 2012). A number of studies have examined saline ocean environments as the source of halogen atoms, and it is believed to be the primary source of halogen-atom precursors, such as Br_2, Cl_2, HOBr, and HOCl (Douglas et al., 2005; Kaleschke et al., 2004; Simpson et al., 2007a).

The aim of this Master's project is to investigate the atmospheric deposition of mercury in an Arctic environment and find evidence supporting articles concerning AMDEs. This dissertation seeks to explain the capture mechanisms of mercury in snow during AMDEs, and provide an overview of the current levels of elemental pollutants and their origin in Svalbard snow. Performing principal component analysis (PCA) and other statistical techniques on a dataset of elemental and molecular composition in Arctic snow may give great insight into environmental information. By looking into ICP-MS data of snow sampled on Svalbard at different seasons it is possible to investigate seasonal variations in mercury and other elements of interest.

The overall purpose is to contribute to new knowledge concerning atmospheric mercury and other long-range transported pollutants and their deposition and fate in the Norwegian Arctic, as well as contribute to the mapping of the current pollution state in the Norwegian Arctic. Knowledge of atmospheric deposition is part of the overall scientific understanding of mercury transport in the environment and biota, which is essential to the policy-making in international environmental legislation.

A series of research questions were formed to clarify the aim of this project: a) What is the average concentration of long-range transported elemental pollutants on surface snow in Svalbard? b) What is the concentration of NOMs in Svalbard surface snow, and is it possible to distinguish the different types of NOM in Arctic snow? c) How does mercury behave under the influence of natural organic matter? d) How do different long-range transported pollutants vary throughout different seasons?

The Arctic Monitoring and Assessment Program wrote an extensive report in 2011, "AMAP Assessment 2011 Mercury in the Arctic", on the state of the Arctic, summarising the work on mercury transport, pathways, deposition, fate, toxicity and topics regarding climate change affection on mercury transport (Outridge et al., 2011). Multiple studies have been conducted concerning the deposition and presence of mercury and other trace elements in Arctic and Norwegian soils and moss, and the deposition of

long-range transported mercury is well-known (Berg and Steinnes, 1997; Halbach et al., 2017; Steinnes et al., 2011). However, knowledge concerning the connection between deposited mercury and natural organic matter is limited, as well as the characterisation of NOMs present in Arctic snow.

Fieldwork concerning this thesis took place in March 2019, from 04.03.19-21.03.19, during the period when the sun returns to Svalbard after a period of darkness. 4 large snow samples were taken in Adventsdalen, Longyearbyen and 18 large snow samples in Brøggerdalen, Ny-Ålesund. 12 snow samples were located along a marine gradient, where the distance from the coast decreased between each sampling location. This was done to investigate the marine effects on mercury deposition. Increased levels of mercury have been found in marine and coast environments, which is a reason to believe the marine component affect the deposition (Steffen et al., 2008).

Research funds were granted for the fieldwork in Longyearbyen and Ny-Ålesund. The Research Council of Norway (NRC) funds up to 2 million NOK for projects concerning Svalbard and Jan Mayen by the Arctic Field Grant (AFG). This project is registered in Research in Svalbard Database with registration number and name RiS-ID 11155 ”Study of Capture Mechanisms of Mercury in Snow/Ice in the Arctic”.

Chapter 2

Theory

2.1 Svalbard

Svalbard is a group of islands in the Arctic Sea, located between 74° and 81° north latitude and 10° and 35° east longitude (see Figure 2.1) (Thuesen and Barr, 2009). The Svalbard archipelago is a part of the Kingdom of Norway, and has been under Norwegian sovereignty since 1925. Its terrain is dominated by glaciers, covering about $61\,\%$ of the surface land. There are relatively few sources of local pollution on Svalbard, whereas these are primarily mining activity and transport (Norwegian Enironment Agency - Norwegian PRTR, 2019). However, the fragile Svalbard ecosystem is susceptible to long-range transported pollution from both atmospheric and marine pathways.

Polar night is a natural phenomenon occurring North of the Arctic circle where there will be no daylight during the winter season. Areas north of the Arctic circle will experience this phenomenon, due to Earths rotation and axial tilt. In Longyearbyen, Svalbard, Polar night will last from October 26th, 2018 to February 16th, 2019. Due to the difference in northern latitude, the Polar night in Ny-Ålesund will last a little longer, from October 24th, 2018 to February 18th, 2019 (Aksnes, 2018).

Figure 2.1: Map of Svalbard (Norwegian Polar Institute, 2019a).

2.1.1 Longyearbyen

Longyearbyen is the administrative centre and largest settlement of Svalbard (see Figure 2.2). Together with Ny-Ålesund, the number of inhabitants is 2310 (Statistics Norway, 2018). Longyearbyen is located on the shoreline in Adventfjorden, which is on the southern part of Isfjorden. Local sources of pollution in Longyearbyen are relatively few and includes the Svalbard Airport (LYR), a waste incineration facility, an active coal mine - Mine 7, cruise and marine activities, and a coal power plant (Norwegian Enironment Agency - Norwegian PRTR, 2019). Snowmobile is a popular method for transportation, both for research activities, tourism and recreation, adding to the output of local pollution.

Figure 2.2: Map of Longyearbyen and Adventdalen (Norwegian Polar Institute, 2019b).

2.1.2 Ny-Ålesund

Ny-Ålesund is located on the northeastern side of Brøggerhalvøya by the shoreline to Kongsfjorden (see Figure 2.3). It is a small settlement with about 130 inhabitants during the summer and 30 inhabitants during the winter. Coal mining was the origin for settling at this location, but due to accidents the mining activities were terminated in 1963 (Barr, 2019). Now, Ny-Ålesund is a centre for international Arctic research of many scientific fields such as geology, biology, space science, and climate and environmental research. Polluting sources in Ny-Ålesund include the Ny-Ålesund airport, a small harbour, and snowmobile use. The local anthropogenic pollution is quite limited, which makes the location suited for investigating long-range transported pollutants. There are still remains of the open mines around the settlement, which may contribute some heavy metal pollutants and act as a local pollution source.

Figure 2.3: Map of Ny-Ålesund and Brøggerdalen (Norwegian Polar Institute, 2019c).

2.2 Mercury

Mercury has the symbol Hg and atomic number 80 and is the only metallic element in a liquid state under standard conditions. Mercury compounds are components in many common products such as batteries, lamps, cosmetics, pesticides, dental amalgam and barometers (Budnik and Casteleyn, 2018). Liquid mercury is used in artisanal and small-scale gold mining in South America, Africa and Asia. Other relevant point sources of emission of mercury include coal-fired power plants, smelting and roasting processes in non-ferrous metal production, and waste incineration facilities (UN environment, 2017a).

The main chemical species of mercury are elemental mercury (Hg^0), inorganic mercury (e.g. $Hg^{2+}, HgCl_2, HgBr_2$ ...), and organic mercury (e.g. methylmercury). Figure 2.4 presents the biogeochemical cycle of mercury and is a simple overview of the different sources, transport methods, and deposition methods of mercury. Mercury is a nonessential trace metal, and associated compounds are usually highly toxic depending on speciation, whereas methylated mercury has historically been of great concern for human and ecological health. Species of methylated mercury are bioavailable compounds able to accumulate in fatty tissue and biomagnify in the food chain. The vapour pressure of mercury at 0.26 Pa at 20°C and its relatively high atmospheric lifetime at 6 to 24 months makes the atmosphere a fitting medium for long-range transport of mercury (National Center for Biotechnology Information, 2019; Steffen et al., 2008; Outridge et al., 2011).

The Minamata disaster is an example of the toxic effects caused by industrial and careless release of methylmercury to the environment. Continuous release of industrial

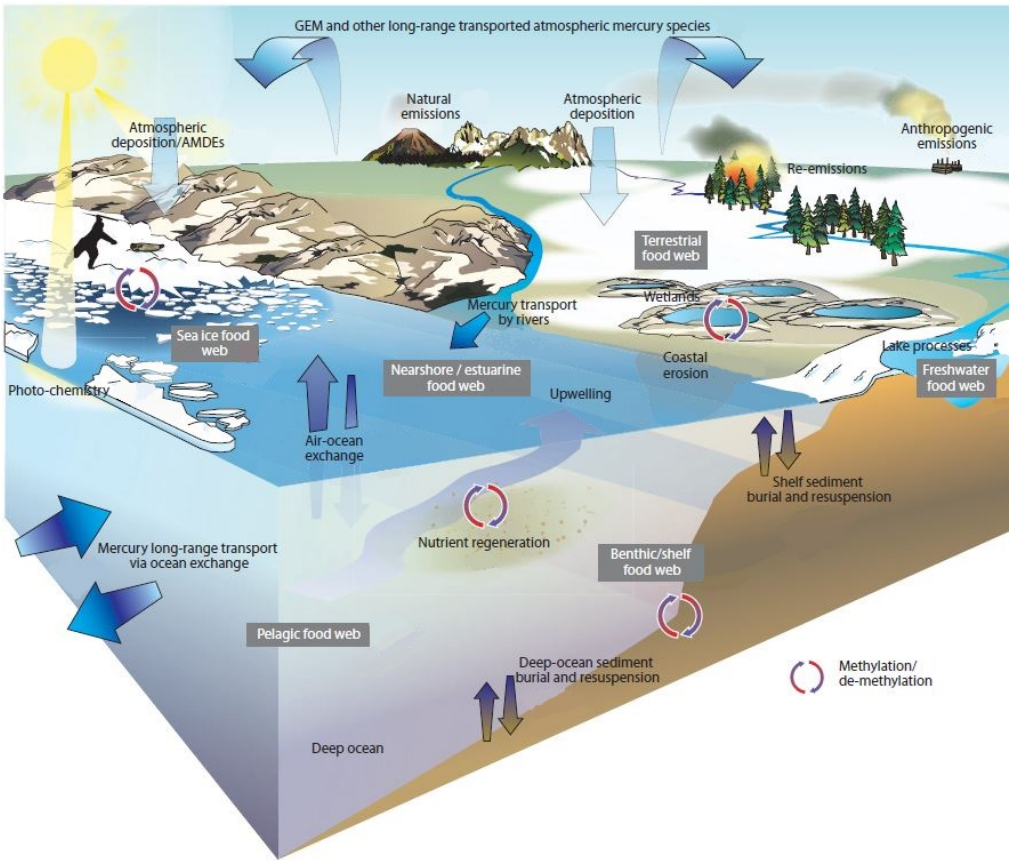

Figure 2.4: A simplified overview of the biogeochemical cycle of mercury in the environment (Outridge et al., 2011).

wastewater containing methylmercury from a chemical production facility in Minamata, Japan from 1932 to 1968 led to bioaccumulation of methylmercury in shellfish and fish in Minamata Bay. This resulted in mercury poisoning among the locals living off the nearby waters. Symptoms of mercury poisoning include muscle weakness, shaking, damage to vision and hearing, ataxia, paralysis, insanity, damage to offspring, coma and death (Budnik and Casteleyn, 2019).

The majority of the mercury found in organisms of higher trophic levels have been linked to mercury from anthropogenic sources. High levels of mercury in the Arctic environment poses a threat to indigenous people whose cultural heritage relies on hunting and fishing. Inuit, Yupik, and Iñupiat are examples of Arctic indigenous people who consume marine mammals such as seals, whales, and polar bears. AMAP assessments have linked marine mammals as a major source of dietary mercury exposure. Blood monitoring of Arctic communities have shown an elevated level of mercury in Arctic indigenous people, and a significant percentage of women have mercury levels exceeding the guideline values of US Environmental Protection Agency and Canada Health (Outridge et al., 2011).

The Minamata Convention on Mercury is a multilateral agreement created with the objective to 'protect human health and the environment from anthropogenic emissions and releases of mercury and mercury compounds' (UN environment, 2017b). The convention recognises the global concern of long-range transported mercury and its impact on human health and the environment. It also notes the exposure of long-range transported to the vulnerable Arctic ecosystem and indigenous communities (UN environment, 2017b).

2.2.1 Mercury Deposition & Re-emission

Mercury can appear as several different species in the various phases in the Arctic. Terms for common gaseous Hg-species are gaseous elemental mercury (GEM), Hg^0, and reactive gaseous mercury (RGM), whereas GEM is the main Hg-species in the atmosphere. RGM is generally produced through oxidation of GEM and is a term used to describe different gaseous molecules containing divalent mercury, Hg^{2+}. Hg^0 originates in both natural and anthropogenic sources, and approximately 98% of total mercury in the atmosphere will in most circumstances be Hg^0 (Outridge et al., 2011). Hg^0 has an insignificant affinity with surface snow (Bartels-Rausch et al., 2008), but RGM is more inclined to interact with surface snow. RGM may also adhere to airborne particles and create particulate mercury (PHg). Both RGM and PHg may deposit onto surface snow through either dry or wet deposition. Further pathways of deposited divalent mercury can be reduction to elemental mercury and reemission as GEM, or methylation of mercury to methylmercury. Figure 2.5 is a simplified illustration of the mercury cycling in the environment.

Considering the low affinity GEM has to surface snow, there must be a transformation of GEM to a more reactive species prior to the atmospheric deposition of mercury. A series of proposed mercury-related reactions involving oxidation of elemental mercury is presented in equation 2.1-2.5. The chlorine and bromine radicals linked to these re-

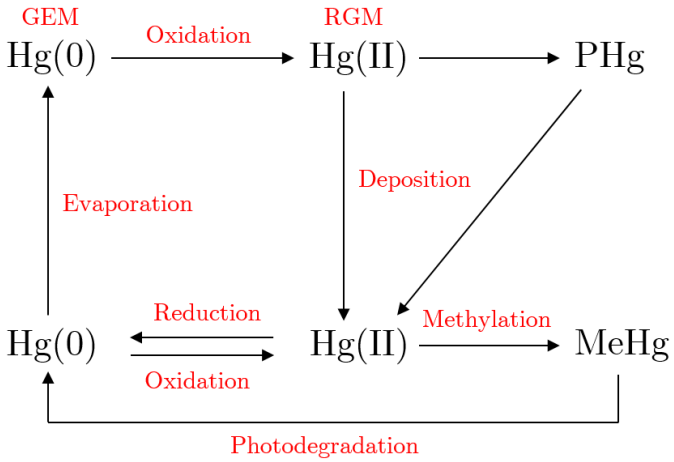

Figure 2.5: A simplified flow sheet of the mercury cycling in the Arctic (Hald, 2014).

actions are released during photochemical processes of sea salt (Simpson et al., 2007b). In the initial reaction, equation 2.1, GEM and Br will form a HgBr radical. This will stabilise after a collision with and inert particle, M, equation 2.2. However, the intermediate mercury bromide radical may instead destabilise and form elemental mercury and bromide, as shown in equation 2.3 (Donohoue et al., 2006).

$$\mathrm{Hg} + \mathrm{Br} \longrightarrow \mathrm{HgBr}^* \tag{2.1}$$
$$\mathrm{HgBr}^* + \mathrm{M} \longrightarrow \mathrm{HgBr} + \mathrm{M}\,(\mathrm{M}{=}\,\mathrm{He}, \mathrm{N_2}) \tag{2.2}$$
$$\mathrm{HgBr}^* \longrightarrow \mathrm{Hg} + \mathrm{Br} \tag{2.3}$$
$$\mathrm{HgBr} \longrightarrow \mathrm{Hg} + \mathrm{Br} \tag{2.4}$$
$$\mathrm{HgBr} + \mathrm{Y} \longrightarrow \mathrm{HgBrY}\,(\mathrm{Y}{=}\mathrm{Br}, \mathrm{Cl}, \mathrm{OH}, \mathrm{Br_2}, \mathrm{etc.}) \tag{2.5}$$

The mercury bromide molecule may also decompose as shown in equation 2.4, and form elemental mercury and bromide. Equation 2.5 is the reaction that will lead to formation of a stable RGM compound, which is thought to result in deposition of divalent mercury species. AMDEs have been reported to generate a mercury concentration up to $0.820\,\mu\mathrm{g\,L^{-1}}$ (Douglas et al., 2005), but other values typically range between $0.080\,\mu\mathrm{g\,L^{-1}}$ and $0.100\,\mu\mathrm{g\,L^{-1}}$ during AMDEs (Steffen et al., 2008).

Studies have shown that a large portion of mercury deposited onto Arctic snow during AMDEs is quickly volatilised and re-emitted and that approximately $80\,\%$ of newly deposited mercury from AMDEs is re-emitted during the span of 48 hours (Outridge et al., 2011). Lalonde et al. hypothesised in 2002 that this loss is caused by photoinduced reduction of divalent mercury species to GEM (Lalonde et al., 2002). Organic matter has also been linked to the re-emission of deposited mercury. Bartels-Rausch et al. (2010) have investigated the photochemically initiated reduction of divalent mercury species in presence of organic matter. There will be a continuous competition between the deposition and re-emission of mercury. The net flux of mercury in the snow-air interface will be affected by the presence of halogens, sun intensity, temperature, oxy-

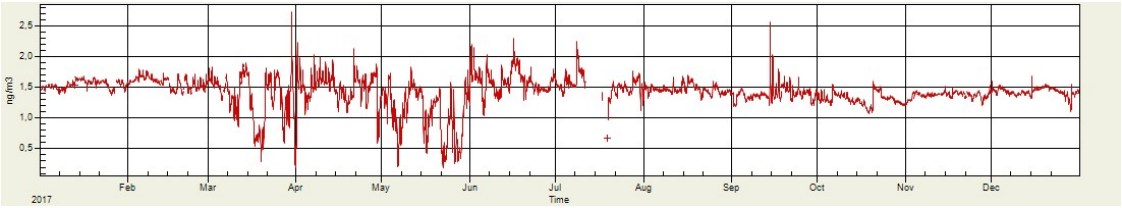

Figure 2.6: GEM concentrations data in 2017 from the Zeppelin Observatory (NILU, 2018).

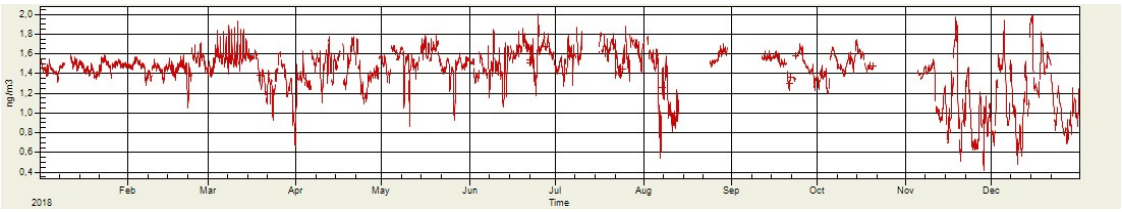

Figure 2.7: GEM concentrations data in 2018 from the Zeppelin Observatory (NILU, 2019).

gen content, acidity, and possibly natural organic matter (Bartels-Rausch et al., 2011; Lalonde et al., 2002; Outridge et al., 2011).

Figure 2.6 and 2.7 presents plots of the concentration of GEM at Zeppelin Observatory, Ny-Ålesund, in 2017 and 2018, respectively. There is an apparent fluctuation in GEM concentrations during springtime sun return in March both years, explained as deposition events of atmospheric mercury. Pan Wang (2015) reported general trends in weather conditions for AMDEs to occur: (i) a low temperature of $-23\,^{\circ}\mathrm{C}$ to $-12\,^{\circ}\mathrm{C}$; (ii) high relative humidity; and (iii) low precipitation (Wang, 2015). This is supported by findings of high concentrations of mercury in humid conditions and low temperatures (Douglas et al., 2005). Table 2.1 presents weather data for relevant sampling dates for the fieldwork performed in Ny-Ålesund, 15.03.19 - 22.03.19. The generally low temperature and precipitation levels might result in observable AMD events.

Table 2.1: Weather data for relevant sampling dates from Ny-Ålesund Observatory (Norwegian Meteorological Institute, 2019).

Date	Min. [°C]	Middle [°C]	Max. [°C]	Precipitation [mm]	Clouds
15.03.19	-18.3	-16.0	-14.6	0.0	Partly
16.03.19	-17.8	-15.4	-14.3	0.0	Partly
17.03.19	-17.0	-10.2	-6.5	0.0	Cloudy
18.03.19	-10.7	-8.1	-0.9	4.0	Cloudy
19.03.19	-14.5	-10.8	7.6	14.4	Cloudy
20.03.19	-8.5	-1.3	1.6	1.7	Cloudy
21.03.19	-7.4	-4.7	-1.7	3.8	Partly

2.3 Other Long-Range Atmospheric Transported Metals

Metals are found naturally in the environment, and are present in rocks, soil, plants and animals, and both natural and anthropogenic processes emit metals. Metals may take form as ions, vapours, salts or minerals, or bound as either inorganic and organic molecules, or adhered to airborne particles. While some metals are needed for biochemical processes such as photosynthesis and carrying oxygen in blood, other metals have no biochemical advantageous function and may pose a risk to the health of animals and people, even at trace amounts (Nilsson, 1997).

In the Arctic, natural sources of heavy metals include weathering of rocks. Anthropogenic sources will include mining, household heating, coal burning, metal processing, and burning of fossil fuels through transport vehicles and heating. The degree of anthropogenic influence in the Norwegian Arctic is relatively low. However, the Arctic is receiving heavy metals emitted in other regions of the northern hemisphere, e.g. China and Russia. These pollutants are carried on particles that stay suspended in the cold polar air (Nilsson, 1997).

Examples of elemental pollutants are cadmium (Cd), lead (Pb), selenium (Se), arsenic (As), copper (Cu), iron (Fe), aluminium (Al), chrome (Cr), manganese (Mn), zinc (Zn) and tin (Sn). There are great concerns regarding health and environment with respect to these elements, and the impact varies from element to element. Due to their toxicity, cadmium, lead, and mercury are often the focus in environmental research (Nilsson, 1997).

2.4 Natural Organic Matter

Natural Organic Matter (NOM) is a term for a complex mixture of degraded biological material. NOM molecules have a high molecular mass, and is formed through reactions between fragments of carbohydrates, proteins and lipids in an open environment. NOM consists primarily of carbon, oxygen and hydrogen, but sulphur and nitrogen may also be present depending on the source (Sillanpää et al., 2015).

There are few methods for determining natural organic matter, and no exact method for characterising NOMs in the environment. As stated above, NOM is not one component, but a general term for a wide range of organic compounds. This is the main obstacle in characterisation of NOM. Due to the complexity of this organic mixture, qualitative studies usually characterise the bulk NOMs.

Total organic carbon (TOC) is used to refer to the total amount of organic carbon, with carbon (C) as building block for the organic compounds. TOC in an aquatic system have two fractions: dissolved organic carbon (DOC) and non-dissolved particulate organic carbon (POC). The DOC concentration in a sample is measured by performing a TOC analysis on a filtrated sample ($0.45\,\mu\mathrm{m}$), as only dissolved components will pass the filter. The POC concentration can then be calculated by subtracting DOC from TOC. The DOC concentration in environmental waters vary greatly on the type of water. Some

groundwaters and seawater have as low as $0.5\,\mathrm{mg\,L^{-1}}$ DOC, whereas colored water from swamps may have over $30\,\mathrm{mg\,L^{-1}}$ DOC (Sharma et al., 2011).

Humic substance is a type of NOM, and is divided into three categories: humic acid (HA), fulvic acid (FA) and humin. The main fraction of humic substance in environmental waters is usually HAs. HA and FA are the compounds of interest with respect to complexation and chelation effects of heavy metals in aquatic systems. Both HA and FA are hydrophobic compound, however they both exist dissolved in water, constituting the main fraction of DOC. The main difference between these NOMs, is that HAs precipitate in an acidic environment with pH < 2, and FAs are dissolved under the whole pH range. In addition, FAs are somewhat smaller than HAs in molecular size, and has higher oxygen-to-carbon ratio (Sharma et al., 2011; Uyguner Demirel et al., 2007).

Humic substances may be assessed by the aromaticity of the contents in a water sample. This is done by measuring the absorbance of a filtered water ($0.45\,\mu\mathrm{m}$) in a UV-spectrometer at 254 nm. This specific wavelength will assess the density of electronic configuration associated with aromatic bonds. Equation 2.6 presents the calculation of specific UV absorbance (SUVA) of the water sample. The SUVA value is defined as the normalised UV absorbance with respect to the content of dissolved organic carbon and indicates the relative content of humic substance. A SUVA value greater than $4\,\mathrm{l\,mg^{-1}\,m^{-1}}$ may be interpreted as the water sample having a dominating fraction of humic substances, whereas a water sample with SUVA value below $2\,\mathrm{l\,mg^{-1}\,m^{-1}}$ is dominated by nonhumic material (Sharma et al., 2011).

$$\mathrm{SUVA} = \frac{\mathrm{UV}_{254}\ (\mathrm{cm^{-1}}) \times 100}{\mathrm{DOC}\ (\mathrm{mg\ l^{-1}})} \tag{2.6}$$

2.4.1 NOM - Metal Interactions

Complexation of divalent mercury with organic matter in aquatic systems is evident, and usually occurs in environments with higher concentrations of organic matter than Hg(II). As indicated previously, the Hg^{2+} - organic matter interaction will strongly affect mobility and bioavailability of mercury in the environment, by hindering reemission and altering solubility. Haitzer et al. (2002) studied the role of mercury to DOM concentration ratio, and found strong interactions at $1\,\mu\mathrm{g}$ Hg^{2+} per $1\,\mathrm{mg}$ of DOM. The reaction equation regarding metal binding to DOM is presented in equation 2.7, with a equilibrium constant of $K_{DOM'} = 10^{23.2\pm1.0}$ L kg^{-1} (Haitzer et al., 2002).

$$\mathrm{Hg^{2+}} + \mathrm{DOM} \rightleftharpoons \mathrm{HgDOM} \tag{2.7}$$

Studies have shown spectroscopic evidence of direct binding of Hg(II) to organic sulphur (S_{red}), and there is generally a high amount of sulphur groups in DOMs found in the environment. Haitzer et al. (2002) suggests that in the case of a Hg/DOM-ratio of $1\,\mu\mathrm{g}$ Hg^{2+} per $1\,\mathrm{mg}$ of DOM, mercury-thiol-binding will dominate, and that strong interactions between mercury and $DOMS_{red}$ are expected in a natural environment. An important note to be made is that even through snow is connected to aquatic systems, the knowledge of organic matter in snow is quite limited, and interactions and mechanisms may be different in snow and ice systems.

Other competing ligands for divalent mercury complexation in aquatic systems can be inorganic compounds, for example hydroxide molecules (OH^-) and chloride (Cl^-) (Han and Gill, 2005).

2.5 Molecular Tracers and Origin Specific Ratios

There is a significant link between mercury emissions and biomass burning (Fraser et al., 2017), as forests act as sinks in the biogeochemical cycle of mercury. About a half of the carbonaceous aerosols all over the world are emitted from biomass burning. Monosaccharide anhydrides (MAs) are examples of carbonaceous aerosols generated through combustion of cellulose and hemicellulose at temperatures over $300\,^{\circ}\mathrm{C}$. Levoglucosan ($C_6H_{10}O_5$, Figure 2.8) is a MA which can act as specific molecular tracers for biomass burning aerosols. You et al. (2016) have developed a method for determining levoglucosan in snow and ice at trace concentrations by using Ultra-Performance Liquid Chromatography (UPLC) (You et al., 2016). This will make it possible to pinpoint pollution sources of contaminants in the Norwegian Arctic. Major ions such as

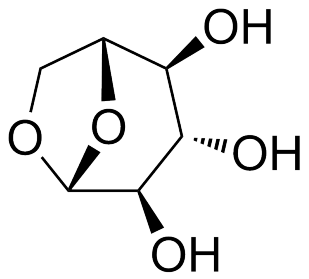

Figure 2.8: Molecular structure of levoglucosan.

Na^+, Ca^{2+}, $NH_4{}^+$ and $SO_4{}^{2-}$ are also tracers for aerosol sources. Similar to Cl^-, Na^+ is also a sea salt tracer, indicating influence of sea spray. Organic anions such as acetate ($[CH_3COO^-]$) and formate ($[HCOO^-]$) are also products of biomass burning, and may be used as biomass burning tracers in Arctic snow. $NO_3{}^-$ is an abundant anion in polar snow, and is a product of NO_X oxidation. Presence of $SO_4{}^{2-}$ indicate affection of anthropogenic combustion related emissions (Lai et al., 2017).

Presence of sulphur isotopes may be utilised to calculate isotope ratios to indicate sulphur origin. ^{32}S and ^{34}S have a natural abundance of $93.13\,\%$ and $4.29\,\%$, respectively. Equation 2.8 presents the calculation of sulphur isotope ratios. A $\delta S^{34/32}$ value between 3 and 6 indicate that the sulphur has anthropogenic origin, and a $\delta S^{34/32}$ value between 15 and 21 indicate marine sourced sulphur compounds (Barrie et al., 1994).

$$\delta S^{34/32} = \left(\frac{\left(\frac{^{34}S}{^{32}S}\right)_x}{\left(\frac{^{34}S}{^{32}S}\right)_{ref.}} - 1 \right) \tag{2.8}$$

Rock erosion produces dust which is distributed in the environment. Since the crustal composition is know, it is possible to calculate a crustal enrichment factor (CEF) to in-

dicate if an element might be of crustal or non-crustal origin. CEF is defined as the ratio of an element of interest to an abundant crustal element such as aluminium, normalised to the corresponding ratio of a known source. The equation for CEF is presented in equation 2.9 (Lai et al., 2017). UCC refers to the upper continental crust concentrations (Wedepohl, 1995). CEF values below 10 indicate crustal origin of the element, and a CEF values above 50 indicate non-crustal origin.

$$\mathrm{CEF} = \frac{(\mathrm{Element}/\mathrm{Aluminium})_{\mathrm{sample}}}{(\mathrm{Element}/\mathrm{Aluminium})_{\mathrm{UCC}}} \tag{2.9}$$

Chapter 3

Experimental

3.1 Svalbard Fieldwork

When characterising areas in the environment, it is generally impossible to examine its entirety. Therefore, it is necessary to take samples of the environmental phase under study, e.g. soil, water, or snow. The main goal during sampling is to remain the integrity of the sample, that is, no alteration or loss of interesting properties or parameters of the contents in the sample container. An environmental sample is susceptible to contamination during the whole process, from sampling to analysis. Personnel, sampling materials, method, preservation, environment and transportation will all present a risk of contaminating the sample. The sampling at Svalbard was performed according to NS-EN ISO 5667-14:2016 "Water quality - Sampling - Part 14: Guidance on quality assurance and quality control of environmental water sampling and handling" and NS-EN 1481-1997 "Water analysis - Guidelines for the determination of total organic carbon (TOC) and dissolved organic carbon (DOC)" with some modifications to cut expenses (International Organization for Standardization, 2016, 1997).

Snow sampled for elemental analysis by ICP-MS were sampled in metal free, high-quality polyethene tubes (50 ml). Snow sampled for organic analysis was sampled in clean low-density polyethylene ziplock bags (8000 ml) prior to melting and transferring the water to two 500 ml aluminium bottles for each sample site. The aluminium bottles were pre-washed with Milli-Q water (18.2 MΩ·cm, $1\,\mathrm{ppbTOC}$). Samples for elemental analysis was preserved with a few drops of nitric acid, HNO_3.

10 larger samples were collected for organic analysis, respectively 4 samples in Adventdalen, Longyearbyen and 6 samples in Brøggerdalen, Ny-Ålesund. Approximately 6 litres of snow was sampled in a low-density polyethylene ziplock bag, expecting to yield approximately 1 litre of water. After sampling, the snow was stored in a freezer prior to melting in room temperature and transfer to two 500 ml pre-washed aluminium bottles for each sample location.

Figure 3.1: Fresh snow, intense sun, and cold temperatures facilitates to atmospheric deposition of mercury, and creates excellent field trip conditions in Bayelva area, Ny-Ålesund. (Photo: Torstein Bye)

3.1.1 Sampling in Adventdalen, Longyearbyen 06.03.19

Snow for organic analysis was sampled at locations shown in Figure A.1 and Table A.1 (Appendix A). These locations are distributed along a marine gradient from Adventfjorden towards Adventdalen and further into Eskerdalen. The weather conditions during the sampling was poor, with reduced vision caused by fog and some snow. The temperature was ranging between $-10.8\,^{\circ}\mathrm{C}$ and $-28.4\,^{\circ}\mathrm{C}$, with a middle temperature of $-18.1\,^{\circ}\mathrm{C}$. There was a little wind, with an average wind speed of $3.4\,\mathrm{m\,s^{-1}}$ and maximum wind speed of $8.8\,\mathrm{m\,s^{-1}}$.

Snow mobiles were used for transportation between each sample location. The snow mobiles were parked and the snow was sampled around 20 meters from the snow mobiles and old snow mobile tracks. The snow sampled on Wednesday 06.03 was stored in a freezer until Wednesday 13.03, prior to melting in room temperature and transferring it to aluminium bottles. The samples were stored in room temperature for a week, prior to storage in a fridge (22.03.19).

3.1.2 Sampling in Brøggerdalen Ny-Ålesund 16.03.19 and 19.03.19

Snow sampled in the Bayelva area (16.03.19) is shown in Figure A.2 with coordinates in Table A.2 (Appendix A). The sun was shining all day, with just a few clouds, and the temperature was ranging between $-17.8\,^{\circ}\mathrm{C}$ and $-14.3\,^{\circ}\mathrm{C}$, with a middle temperature of $-15.4\,^{\circ}\mathrm{C}$. The wind conditions were gentle, with a middle wind speed at $4.3\,\mathrm{m\,s^{-1}}$ and a maximum wind speed at $9.7\,\mathrm{m\,s^{-1}}$. Snow was sampled in sun-rich areas. P5 is located on a river outlet to the ocean, and sample P6 and P7 were sampled at locations closer towards Brøggerdalen. Snow sampled by the Brøggerbreen area (19.03.19) is shown in Figure A.3 with coordinates in Table A.3 (Appendix A). The sampling was done the day after heavy snowfall and wind, supplying fresh surface snow. The sky was pretty clouded during the sampling, but there was little to no wind, and a temperature average of $-10.0\,^{\circ}\mathrm{C}$.

Two metal-free polypropylene tubes (50 ml) for ICP-MS analysis were also filled for each sample location. These were melted and acidified directly after the sampling. Samples for analysis of organics were stored in a freezer from from the respective sampling day until 20.03, prior to melting in room temperature and transferring the sample to pre-washed 500 ml aluminium bottles.

The 6 sample locations from 16.03.19 and 19.03.19 is presented in Figure 3.2.

3.1.3 Sampling in the Bayelva area, Ny-Ålesund 21.03.19

Snow was sampled with shorter intervals along a marine gradient 21.03.19. The sample locations are shown in Figure A.4 with coordinates in Table A.4 (Appendix A). The sun was shining with a few scattered clouds. The temperature was about $-5.0\,^{\circ}\mathrm{C}$ during the sampling, and there was a little to no wind.

Figure 3.3 presents the sampling locations of the dense sample locations. The sampling was performed on a flat field in the Bayelva area. Sample locations 1 to 10 are

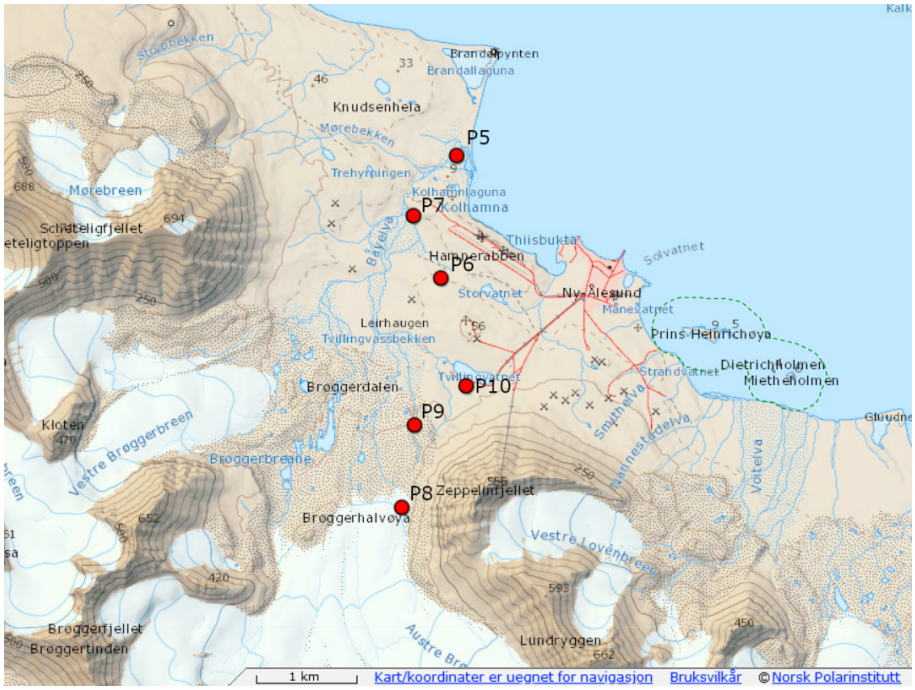

Figure 3.2: Sample locations of the 6 larger samples in Brøggerdalen and Bayelva, Ny-Ålesund.

sampled approximately 200 meters apart.

3.2 Sample and Analysis Overview

There were several different analytical approaches in mind during sampling, whereas the samples varied in sample volume, number of samples and sampling time. In this section, I will give clarification to the different sampling sets.

Firstly, four sampling periods were selected for this project: (1) sampling of snow in Ny-Ålesund prior to the AMDE period, November 2018; (2) sampling of snow in Longyearbyen with impending AMDEs, January and February 2019; (3) sampling of snow in Ny-Ålesund during the AMDE period, March 2019; and (4) sampling of snow in Longyearbyen and Ny-Ålesund after the AMDE period, May 2017. Sampling in period (1) was performed by my supervisor, Øyvind Mikkelsen. Sampling in period (2) was done by the UNIS students from the course ”AT-331 Arctic Environmental Pollution: Distribution and Processes”, supervised by Øyvind Mikkelsen. Sampling in period (3) was performed by my supervisor and me. Lastly, sampling in period 4 was performed by Master’s student Göksu Çelik and Øyvind Mikkelsen.

The second sampling period, just before the suns return to Svalbard, is divided into two sets: (i) 15 snow samples sampled January 2019 for ICP-MS analysis and (ii) 18 snow samples sampled February 2019 for ICP-MS analysis.

The third sampling period, during the AMDEs, is further divided into two sets: (a) 12 sampling locations for ICP-MS analysis from Ny-Ålesund and (b) 10 high volume samples (1.0 L) from Longyearbyen (4 samples) and Ny-Ålesund (6 samples) for organic

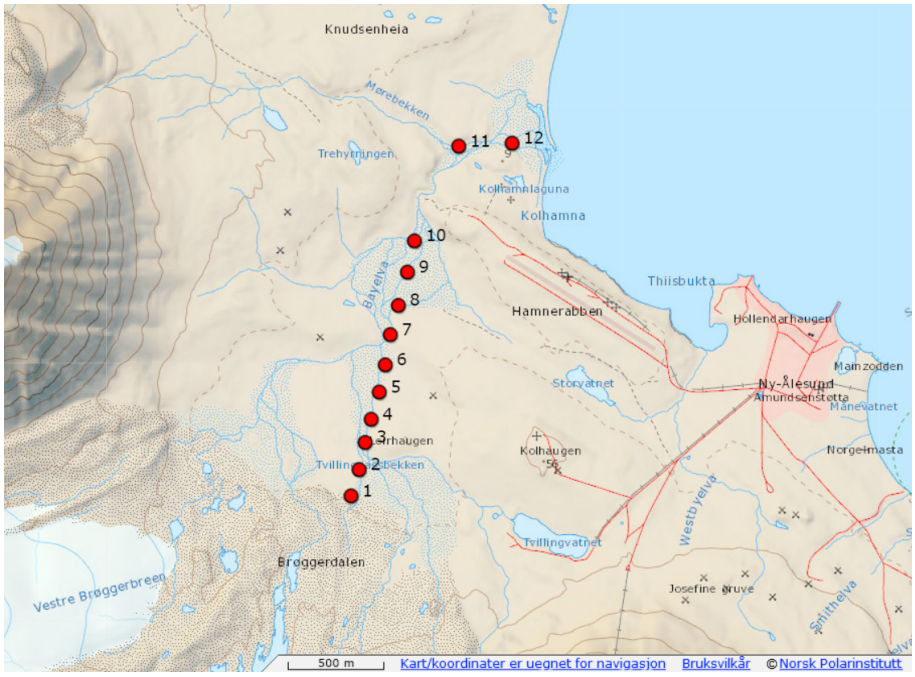

Figure 3.3: Sampling locations for investigating marine effect on mercury deposition.

analysis. When it is referred to 10 samples in this thesis, it is the 10 high volume samples from Longyearbyen and Ny-Ålesund during the AMDEs (period 3).

Both organic and inorganic compounds will be analysed in this thesis. A brief overview of the analysis techniques used to assess inorganic and organic compounds are presented in Figure 3.4 and 3.5, respectively.

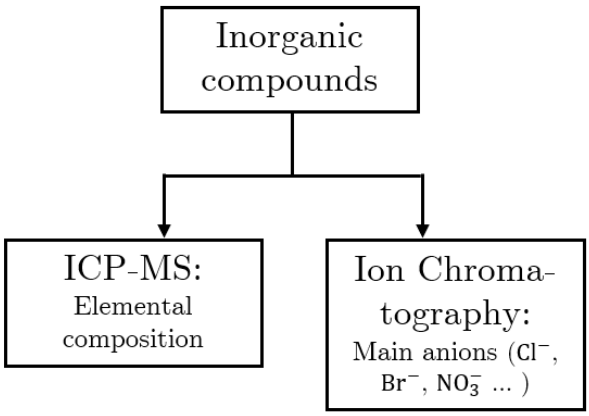

Figure 3.4: Overview of analysis techniques used to assess the inorganic compounds in Svalbard snow.

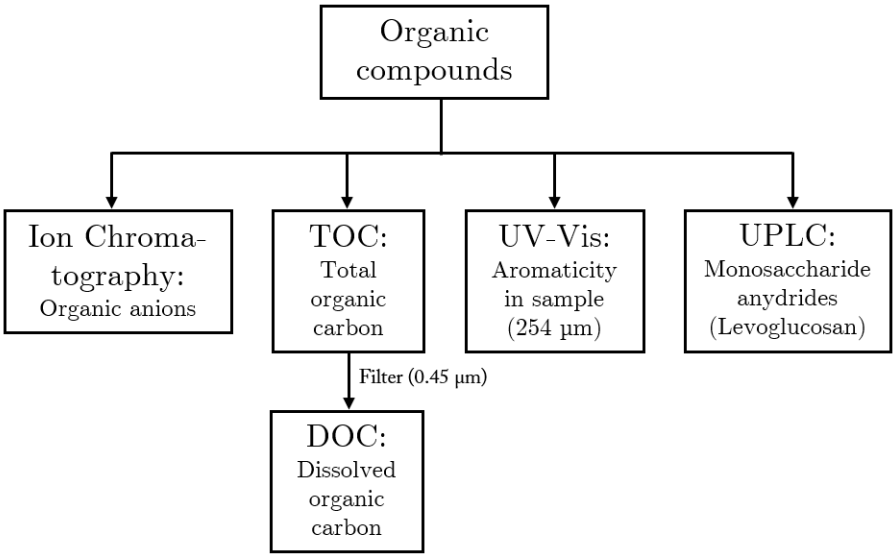

Figure 3.5: Overview of analysis techniques used to assess the organic compounds in Svalbard snow.

3.3 Inductively Coupled Plasma - Mass Spectrometry

Inductively Coupled Plasma - Mass Spectrometry (ICP-MS) is an analytical method for total element analysis. The method is a quantitative technique and used to determining the total amount of elements in a low-concentration sample matrix. ICP-MS is popular in environmental research considering its low analysis time, high accuracy and ability to quantify many elements at the same time with elimination of interference. It also has the advantage of low sample preparation prior to analysis, and samples are mainly aquatic. The method uses an induced coupled plasma source for atomising the sample, converting it into gas-phase atoms and ions. After atomisation of the sample, the ions are separated according to their respective mass-to-charge ratio prior to detection (Skoog et al., 2014).

Instruments available at Department of Chemistry, NTNU, are the Thermo Finnigan model Element 2 ICP-HR-MS instrument and an Agilent 8800 ICP-QQQ triple quadrupole instrument, offering precise analyses in a $\mathrm{mg\,L^{-1}}$ to sub-$\mathrm{ng\,L^{-1}}$ concentration range and determination of up to 73 elements.

Throughout this thesis, filtered samples will refer to filtering with a $25\,\mathrm{mm}$ syringe filter with a $0.45\,\mu\mathrm{m}$ polyethersulfone membrane, unless other is specified. Also, Milli-Q water will be used to refer to ultra-pure water filtered through a $0.22\,\mu\mathrm{m}$ filter with a conductance of $0.055\,\mu\mathrm{S}$ and a TOC-concentration of $1\,\mathrm{ppb}$.

Determination of elements of low concentration by ICP-MS is limited by matrix effects in the ion beam path through the ion optics and the mass spectrometer. Limit of detection is affected by high concentrations of other matrix elements which may suppress signals from other analytes.

3.4 UV-Vis

A UV mini 1240 spectrophotometer was used to measure both the UV absorbance at $\lambda = 254\,\mathrm{nm}$ for calculation of SUVA-values, and to investigate aromaticity in the sample by measuring over a range of UV-values. The UV-scans was performed over the range $190\,\mathrm{nm}$-$350\,\mathrm{nm}$.

UV-Vis analyses were measured in a cleaned quartz cuvette. Milli-Q water was used to clean the cuvette between each measurement, in addition to washing the cuvette with the respective sample solution.

3.5 Total Carbon and Freeze Drying

Total organic carbon (TOC) and dissolved organic carbon (DOC) in the samples was determined by a Teledyne Tekmar Torch Combustion TOC/TN Analyzer with a NDIR detector. Particulate organic carbon (POC) was calculated by the equations 3.1. TOC is measured by analysing an unfiltered sample, and DOC is measured by analysing a filtered sample.

$$\mathrm{POC} = \mathrm{TOC} - \mathrm{DOC} \tag{3.1}$$

TOC and DOC was measured on a sample twice: firstly as the pure sample, filtered and unfiltered, and secondly as a preconcentrated sample, filtered and unfiltered. The preconcentration method of choice was freeze-drying. Freeze drying is based on utilising a phase diagram of water to sublimate ice under vacuum (see Figure 3.6). This process will remove water and other volatile compounds from the sample, causing larger, nonvolatile molecules to remain in the sample container.

$250\,\mathrm{mL}$ from 10 samples was transferred to clean LDPE plastic bottles ($250\,\mathrm{mL}$) and frozen. These were freeze dried under a pressure of $0.94\,\mathrm{mbar}$ for 160 hours.

$25\,\mathrm{mL}$ MQ water was added to the freeze dried sample containers to dissolve the remains of the concentration process, before determining concentration of TOC in the samples. The samples was then filtered, before determining the concentration of DOC in the samples. The remaining sample solution was transferred to a clean quartz cuvette, and UV-absorbance at wavelength $\lambda = 254\,\mathrm{nm}$ was measured.

3.6 Ion Chromatography

A qualitative ion chromatography analysis of 10 samples from Longyearbyen and Ny-Ålesund was performed by the use of a Metrohm 940 Professional IC Vario ion chromatograph. The column used in the IC analysis was a Metrosep A supp 7 - 250/4.0 anion column, with a $3.6\,\mathrm{mM}$ Na_2CO_3 eluent. The analysis temperature was $45\,^{\circ}\mathrm{C}$, with a flow of $0.700\,\mathrm{mL/\,min}$.

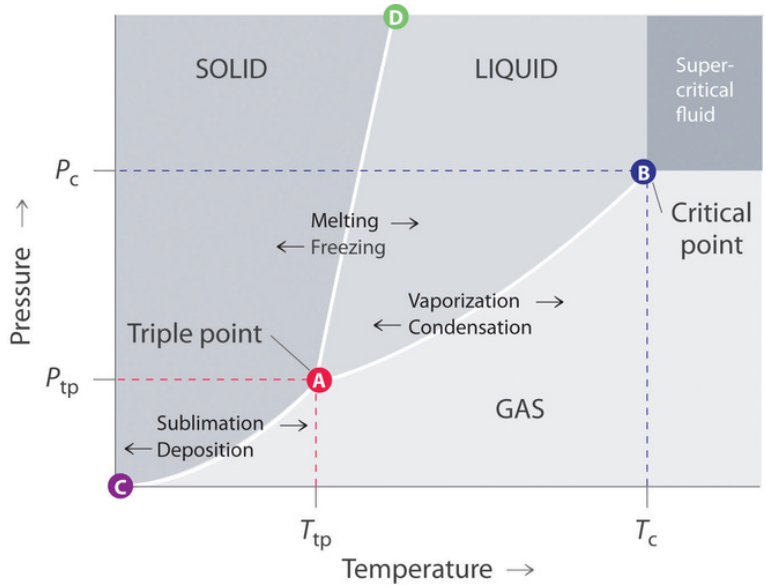

Figure 3.6: Phase diagram of water (Chemistry Libratexts, 2019). $P_{tp} = 6.11\,\mathrm{mbar}$ and $T_{tp} = 0.01\,^{\circ}\mathrm{C}$. The samples were sublimated at $P = 0.94\,\mathrm{mbar}$ and $T = -20.00\,^{\circ}\mathrm{C}$.

3.7 Detection of Levoglucosan by UPLC Analysis

The methodology used in this experiment is based on the work of You et al. (2016), determining levoglucosan at trace concentration levels using ultra high performance liquid chromatography coupled with a triple quadrupole mass spectrometer for detection (UPLC-MS) (You et al., 2016).

Chemicals used in this experiment is according to the article by You et al. (2016): HPLC grade water filtered at $0.20\,\mu\mathrm{m}$; HPLC grade acetonitrile (ACN) filtered at $0.20\,\mu\mathrm{m}$; HPLC grade ammonium hydroxide ($25\,\%$).

An aliquot consisting of $8\,\mathrm{mL}$ from 10 snow samples were filtered and transferred into cleaned low-density polyethylene containers ($10\,\mathrm{mL}$) sealed with a lid. The snow samples were frozen, prior to freeze-drying under near $0.80\,\mathrm{mbar}$ over $24\,\mathrm{h}$. $0.25\,\mathrm{mL}$ water was added to the sample container, before transferring the aliqout to a $2.00\,\mathrm{mL}$ sample vial. $0.75\,\mathrm{mL}$ ACN was added to each sample vial, adding up to a total sample volume of $1.00\,\mathrm{mL}$ in each sample. The sample vials were stored in a fridge at a temperature of $4\,^{\circ}\mathrm{C}$ for a week before analysis. Holding up the sample to light showed a high amount of sediments and particles, probably as a result of the concentration process. This is impossible to inject without resulting in clogging the instrumentation. Instead, the pure samples was filtered directly into $0.75\,\mathrm{mL}$ stands for the HPLC vials, and further sealed.

Analysis was performed by a UPLC system in reverse phase mode. The column used in this experiment, was a BEH Amide column ($2.1\,\mathrm{mm} \times 150\,\mathrm{mm}$, $1.7\,\mu\mathrm{m}$, Waters, Ireland). The mobile phase was a combination of ultra-pure water with $0.1\,\%$ NH_4OH (mobile A) and ACN (mobile B), with a gradient flow program for the UPLC system presented in Table 3.1.

Table 3.1: UPLC gradient flow program.

Time [min]	Mobile A / Mobile B	Flow rate [mL min^{-1}]	Curve
initial	65/35	0.15	6
0.25	65/35	0.15	6
0.50	50/50	0.15	9
7.00	50/50	0.15	6
8.00	65/35	0.15	6

3.8 Basic Statistics

3.8.1 Average

A simple tool for describing the contents of a larger set of data is to present the mean value for a variable. The mean value (or average) is calculated as presented in equation 3.2, where N is the total number of samples, and $\bar{X}$ is the average.

$$\bar{X} = \frac{\sum_{i=1}^{N} X_i}{N} \tag{3.2}$$

3.8.2 Standard Deviation

Standard deviation, σ, is a measure used to describe the variation of values in a dataset, and is calculated as presented in equation 3.3. A low standard deviation means most values are close to the average. Likewise, a high standard deviation indicates more values are farther from the average (Walpole et al., 2012).

$$\sigma = \sqrt{\frac{1}{N-1}\sum_{i=1}^{N}(X_i - \bar{X})^2} \tag{3.3}$$

A popular statistical measure in analytical chemistry is the relative standard deviation, RSD, which is used to express the repeatability and precision of a measurement. Unlike average and standard deviation, it is a dimensionless number, often expressed in percent as shown in equation 3.4.

$$RSD = \frac{\sigma}{\bar{X}} \cdot 100\% \tag{3.4}$$

3.8.3 Correlation

Correlation analysis sets out to measure the strength of the relation between two variables. The correlation is described by a single number called the correlation coefficient. The correlation coefficient, r, describes the linear association between the variables X and Y, and varies between -1 and 1. A correlation coefficient equal to either -1 or 1, $r = \pm 1$, occurs when there is a perfect linear relation between X and Y, whereas $r = 0$ occurs when there is no linear relation. A positive r can be directly interpreted to a

positive relationship between the two variables, X and Y. The opposite is true for the negative correlation coefficient, where there is a negative relation between X and Y, i.e. increasing value for X yields a decreasing value for Y, and vice versa (Walpole et al., 2012).

Calculation of the correlation coefficient r is presented in equation 3.8. The computation of r utilises the total corrected sum of squares of X and Y, presented in equation 3.5 - 3.7.

$$S_{xx} = \sum_{i=1}^{n}(X_i - \bar{X})^2 \tag{3.5}$$

$$S_{yy} = \sum_{i=1}^{n}(Y_i - \bar{Y})^2 \tag{3.6}$$

$$S_{xy} = \sum_{i=1}^{n}(X_i - \bar{X})(Y_i - \bar{Y}) \tag{3.7}$$

$$r = \frac{S_{xy}}{\sqrt{S_{xx}S_{yy}}} = \frac{\sum_{i=1}^{n}(X_i - \bar{X})(Y_i - \bar{Y})}{\sqrt{\sum_{i=1}^{n}(X_i - \bar{X})^2}\sqrt{\sum_{i=1}^{n}(Y_i - \bar{Y})^2}} \tag{3.8}$$

A correlation matrix is a useful way of presenting correlation between many variables in a data set. Correlation matrices were computed in RStudio with the *corrplot* package. A coding example for correlation matrix computation is presented in Listing 3.1.

```
library(corrplot)

# Load data
myData <- read.table("table.txt", header = T, row.names = 1)
summary(myData) # Check successful load

# Compute Correlation Matrix
G <- cor(myData)
corrplot.mixed(G)
```

Listing 3.1: Correlation matrix code example in R

3.9 Principal Component Analysis

Principal component analysis (PCA) is an unsupervised analysis method for visualising higher dimensional spaces. In chemometrics, unsupervised means the method is not used to predict a variable, but a method of comparing objects containing multiple variables. The method is based on creating linear combinations of the original variables. These linear combinations are called latent variables. This allows inspection of a higher dimensional space by projecting the data onto a lower dimensional space, which facilitates visualisation and interpretation.

Principal components (PCs) are latent variables that describe the new coordinate system onto which the samples are projected. The first PC (PC1) is created by rotation

of the original coordinate system in the direction of maximum variance. The second PC (PC2) is constructed by finding the maximum variance pointing orthogonal to PC1.

Two terms are used to describe the 2D PCA representation of a higher dimensional system - 'scores' and 'loadings'. 'Scores' can be defined as the coordinates of an object in the new axes. The term 'loadings' can broadly be defined as the how the variables in the data set are directed in the new coordinate system. Loadings are described by magnitude and direction. The direction of a loading can be used to interpret the correlation to another loading, as well as its effect on the PCs. The magnitude of a loading can be used to describe the relevance of said effect or correlation. Loadings pointing in the same direction are positively correlated, whereas two loadings forming a line around $180°$ with each other means they are negatively correlated. Loadings orthogonal to each other means the variables are independent of each other. In terms of interpretation, loadings can be used to: (a) detect how variables contribute to the different principal components; (b) finding clusters of correlated variables; (c) finding negatively correlated variables, and (d) finding clusters of unimportant variables for the model.

The definition of a principal component is the direction in multidimensional space corresponding to the maximum variance. The mathematical relationship between the original data, scores, and loadings is described in equation 3.9. This equation is valid if all principal components, A_{max}, are extracted. Throughout this chapter, $\mathbf{X}$ is the centred original data matrix, $\mathbf{T}$ is the scores matrix, $\mathbf{P}$ is the loadings matrix, and A is used to describe the number of the number of principal components extracted.

$$\mathbf{X} = \mathbf{T}\mathbf{P}^T \tag{3.9}$$

The number of PCs used to describe the model is generally lower than the number of PCs we are able to extract from the original data set. This introduces an additional component to equation 3.9, $\mathbf{E}_A$, which describes the residual matrix, i.e. the variance in the model not explained by $\mathbf{T}_A\mathbf{P}_A^T$. This PCA equation is presented in equation 3.10.

$$\mathbf{X} = \mathbf{T}_A\mathbf{P}_A^T + \mathbf{E}_A \tag{3.10}$$

Several plot types are used in PCA, for the cause of visualisation and explanation. The **loadings** plot is a visualisation of how the variables are oriented in the new coordinate system, whereas a **scores** plot is a visualisation of the objects in the new coordinate system. A **biplot** is a plot which combines the scores and the loadings for the principal components. Biplots offers visualisation of how variables affect the objects and vice versa (Alsberg, 2018).

Listing 3.2 presents a coding example for principal component analysis performed in RStudio. The package *ggplot2* is used to easily visualise samples with a specific **category** in the scores plot, by colouring the scores and drawing an ellipse around objects with a shared category.

```r
library(ggplot2)
library(FactoMineR)
library(factoextra)

# Load data
myData <- read.table("table.txt", header = T, row.names = 1)
summary(myData) # Check successful load

# Perform PCA
myPCA <- prcomp(myData[,n1:n2], scale = TRUE) # Scale to unit variance
fviz_eig(myPCA) # Scree plot
biplot(myPCA, scale = 0) # Biplot
fviz_pca_var(myPCA, col.var = "contrib", gradient.cols = c("#00AFBB",
    "#E7B800", "#FC4E07"), repel = TRUE) # Generate loadings plot with
     coloured contributions

# Extract PC scores
myPCA$x
myelements <- cbind(myData, myPCA$x[,1:2])
head(myelements) # Check

# Draw ellipse around scores in common category
ggplot(myelements, aes(PC1, PC2, fill = category)) +
  stat_ellipse(geom = "polygon", col = "black", alpha = 0.5) +
  geom_point(shape = 21)
```

Listing 3.2: PCA example in R

Chapter 4

Results and Discussion

4.1 Examining Elemental Composition in Arctic Snow by ICP-MS

Elemental composition were determined with ICP-MS by Syverin Lierhagen. 50 element concentrations were determined, but only 13 elements have been selected for further statistical analysis: manganese (Mn), cadmium (Cd), arsenic (As), mercury (Hg), zinc (Zn), nickel (Ni), chromium (Cr), lead (Pb), iron (Fe), aluminium (Al), copper (Cu), chlorine (Cl), and bromine (Br). These are selected based on theory on atmospheric mercury deposition events and elements linked to anthropogenic long-range transported pollutants.

Samples were collected in four different periods in time: (1) prior to AMDEs, during polar night, November 2018; (2) impending AMDEs, in the transition between polar night and sun return, January and February 2018; (3) during the AMDEs, right after sun return, March 2019; and (4) after AMDEs, during midnight sun, April and May 2017. These will be referred to as period 1 - 4 in results and discussion. The first research question set out to investigate the average concentrations of some elemental pollutants in Svalbard snow. These are summarised in the ICP-MS data tables 4.1 - 4.4. Unfiltered samples are removed from the data sets to yield a homogeneous data set with similar preprocessing methods.

P5 - P10 (Ny-Ålesund) from the 10 larger samples were used to assess the amount of particulate compounds in polar snow. These were analysed by ICP-MS as both filtered and unfiltered samples, allowing investigation of both the dissolved and particle bound elements. Table 4.5 presents a summary of the element concentration of particulates in sample P5 to P10 from Ny-Ålesund (period 3). The particulate concentrations were calculated by subtracting the values in filtered samples (dissolved fraction) from the values in the unfiltered samples (total fraction), as seen in equation 4.1.

$$c_{\text{particulates}} = c_{\text{unfiltered}} - c_{\text{filtered}} \tag{4.1}$$

Some tabulated values are negative, resulting from either filter contamination or high

Table 4.1: ICP-MS results for period 1, November 2018 ($N = 19$). All values have the unit [$\mu g\, L^{-1}$].

Element	Average	Median	Min	Max	Standard deviation
Cd	8.10×10^{-4}	7.10×10^{-4}	1.87×10^{-4}	22.90×10^{-4}	5.49×10^{-4}
Hg	10.1×10^{-3}	9.10×10^{-3}	2.17×10^{-3}	2.99×10^{-3}	5.89×10^{-3}
Pb	12.30×10^{-4}	11.60×10^{-4}	2.53×10^{-4}	32.30×10^{-4}	8.92×10^{-4}
Al	0.986	0.468	0.228	7.150	1.540
Cl	1.76×10^{3}	0.297×10^{3}	201×10^{3}	11.7×10^{3}	3.67×10^{3}
Cr	0.0285	0.0234	0.0052	0.0835	0.0203
Mn	0.505	0.069	0.018	3.760	1.140
Fe	0.512	0.385	0.171	1.620	0.431
Ni	0.0210	0.0135	0.0049	0.0746	0.0178
Cu	0.0474	0.0339	0.0207	0.2200	0.0457
Zn	5.57	5.43	1.57	9.25	2.33
As	13.40×10^{-3}	14.5×10^{-3}	0.00×10^{-3}	32.30×10^{-3}	9.32×10^{-3}
Br	6.2	1.5	1.0	39.5	12.0

Table 4.2: ICP-MS results for period 2, January and February 2019 ($N = 25$). All values have the unit [$\mu g\, L^{-1}$].

Element	Average	Median	Min	Max	Standard deviation
Cd	11.0×10^{-3}	9.92×10^{-3}	1.42×10^{-3}	33.10×10^{-3}	6.67×10^{-3}
Hg	4.64×10^{-3}	4.62×10^{-3}	0.53×10^{-3}	1.41×10^{-3}	3.17×10^{-3}
Pb	0.159	0.142	0.019	0.410	0.117
Al	13.50	4.50	0.849	174.00	35.40
Cl	12.3×10^{3}	11.0×10^{3}	2.40×10^{3}	27.8×10^{3}	7.45×10^{3}
Cr	0.0686	0.0443	0.0147	0.2010	0.0544
Mn	5.230	1.600	0.115	31.600	8.710
Fe	5.630	3.610	0.881	36.800	7.360
Ni	0.314	0.139	0.046	3.620	0.704
Cu	1.500	0.519	0.152	13.900	2.970
Zn	19.40	11.30	1.02	95.70	20.60
As	0.125	0.055	0.007	1.170	0.232
Br	40.0	36.6	8.3	95.2	24.6

Table 4.3: ICP-MS results for period 3, March 2019 ($N = 18$). All values have the unit [$\mu g\,L^{-1}$].

Element	Average	Median	Min	Max	Standard deviation
Cd	14.60×10^{-3}	14.10×10^{-3}	3.73×10^{-3}	28.50×10^{-3}	7.72×10^{-3}
Hg	7.41×10^{-3}	4.16×10^{-3}	0.00	20.50×10^{-3}	7.34×10^{-3}
Pb	0.367	0.351	0.065	0.709	0.239
Al	0.727	0.941	0.534	3.800	0.727
Cl	36.8×10^{3}	34.7×10^{3}	3.53×10^{3}	74.3×10^{3}	25.6×10^{3}
Cr	0.0373	0.0248	0.0063	0.1020	0.0280
Mn	0.939	0.487	0.147	6.320	1.400
Fe	1.680	1.200	0.344	6.760	1.640
Ni	0.0335	0.0314	0.0086	0.0989	0.0207
Cu	0.1230	0.0955	0.0144	0.4450	0.0974
Zn	13.90	14.10	5.57	23.20	5.60
As	0.0950	0.0909	0.0056	0.2200	0.0593
Br	149.0	136.0	11.8	288.0	95.9

Table 4.4: ICP-MS results for period 4, April and May 2017 ($N = 39$). All values have the unit [$\mu g\,L^{-1}$].

Element	Average	Median	Min	Max	Standard deviation
Cd	7.15×10^{-3}	7.77×10^{-3}	0.80×10^{-3}	13.70×10^{-3}	3.72×10^{-3}
Hg	1.95×10^{-3}	1.84×10^{-3}	0.00	4.90×10^{-3}	1.37×10^{-3}
Pb	0.0765	0.0551	0.0129	0.2420	0.0662
Al	1.630	0.956	0.401	7.460	1.560
Cl	6.26×10^{3}	5.57×10^{3}	1.09×10^{3}	3.07×10^{4}	5.24×10^{3}
Cr	0.0257	0.0192	0.0042	0.1140	0.0229
Mn	4.400	1.010	0.099	52.900	10.800
Fe	1.450	0.799	0.341	6.270	1.530
Ni	0.090	0.059	0.004	0.742	0.129
Cu	0.477	0.179	0.033	4.520	0.870
Zn	3.580	2.970	0.913	10.700	2.160
As	0.0260	0.0217	0.00476	0.0717	0.0159
Br	12.2	7.4	3.5	60.9	12.2

Table 4.5: Element concentrations for particulate compounds in sample P5 - P10 from Ny-Ålesund (16.03.19 and 19.03.19), calculated by subtracting the filtered samples from the unfiltered samples. All values have the unit [$\mu g\,L^{-1}$].

Element	Average	Median	Min	Max	Standard deviation
Cd	1.36×10^{-3}	0.89×10^{-3}	0.00	4.56×10^{-3}	1.74×10^{-3}
Hg	1.21×10^{-3}	0.02×10^{-3}	N/A	9.24×10^{-3}	4.01×10^{-3}
Pb	0.301	0.166	0.053	1.000	0.358
Al	72.30	41.60	9.02	255.00	92.40
Cl	601.0	242.0	42.1	2370.0	893.0
Cr	0.166	0.078	0.021	0.666	0.249
Mn	2.400	1.930	0.151	6.030	2.170
Fe	128.0	85.9	15.6	425.0	151.0
Ni	0.144	0.113	0.010	0.448	0.157
Cu	0.167	0.069	0.002	0.723	0.276
Zn	N/A	N/A	N/A	N/A	N/A
As	0.0315	0.0312	N/A	0.1320	0.0587
Br	9.77	10.45	N/A	22.66	8.84

analytical uncertainty from ICP-MS results. The negative values were set to N/A, as a negative concentration is impossible. As the filtering process removes certain parts of the total contents, the concentration of an element in the filtered sample should always be equal or less than the concentration of en element in the unfiltered sample, unless the filter itself is a source of contamination. The concentration of particulate zinc is negative for all samples, which may be a result of filter contamination. As acidification and filtering is the only preprocessing needed for ICP-MS analysis, there is no other source for increased zinc in filtered samples. The analysis of zinc is quite precise, as all samples have a low relative standard deviation ($< 8.0\,\%\mathrm{RSD}$). Elemental analysis of particulate arsenic show some negative values. This may be a result of analytical noise, as the raw data of arsenic have high RSD% ranging between $24.7\,\%$-$100.0\,\%$.

Mercury raw data shows a high relative standard deviation (RSD%) as most of the samples are close to or below the quantification detection limit ($5.00 \times 10^{-3}\,\mu g\,L^{-1}$). Table 4.5 shows low degree of particulate formation of mercury, with the highest particulate mercury concentration of $9.24 \times 10^{-3}\,\mu g\,L^{-1}$. The sample with the highest concentration of particulate mercury is P5, which is the sample closest to the ocean. This could be a result of marine transported mercury particulates, deposition of particulate mercury, PHg, or a result of atmospheric mercury deposition on the marine boundary followed by adhesion to particles. Sample P5 also have high chlorine and bromine concentration. This is better visualised by normalising and plotting the particulate element values, presented in Figure 4.1.

Inspection of Figure 4.1 shows a high correlation between mercury, chlorine, bromine and cadmium, which is confirmed by the correlation matrix in Figure 4.3 ($r_{\text{Cd/Hg}} = 0.82$, $r_{\text{Cd/Cl}} = 0.81$, $r_{\text{Cd/Br}} = 0.68$, $r_{\text{Hg/Cl}} = 0.97$, $r_{\text{Hg/Br}} = 0.64$, $r_{\text{Cl/Br}} = 0.79$). The rest of

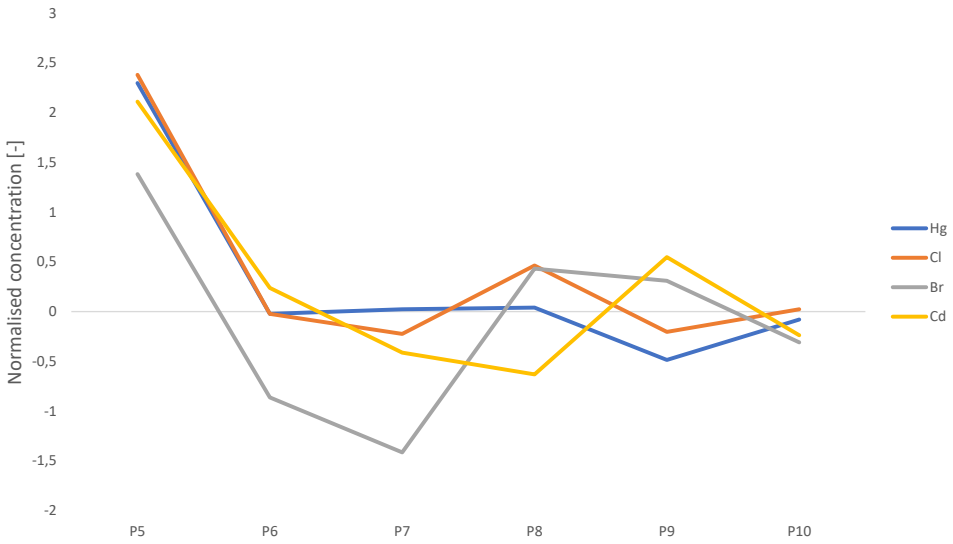

Figure 4.1: Normalised particulate concentrations of the correlating element; Cd, Hg, Cl, and Br, in sample P5 to P10.

the samples have no sign of particulate mercury, and the unfiltered and filtered sample both have relatively low concentration of mercury, ranging between 'not detected' to $5.00 \times 10^{-3}\,\mu g\,L^{-1}$.

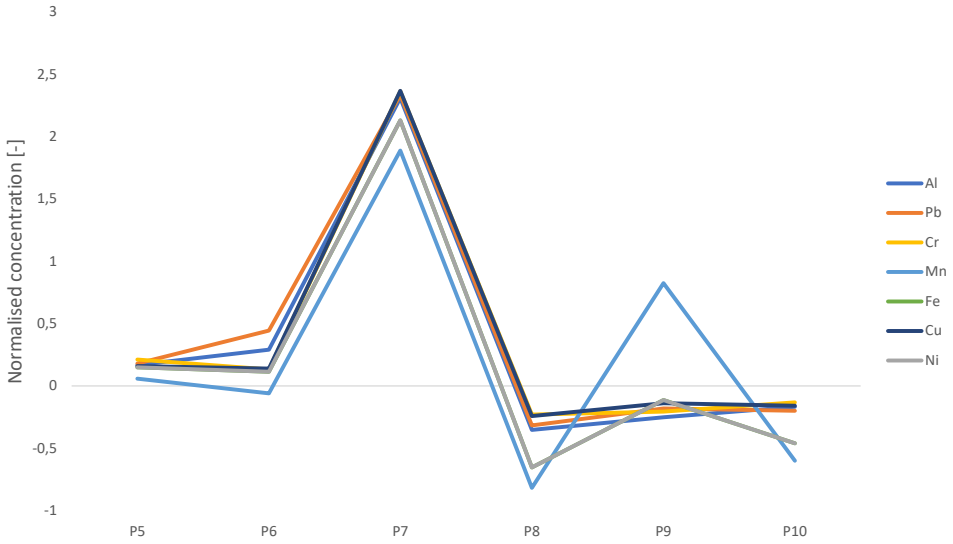

Figure 4.2: Normalised particulate concentrations of the correlating elements; Al, Pb, Cr, Fe, Ni, Cu in sample P5 to P10.

Inspection of the correlation plot in Figure 4.2 and 4.3 shows a high correlation between aluminium, lead, chromium, manganese, iron, copper and nickel, with 21 correlation factor describing their relationships with values ranging between 0.81 and 1.00. Zinc and arsenic were removed from this data set as there is high analytical uncertainty in the arsenic concentration and possible contamination of zinc. The high correlation between Al, Pb, Cr, Mn, Fe, Ni, and Cu is presumably due to a common origin for these elements. This indicates that the elements lead, nickel, aluminium, chromium, and copper are present on Svalbard snow in Ny-Ålesund mostly due to products of rock erosion. This is supported by the low and negative correlation coefficient these heavy metals have with marine halogens. However, with a small sample size of $N = 6$ these results need to be interpreted with caution.

Crustal enrichment factors were calculated for the samples in period 3, to further investigate the source of the metals found on the snow in Ny-Ålesund. A box plot containing CEFs for cadmium, mercury, lead, chromium, manganese, iron, nickel, copper, zinc and arsenic is presented in Figure 4.4. Cadmium, mercury, zinc, and arsenic show a considerably distinction from the other elements, indicating a non-crustal origin. This

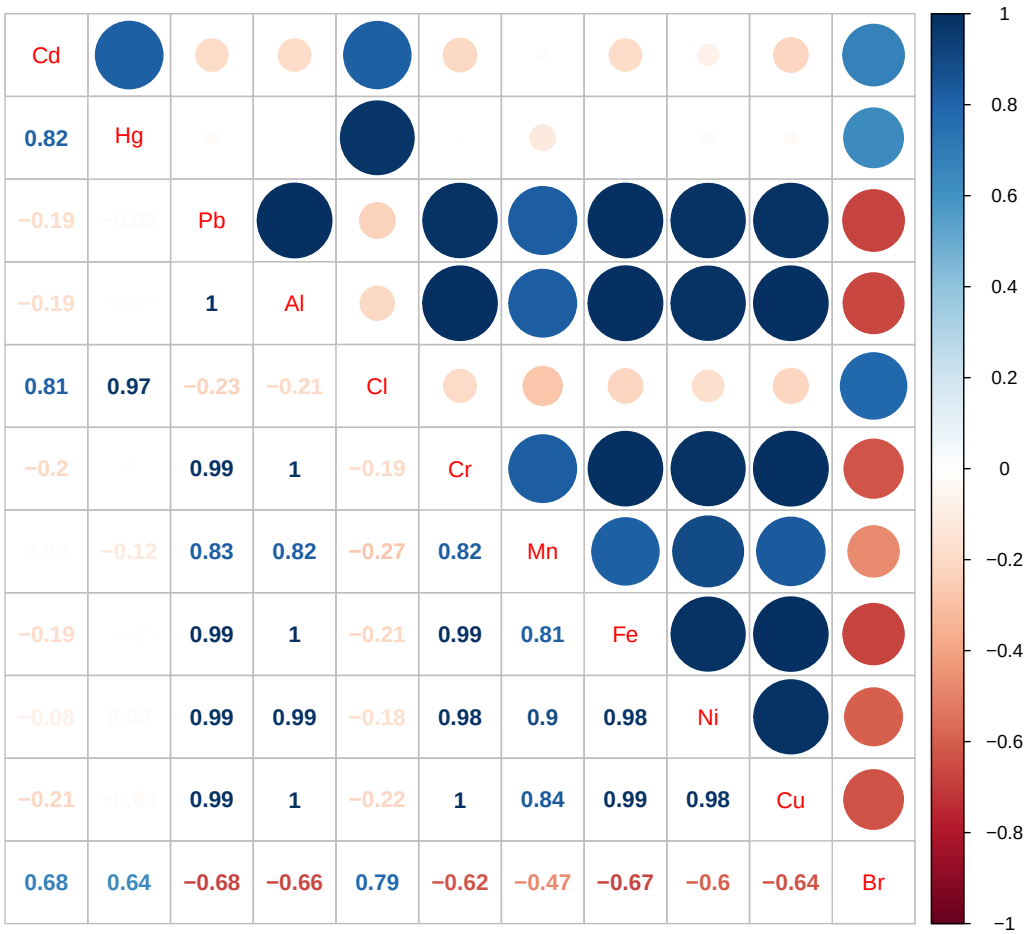

Figure 4.3: Correlation matrix of particulate elements in sample P5-P10 in period 3.

further supports the theory of atmospheric deposition of mercury.

Lead also shows some high CEF values. Investigation of the raw data shows that lead has higher CEF values in the filtered samples and a considerably lower enrichment factor in the unfiltered samples. This strongly indicate that the lead existing as particulates is of crustal origin. Chromium, manganese, iron, nickel and copper show relatively low CEF values, which indicate crustal origin of all these elements during this time period.

4.1.1 Investigating Marine Effects

Statistical analyses were used to assess the effects of marine halogens on mercury content in the snow. This section will mainly focus on the data set containing 12 samples along the marine gradient, sampled 21.03.19. Here, sample **G1** - **G12** corresponds to sample 1-12 in Figure 3.3, whereas the distance between the sample location and the shoreline will decrease with an increasing sample number.

Figure 4.5 presents the concentration of mercury in snow sampled along a marine gradient in Ny-Ålesund, compared to the quantification detection level of $0.005\,\mu g\,L^{-1}$. The concentrations show no direct correlation with distance to the shoreline. However, this does not necessarily mean mercury is independent of marine effects. The high concentrations present in sample G3 - G7 and G9 clearly demonstrates that there is some deposition of mercury occurring in the Arctic area during the springtime sun return.

Figure 4.6 presents the normalised concentrations of mercury, chlorine and bromine along the marine gradient. The halogens have marine origin, and are highly correlated with a correlation coefficient of $r_{\text{Cl/Br}} = 0.996$. Mercury shows a similar pattern, and have correlation coefficients with chlorine and bromine of $r_{\text{Hg/Cl}} = 0.843$ and $r_{\text{Hg/Br}} = 0.849$, respectively.

The fluctuating levels of mercury (Figure 4.5) in the Ny-Ålesund snow is, as previously mentioned, highly correlated with chlorine and bromine. This supports the theory of halogen reactions causing mercury deposition. However, mercury reemission is also occurring as mentioned in the theory. One would expect mercury to be less correlated with halogens if there is a rapid reemission of mercury occurring, but the high correlation between mercury and halogens, having both the deposition and reemission processes in mind, is indicating that the halogens present in the snow is retaining mercury reemission. The potential capturing of mercury this way could be a factor for high release of snowbound mercury to the marine environment during the springtime snowmelt.

There is no obvious trend line in marine originating halogens with respect to the distance from the ocean. The deposition of halogens is probably affected by many pathways, including the creation of marine frost flowers in which deposits halogens on surface snow. This could only be a gradual deposition if the wind were constantly directed towards the land, but that is not the case. Different wind direction is one of the many processes which affects elemental distribution on surface snow.

However, these finding may be somewhat limited by a relative short sampling distance ($1.7\,\text{km}$). The sampling was performed in an marine area where mercury deposition and reemission occur frequently, hence the large variation in mercury concentrations. A longer sampling distance could reveal an overall increase of mercury deposition

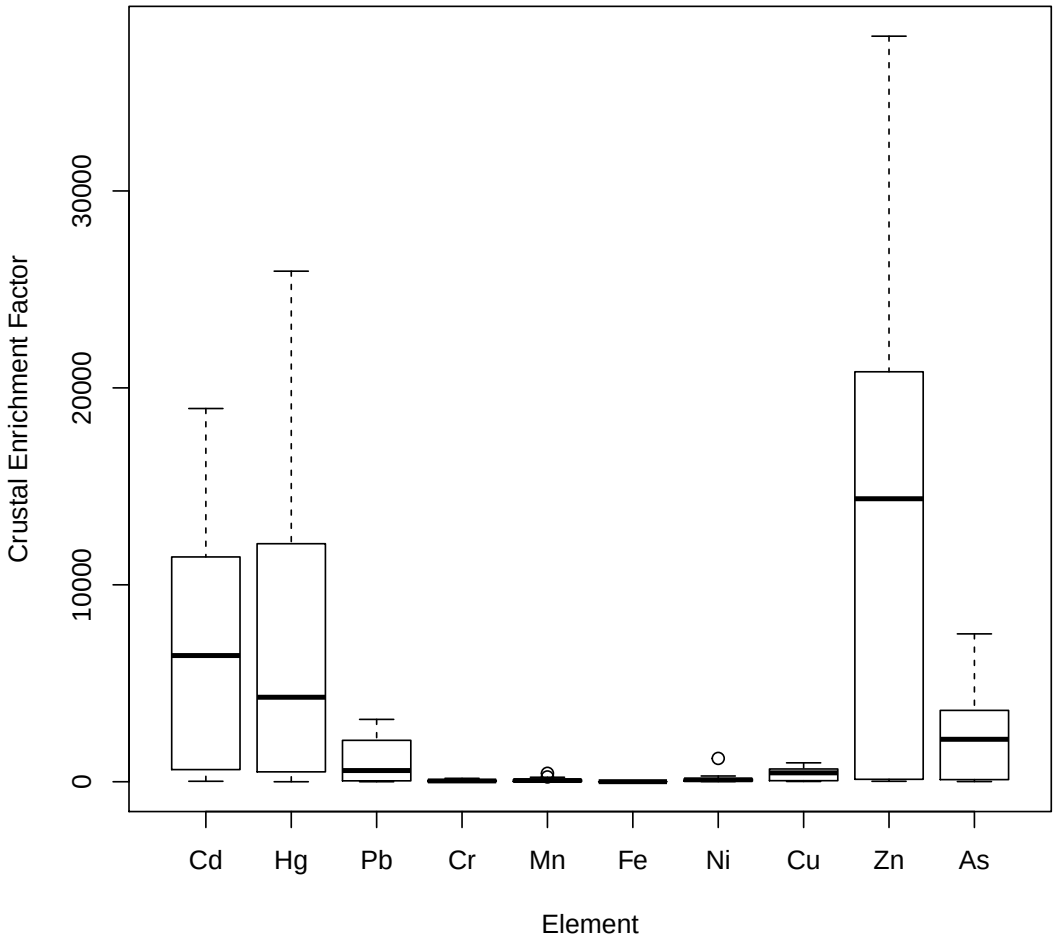

Figure 4.4: Crustal enrichment factors for elements found in the snow in March 2019, Ny-Ålesund.

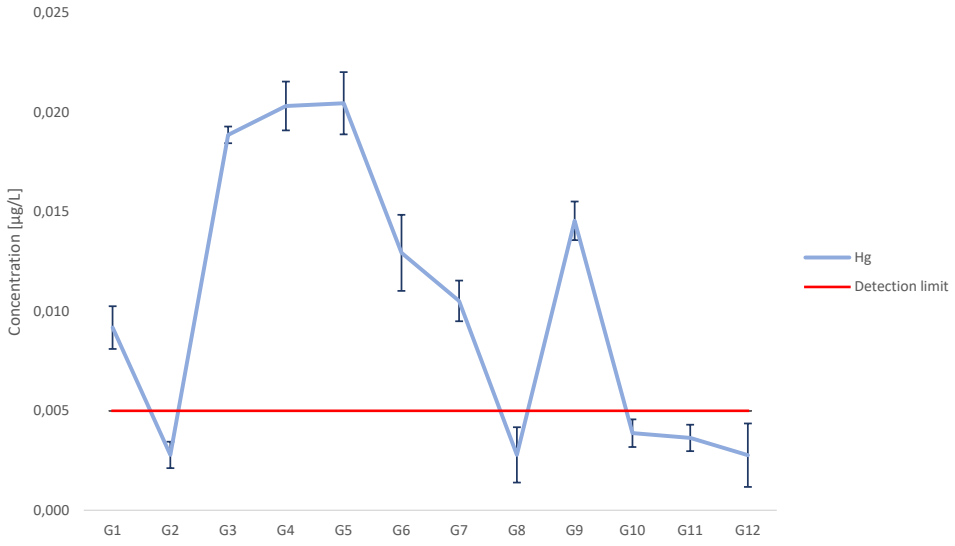

Figure 4.5: Concentration of mercury along the marine gradient in Ny-Ålesund.

closer to the marine environment, and lower mercury deposition far inland. Due to budget, practical, and safety reason, this extensive field trip was not performed.

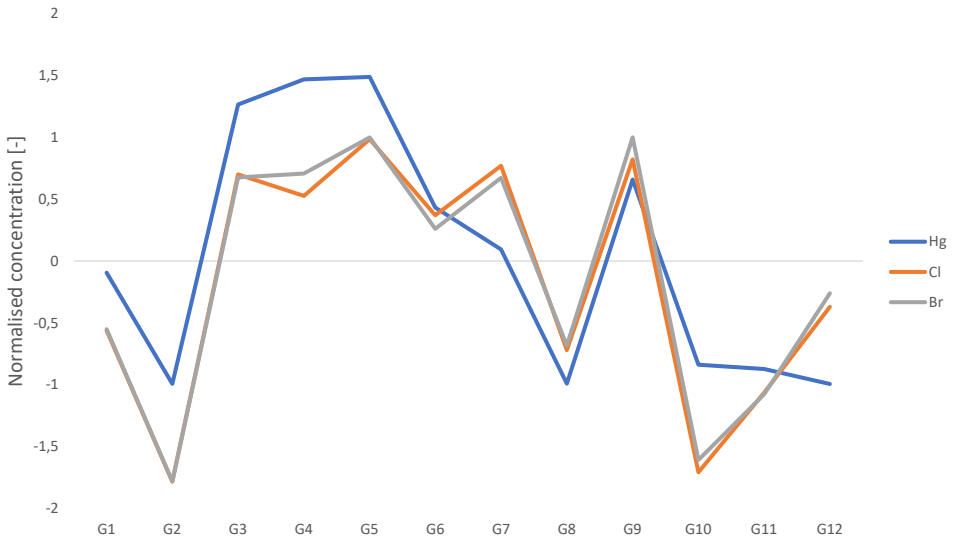

Figure 4.6: Normalised concentrations of mercury, chlorine and bromine in snow samples along marine gradient.

A correlation matrix of the selected elements was calculated to further examine marine effects. The correlation matrix is presented in Figure 4.7. There is a high degree of correlation in this data set, whereas many elements correlate with each other. As stated before, the marine originating elements chlorine and bromine are highly correlated with a correlation coefficient of 1, as expected. Mercury has a relatively high correlation coefficient with most elements, but are better correlated with the halogens. This supports the theory of halogen initiated photoreactions resulting in mercury deposition. An observation here is the nearly perfect correlation between cadmium and marine halogens, as well as the high correlation coefficient between cadmium and lead and nickel. The data set used to generate Figure 4.7 consists only of filtered samples. The strong correlation found between all the elements could indicate that there is some non-crustal origin of aluminium, lead, nickel, chromium, manganese, zinc, iron and copper.

4.2 Seasonal Variations

One of the research questions set out to investigate the seasonal variations of different elements in Svalbard snow. 4 sets of elemental data from ICP-MS analysis of Svalbard

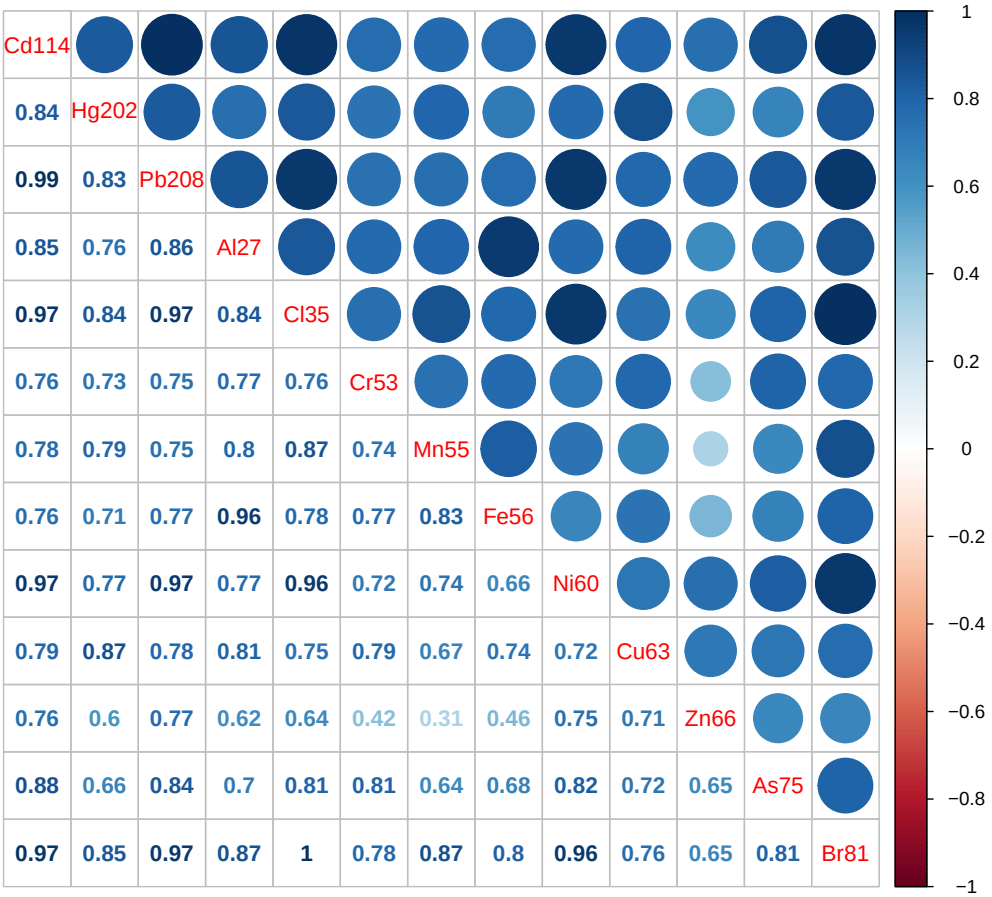

Figure 4.7: Correlation matrix of selected elements in samples along a marine gradient.

snow are presented in Table 4.1 - 4.4. Box plots were generated to inspect seasonal variations of mercury and halogen deposition. Figure 4.9 presents a box plot of mercury concentration in filtered snow from the different periods. Period 1 contains the highest mercury concentration observed in all of the data sets with $(0.030 \pm 0.002)\,\mu g\,L^{-1}$. The box plot of period 2 have almost the same median value as period 3, but is much narrower. Period 3 shows high spread in the box plot, including values of both high and low concentrations. Period 3 is set to the time when AMDEs are occurring, including both rapid deposition and reemission of mercury in Svalbard snow, which could explain the spread in the observed mercury concentrations. The box plot of period 4 is relatively narrow, with the most similar samples containing low concentrations of mercury.

Figure 4.8 presents the concentration of gaseous elemental mercury measured at Zeppelin Observatory in March 2019. The data have been supplied by NILU, and are not quality controlled as this happens after a whole year of measurements. However, these are valuable to discuss AMDEs occurring during the sampling days 16.03.19, 19.03.19, and 21.03.19. A slow decrease in GEM is observed the days before March 16th, indicating fluctuations of mercury levels, i.e. both deposition and reemission of mercury occurring at the same time. A rapid decrease of GEM is observed on March 19th and 21st, indicating atmospheric mercury depletion events happening both of these days. The sampling days March 19th and 21st were relatively sunny days after a couple of days with snow storms.

Moving on now to discuss the box plots of chlorine and bromine presented in Figure 4.10 and 4.11, respectively. There is an evident increase in both chlorine and bromine concentrations in Svalbard snow during the springtime sun return (period 3). Chlorine and bromine are strongly correlated in all data sets, explained by the common marine origin. There is a clear pattern followed by these marine halogens which is also observed in box plots of other elements. The increase of halogens during springtime sun return can be explained by the photochemical processes in sea salt which releases chlorine and bromine radicals, suggested by Simpson et al. (2007).

AMDEs need sunlight and a high content of halogens available. However, the content of chlorine and bromine in period 1 is relatively low. Thus, the high content of mercury in the snow in period 1 might be a result of dry or wet deposition. Figure 2.7 shows a high fluctuation in GEM concentrations during November which could be leading to this increased concentration of mercury in the snow. The mechanism of deposition is however unknown, but could be through dry or wet deposition.

PCA was performed on the data set to further investigate the seasonal variations. This yielded two principal component, PC1 and PC2, explaining respectively $34.17\,\%$ and $24.98\,\%$ of the variance, presented in Figure 4.12.

Figure 4.13 presents a plot of the loadings found from the PCA performed on the data set containing data from all periods. There is no immediate interpretation of the principal component axes. However, there are apparent clusters of loadings. The metals nickel, aluminium, iron, manganese, and copper are highly correlated in positive direction of both PC1 and PC2. Chromium, zinc, arsenic and cadmium are highly correlated with each other, and have low contribution to PC2. Mercury, lead, chlorine and bromine are highly correlated with each other, and is directed towards positive PC1 and negative PC2.

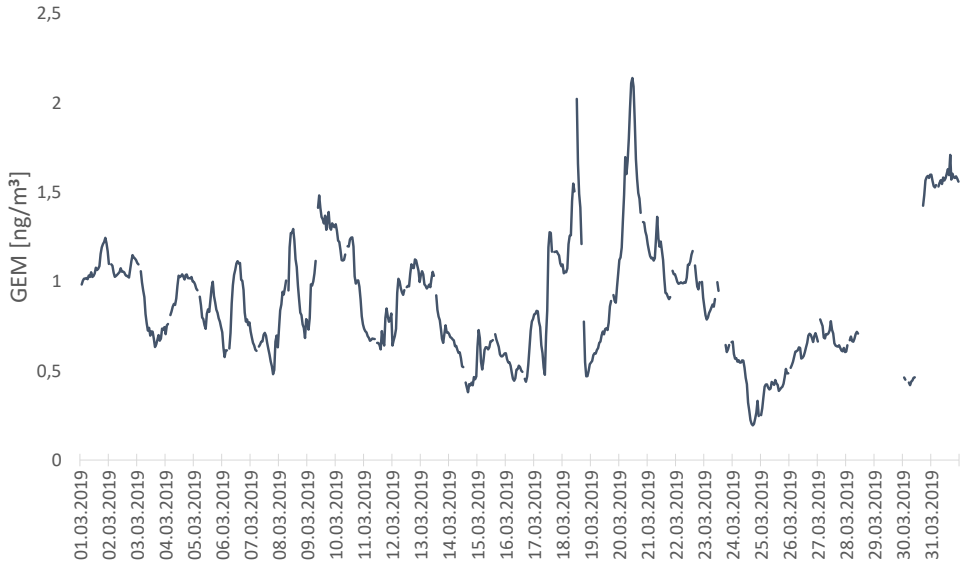

Figure 4.8: Hourly GEM concentrations in March 2019 measured at Zeppelin Observatory (Pfaffhuber, K. A., NILU, private communication, May 2019).

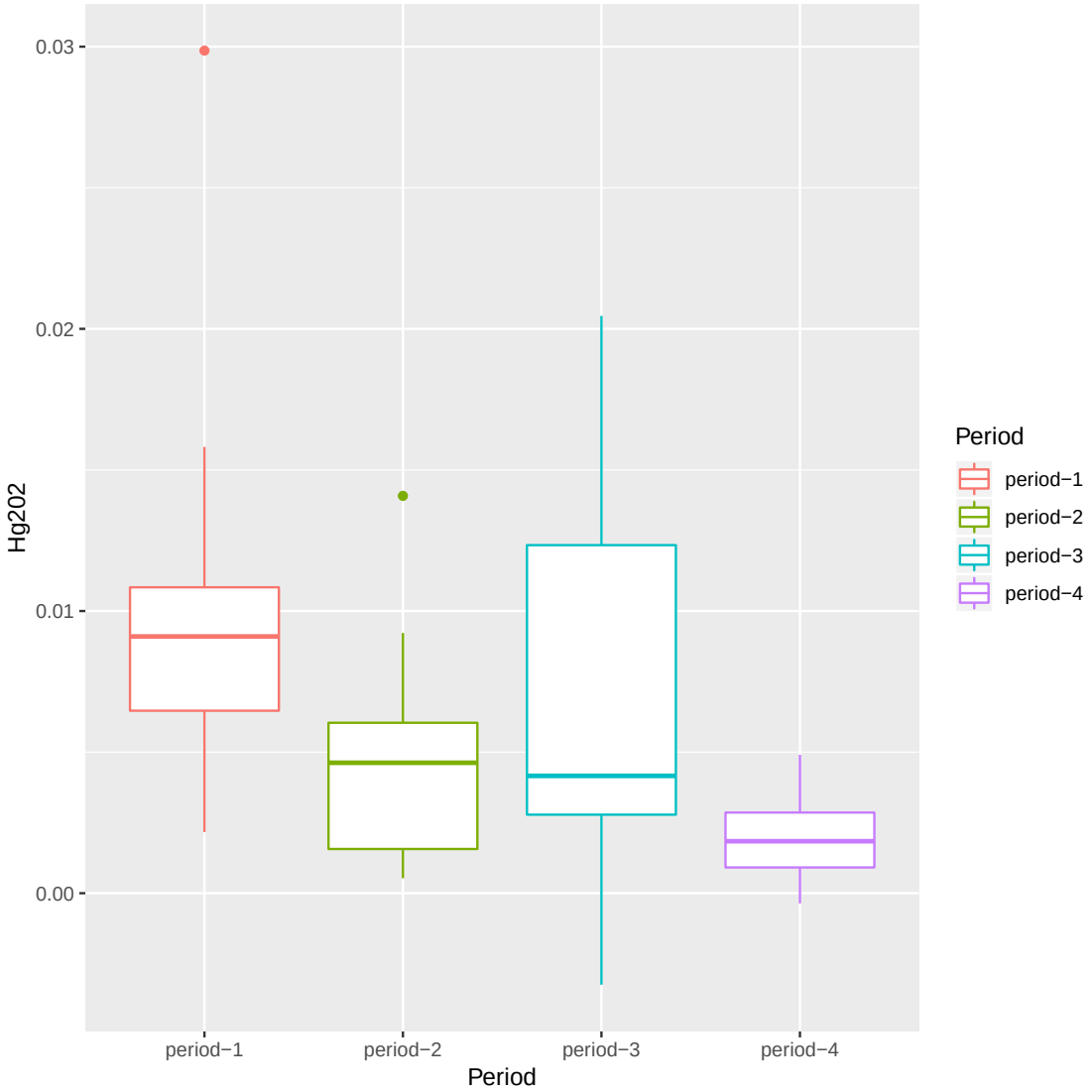

Figure 4.9: Box plot of mercury concentration in Svalbard snow from the 4 respective sampling periods: November 2018 (period 1), January and February 2019 (period 2), March 2019 (period 3), and April and May 2017 (period 4). Concentration is given in the unit [µg L^{-1}].

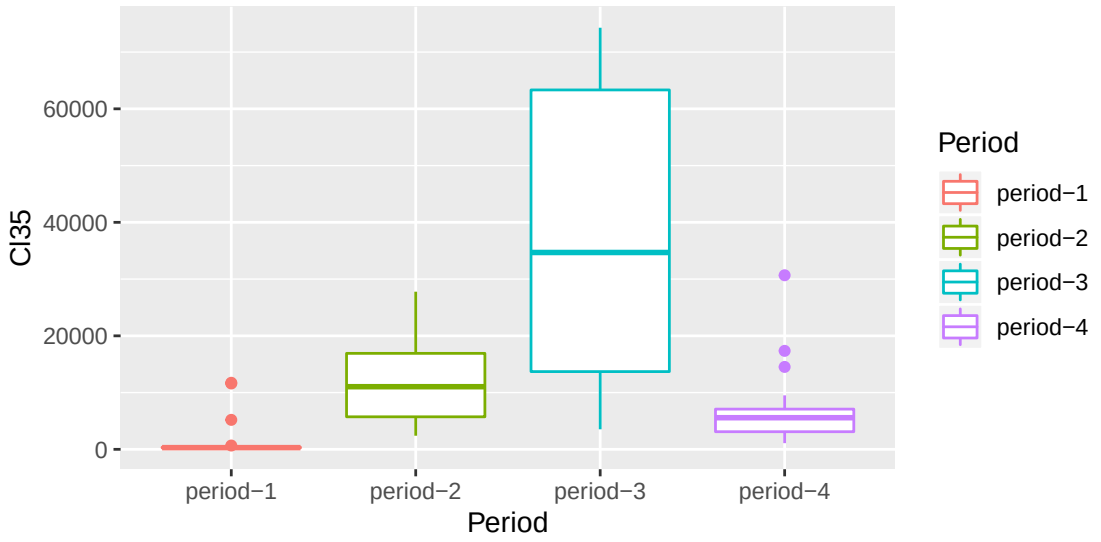

Figure 4.10: Box plot of chlorine concentration in Svalbard snow from the 4 respective sampling periods: November 2018 (period 1), January and February 2019 (period 2), March 2019 (period 3), and April and May 2017 (period 4). Concentration is given in the unit [µg L^{-1}].

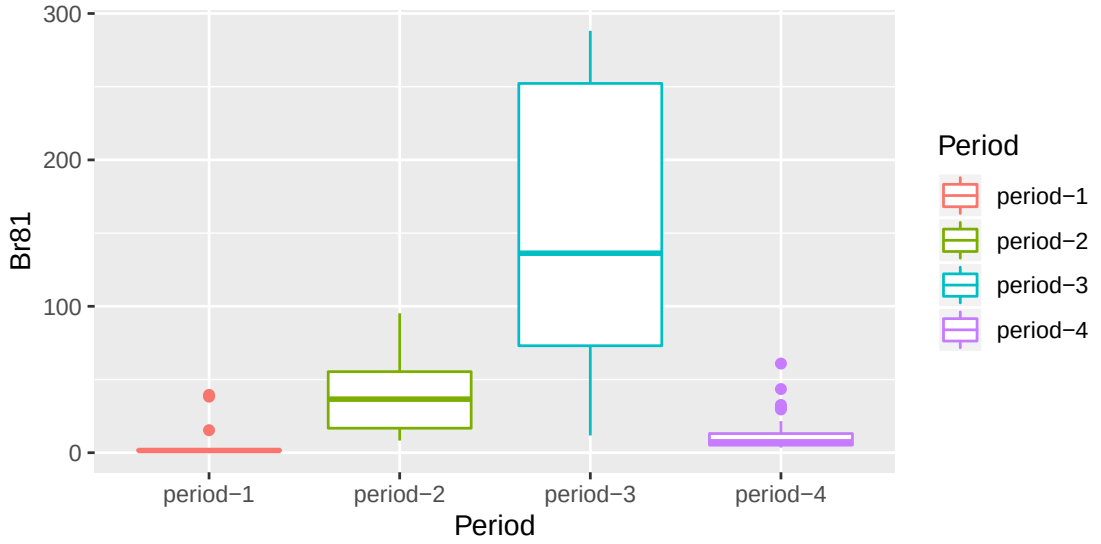

Figure 4.11: Box plot of bromine concentration in Svalbard snow from the 4 respective sampling periods: November 2018 (period 1), January and February 2019 (period 2), March 2019 (period 3), and April and May 2017 (period 4). Concentration is given in the unit [µg L^{-1}].

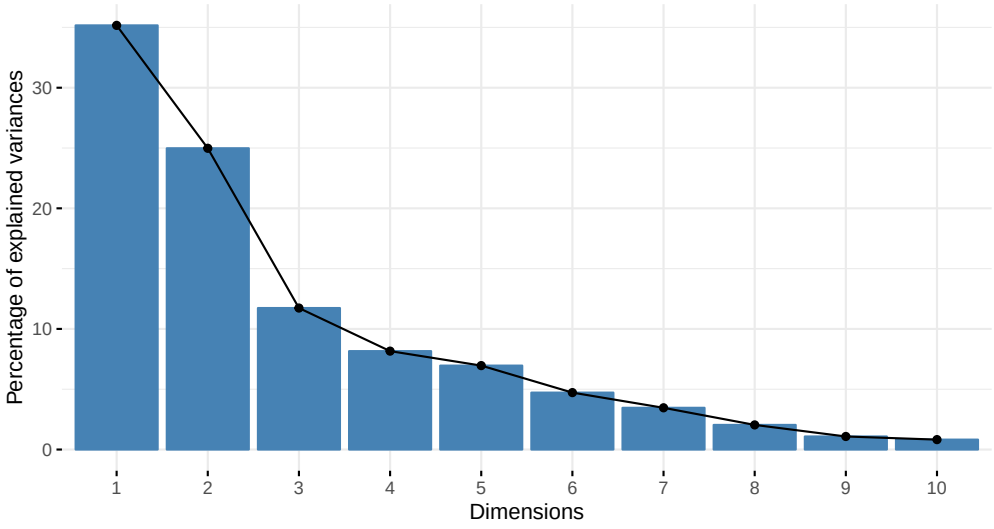

Figure 4.12: Scree plot of the percentage of explained variance of the different principal components created from the PCA.

There is a clear separation between the cluster of the Ni, Al, Fe, Mn, and Cu loadings and the cluster containing the Hg, Pb, Cl, and Br loadings. These clusters are separated by approximately $90°$, and may be considered independent of each other, i.e. no correlation. Thus, elements in these clusters might have different transportation routes in all periods.

A scores plot from the PCA performed on the data set containing data from all periods is presented in Figure 4.14. The different periods are marked with colour, and an ellipse is drawn around the majority of the samples to improve visualisation and simplify interpretation. What stands out in Figure 4.14 is the separation in the direction of period 2 and 3. Period 2 is directed in the same direction as the cluster of metal loadings (Al, Ni, Mn, Fe, Cu) in Figure 4.13, while period 3 appears to follow the cluster of loadings containing Br, Cl, Pb and Hg. Period 1 and 4 suggest low affection by either direction, but period 4 has a higher spread and is directed slightly towards the Al, Ni, Mn, Fe and Cu loadings.

The observed spread of the different periods in the scores plot suggests a large seasonal variation of the elemental composition in Svalbard snow. These results are likely to be related to the springtime return of the sun after the polar night. The theory suggests photochemically initiated halogen reactions as the basis of AMDEs, which agrees with the prominent deviation in which period 3 exhibits in Figure 4.14.

There is no immediate and clear interpretation of the principal components (PC1 and PC2) in Figure 4.14, but PC1 seems to be determined by increasing concentration of most elements, as observations along PC1 increases in elemental concentration. As period 2 and 3 is distinctly separated with mainly crustal affection of period 2 and mainly marine affection of period 3, could PC2 be interpreted as a differentiating axis of either crustal or marine origin.

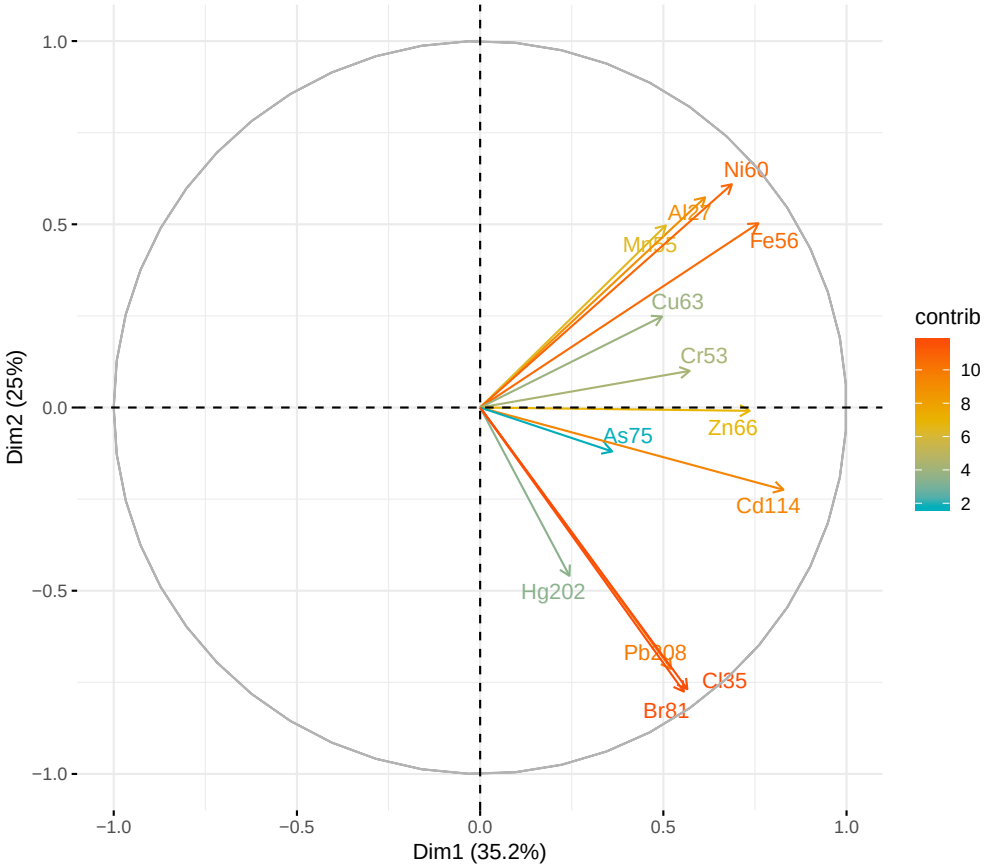

Figure 4.13: Plot of the loadings and their respective contributions to the principal components found from the PCA.

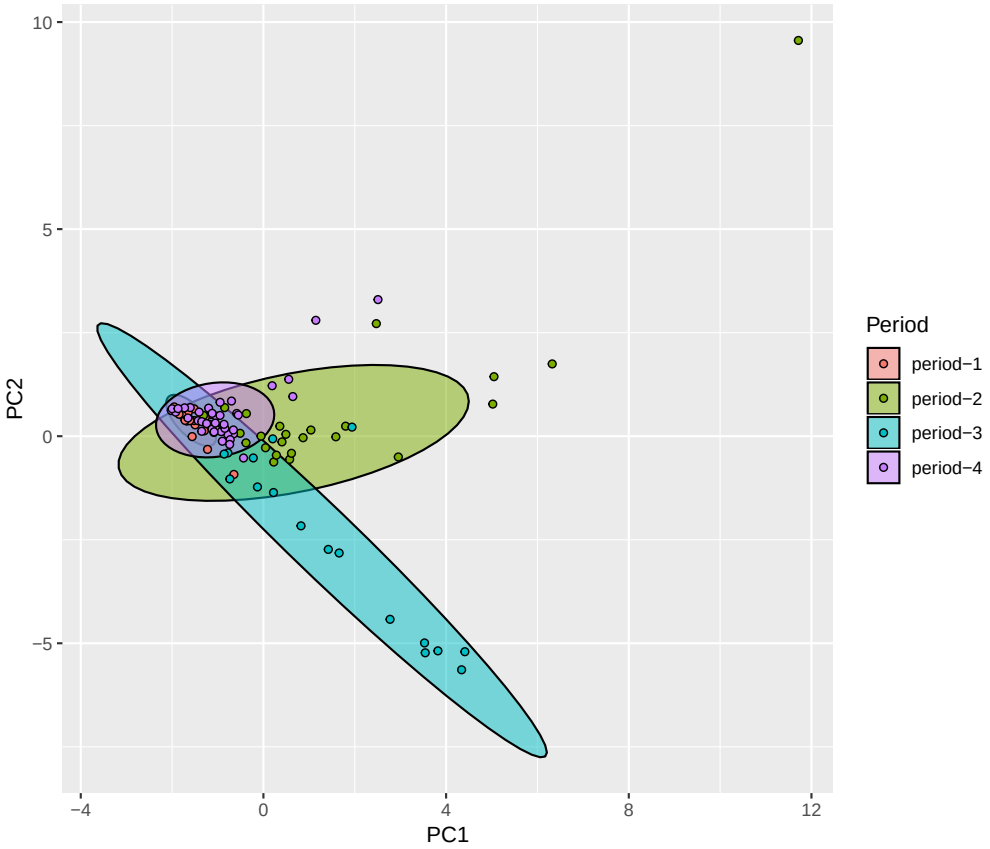

Figure 4.14: Scores plot from PCA performed on data from all sampling period. The respective sampling period is marked with a distinct coloured ellipse. Variance explained by the principal components is PC1 = 35.17 % and PC2 = 24.98 %.

4.3 Examining NOM by TOC/DOC and UV-Vis

Aromaticity in sample P1 - P10 was assessed by UV-Vis analysis. Milli-Q water was used as a reference to calibrate the UV-spectrophotometer. UV-Vis analysis at wavelength $\lambda = 254\,\mathrm{nm}$ suggests a low degree of aromatic compounds in the snow samples. The mean absorbance with UV radiation wavelength $254\,\mathrm{nm}$ is $\overline{\mathrm{Abs.}} = 0.0008$ for sample P1 - P4 (Longyearbyen) and $\overline{\mathrm{Abs.}} = 0.0012$ in sample P5 - P10 (Ny-Ålesund).

Freeze-drying the samples increased the UV absorbance, as a result of concentrating the amount of aromatic structures in the samples. The mean absorbance with UV radiation wavelength $254\,\mathrm{nm}$ is $\overline{\mathrm{Abs.}} = 0.0035$ for the concentrated sample P1 - P4 (Longyearbyen) and $\overline{\mathrm{Abs.}} = 0.0103$ in sample P5 - P10 (Ny-Ålesund). The UV-absorption results of both the pure samples and preconcentrated samples are presented in Table B.1 in Appendix A.

The samples were successfully preconcentrated by using freeze-drying, resulting in roughly tenfold concentration. This yielded a detectable signal of organic carbon in the TOC/TN Analyzer. TOC and DOC concentrations are presented in Table 4.6 and 4.7, as well as the POC concentration calculated by subtracting dissolved organic carbon concentration from the total organic carbon concentration. Tables 4.6 and 4.7 presents the actual concentration of TOC, DOC and POC in snow, calculated from the preconcentrated samples according to equation 4.2.

$$c\,(\text{before preconc.}) = \frac{V\,(\text{after preconc.})}{V\,(\text{before preconc.})} \cdot c\,(\text{after preconc.}) \tag{4.2}$$

Table 4.6: TOC, DOC, and POC values of the samples from Adventdalen, Longyearbyen (06.03.19).

Sample	TOC $[\mathrm{mg\,L^{-1}}]$	DOC $[\mathrm{mg\,L^{-1}}]$	POC $[\mathrm{mg\,L^{-1}}]$	SUVA
P1	0.470	0.193	0.282	0.2620
P2	0.483	0.219	0.265	0.0460
P3	0.497	0.174	0.323	0.2310
P4	0.474	0.178	0.296	0.2220

Table 4.8 presents the UV absorbance and SUVA values for the preconcentrated sample P1 to P10. SUVA values are used to assess the fraction of humic matter in the water. As a reminder, SUVA values greater than $4\,\mathrm{L\,mg^{-1}\,m}$ have a dominating fraction of humic matter, and SUVA values lower than $2\,\mathrm{L\,mg^{-1}\,m}$ are dominated by non-humic material. All samples have SUVA values lower than $2\,\mathrm{L\,mg^{-1}\,m}$, which indicate they are dominated by non-humic carbon. Humic matter are probably not distributed in the same way as other natural organic compounds, such as formate or acetate. Humic matter is usually linked to soil and decomposed remnants of organisms, which could explain the low fraction found in snow. The second research question involves distinguishing the different types of NOM in Arctic snow. With the current analytical procedure, only an overall characterisation of humic matter or non-humic matter is possible, and a further

Table 4.7: TOC, DOC, and POC results of the samples from Bayelva, Ny-Ålesund (16.03.19 and 19.03.19).

Sample	TOC [$\mathrm{mg\,L^{-1}}$]	DOC [$\mathrm{mg\,L^{-1}}$]	POC [$\mathrm{mg\,L^{-1}}$]	SUVA
P5	0.595	0.346	0.249	0.3800
P6	0.471	0.189	0.282	0.1050
P7	0.536	0.298	0.238	0.5170
P8	0.469	0.143	0.326	0.7750
P9	NDA	NDA	NDA	NDA
P10	0.429	0.166	0.263	0.2320

characterisation will be challenging with the current analysis technique and low amount of organic matter in the snow.

Table 4.8: UV absorbance and SUVA values of the preconcentrated samples P1 to P10.

Sample	UV [$\mathrm{cm^{-1}}$]	SUVA [$\mathrm{L\,mg^{-1}\,m}$]
P1	0.005	0.2620
P2	0.001	0.0460
P3	0.004	0.2310
P4	0.004	0.2220
P5	0.013	0.3800
P6	0.002	0.1050
P7	0.015	0.5170
P8	0.011	0.7750
P9	0.017	NDA
P10	0.004	0.2320

Figure 4.15 presents a plot of the TOC, DOC and POC concentrations in samples P1 to P10. The figure shows a negative correlation between DOC and POC, described by a correlation coefficient of $r_{\mathrm{POC/DOC}} = -0.76$. This could indicate an equilibrium between formation of DOC and POC. Interestingly, there were differences in the ratios of DOC-to-TOC between Longyearbyen and Ny-Ålesund samples. An average of $40\,\%$ of the organics is found as DOC in snow from Adventdalen, Longyearbyen, whereas an average of $45\,\%$ of the organic carbon is DOC in snow from Bayelva area, Ny-Ålesund. An explanation for the higher percentage of particulate organic carbon in Longyearbyen could be that the environment here have more particulate forming precursors, and organics are more inclined to exist as particulates.

Another interesting remark is the correlation between organic carbon with distance from the ocean. The sampling locations were sorted according to distance from the ocean, and their respective concentrations were plotted, which is presented in Figure 4.16. The level of dissolved organic carbon is found to be negatively correlated with distance from the ocean, and particulate organic carbon increases with distance from the ocean. This could be a result of DOC transport from the ocean to the land, before

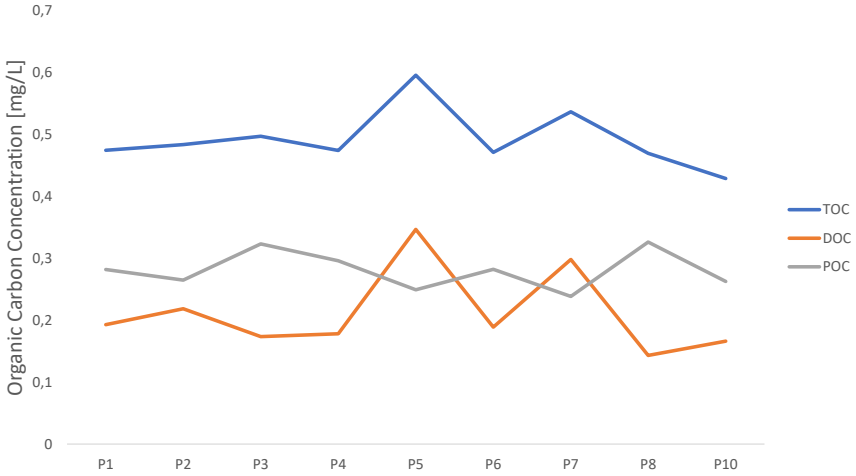

Figure 4.15: Organic carbon concentration of sample P1 to P10 from Longyearbyen and Ny-Ålesund.

transforming into particulates further away from the marine boundary.

4.4 Effects of Organic Matter on Mercury

One of the research questions set out to investigate the effects of organic matter on mercury concentration in snow. A correlation matrix of DOC, POC and mercury was created, and is presented in Figure 4.17. As previously discussed, there is a strong negative correlation between DOC and POC, which is prominent in the correlation matrix. A small positive correlation between POC and Hg is found at $r_{\text{POC/Hg}} = 0.29$. This could be a result of the particulates containing organics also contain mercury. This correlation is found based on only 9 samples, which is a great weakness for statistical analysis and investigating trends.

The theory of NOM and mercury interactions suggests complexation between DOC and mercury, however the slightly negative correlation coefficient between DOC and mercury ($r_{\text{DOC/Hg}} = -0.13$) does not support this. The low concentration of both DOC and mercury found in the 9 samples could be a factor for the poor correlation coefficient. In addition, the theory only describes NOM complexation in aquatic systems such as effluent and natural waters. As snow is solid water, this creates a different environment for chemical reactions to take place. The theory of NOM complexation in liquid water does not necessarily apply for this system of air-solid interactions.

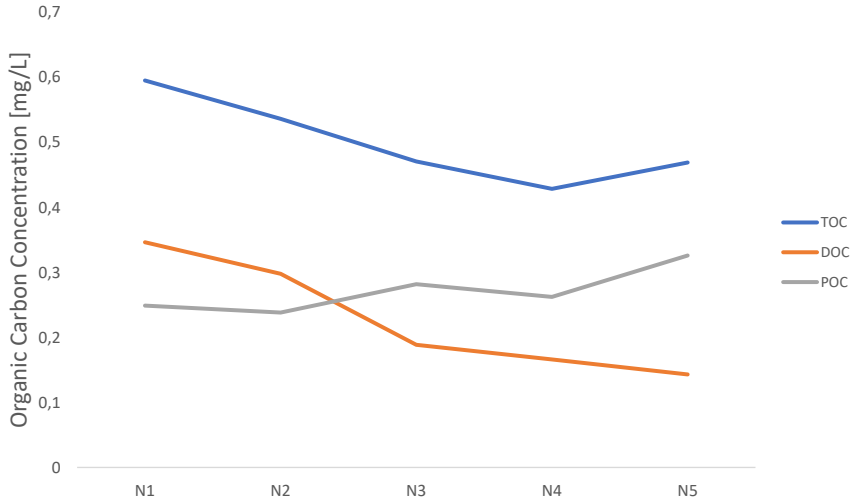

Figure 4.16: Organic carbon concentration of sample P5 to P10 in Ny-Ålesund sorted according to distance from the ocean.

4.5 Analysis of MAs by UPLC-MS

An UPLC-MS system was used in an experiment to attempt detection of molecular tracers from biomass burning. The MS system was set for detection of levoglucosan (m/z 161/71 and 161/101), galactosan (m/z 161/59 and 161/101), and mannosan (m/z 161/85 and 161/101). However, no standard solutions were used to find the optimal detection conditions of the MAs. A standard is necessary to develop optimal detection conditions for specific compounds, as well as replicating the experiment is difficult when not all of the variables were reported. For example, the article by You et al. (2016) did not report collision energy needed to ionise the MAs, forcing the UPLC-MS operator to assume several operating parameters for the experiment. The flow in this experiment was adjusted down to $0.15\,\mathrm{mL/\,min}$ due to pressure problems at $0.20\,\mathrm{mL/\,min}$. Lower flow will in addition to a longer column lead to a longer retention time than reported in the work of You et al. (2016).

The analysis gave no signal for the target compounds. This could be a result of a) the MS detection conditions were sufficient for detection, but there is no detectable amount of levoglucosan, galactosan, or mannosan in Svalbard snow, or b) the MS detection conditions were not optimal causing the system to not detect MAs at all, yielding only noise signals. The limit of detection (LOD) reported was $0.11\,\mathrm{ng\,mL^{-1}}$ (reported as three times the RSD: $0.037\,\mathrm{ng\,mL^{-1}}$). In the case of a), Svalbard snow is affected to a low degree of biomass burning. This means the other elemental pollutants, e.g. mercury, may originate in other sources than biomass burning, at least during this period in time.

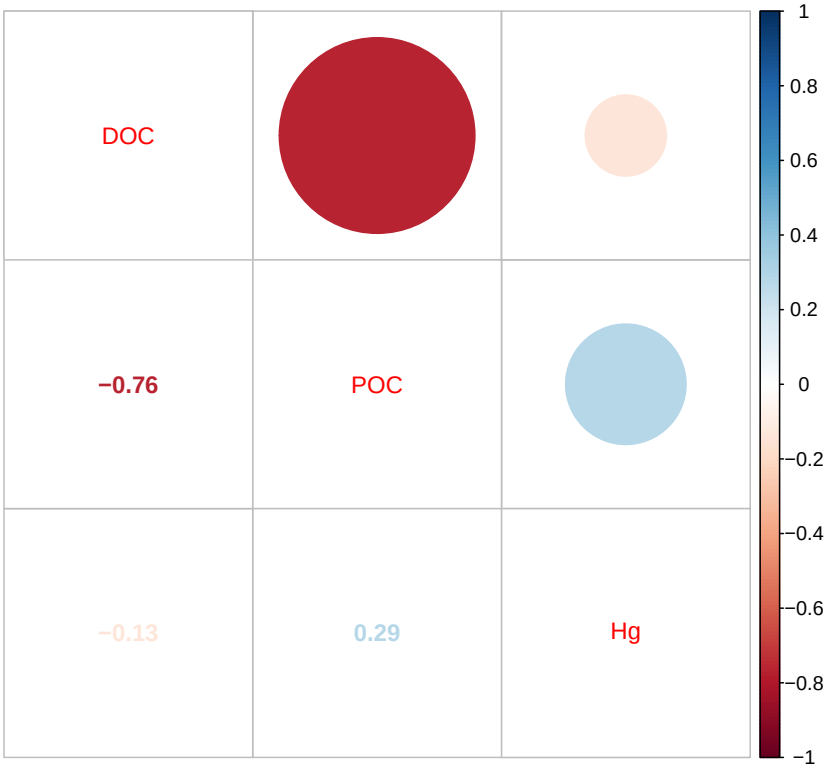

Figure 4.17: Correlation matrix of dissolved organic carbon, particulate organic carbon and mercury concentrations ($N = 9$).

The method used in this experiment was developed by You et al. (2016) using levoglucosan standards, and was applied on snow and ice core samples from Tibetan glaciers. They reported average levoglucosan levels from $0.28\,\mathrm{ng\,mL^{-1}}$ to $1.41\,\mathrm{ng\,mL^{-1}}$. Several levoglucosan concentration values was below LOD, and the highest single levoglucosan concentration found in Tibetan snow was $6.07\,\mathrm{ng\,mL^{-1}}$. These samples are collected in different locations on the Tibetan plateau - an area highly affected by pollution from the nearby countries China, India, and Pakistan. Considering the relative long distance between the Svalbard archipelago and important sources of biomass burning could explain the low or absent amount of levoglucosan and other MAs in Svalbard snow. In the case of b), levoglucosan is present in Svalbard snow, but the MS detection system is not optimised with respect to the target molecules.

4.6 Analysis of Anions using Ion Chromatography

Ion chromatography (IC) was used to assess the anions in the snow samples. The 10 larger samples from Adventdalen and Bayelva area was analysed using ion chromatography, and anion concentrations are presented in Table B.2 in Appendix B.

IC quantified the following naturally occurring elements in the environment: F^-, Cl^-, $NO_2{}^-$, Br^-, $NO_3{}^-$, $PO_4{}^{3-}$ and $SO_4{}^{2-}$. Chloride and bromide are compounds of interest, as they describe marine influence in the environment, and may according to theory be linked to the deposition of mercury during AMDEs. Cl and Br will also be assessed in the ICP-MS analyses, however, ICP-MS will also take into account molecular structures containing Cl and Br, whereas IC will only quantify ionic chlorine and bromine. $SO_4{}^{2-}$ is one of the main constituents in Arctic haze, which is a product of anthropogenic air pollution, and act as molecular tracer for anthropogenic combustion related emissions. A summary of concentrations of interesting compounds is presented in Table 4.9 (Adventdalen, Longyearbyen) and Table 4.10 (Brøggerdalen, Ny-Ålesund). The tables 4.9 and 4.10 contain many values at $0.00\,\mathrm{mg\,L^{-1}}$. However, investigating the

Table 4.9: Ion concentration of compounds of interest in polar snow.

Sample	Cl^- [mg L^{-1}]	Br^- [mg L^{-1}]	$NO_3{}^-$ [mg L^{-1}]	$SO_4{}^{2-}$ [mg L^{-1}]
P1	1.26	0.00	0.00	0.00
P2	1.54	0.00	0.00	0.00
P3	1.25	0.00	0.09	1.07
P4	0.95	0.00	0.00	0.00

IC chromatograms shows peaks at known retention times for several compounds. This means the compounds are present in most of the samples, but the concentration is lower than the limit of quantification (LOQ) of $0.02\,\mathrm{mg\,L^{-1}}$.

Sample P3 are the only sample from Longyearbyen with a detectable amount of $SO_4{}^{2-}$ in the snow. Investigation of $\delta S^{34/32}$-values from ICP-MS analysis may help differentiate between marine and anthropogenic sourced sulphur. $\delta S^{34/32}$-values from

Table 4.10: Ion concentration of compounds of interest in polar snow.

Sample	Cl^- [mg L^{-1}]	Br^- [mg L^{-1}]	$NO_3{}^-$ [mg L^{-1}]	$SO_4{}^{2-}$ [mg L^{-1}]
P5	3.48	0.00	0.07	0.67
P6	0.67	0.00	0.06	0.12
P7	1.74	0.00	0.07	0.45
P8	12.74	0.07	0.00	1.20
P9	8.46	0.07	0.08	1.04
P10	6.51	0.07	0.07	1.35

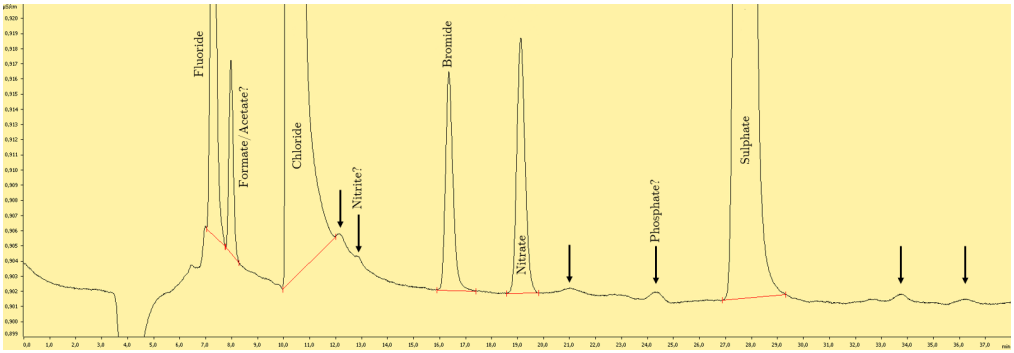

Figure 4.18: IC analysis of P10 from Bayelva area, Ny-Ålesund.

Longyearbyen were ranging between 16.9 and 20.6, which indicate marine sourced sulphur.

There is a observable difference in concentration range between samples P5-P7 and P8-P10 in both Cl^-, Br^-, and $SO_4{}^{2-}$. These two sample collections were sampled at different dates, 16.03.19 and 19.03.19, respectively. The time variation and weather in between could be a reason for the difference in values. $\delta S^{34/32}$-values of snow sampled in Ny-Ålesund November 2019 indicate marine sourced sulphur compounds, as the values are ranging between 16.2 and 28.9. The slight decrease in $SO_4{}^{2-}$ with distance from the ocean in sample P5-P7 also indicate that sulphur has marine origin during springtime.

Figure 4.18 presents the chromatogram from the IC analysis of sample P10. There are several peaks corresponding to values found in an overview of retention times for the specific column used in this experiment, including fluoride, formate, acetate, chloride, nitrite, bromide, nitrate, phosphate, and sulphate. There are remaining peaks not corresponding to a known compound in the chromatogram. These could be system peaks for the IC system, or could indicate organic ions such as amino acids, proteins, or humic acids. As previously mentioned, humic acids is not one, single compound, but a complex mixture of organic functional groups in a vast variety of arrangements. This makes it challenging to pinpoint humic acids as a group in a ion chromatogram, especially to one single peak. The peaks seen here are most likely natural organic compounds such as amino acids or other inorganic anions. However, a presence of formate or other simple organic anions indicate that Svalbard snow is susceptible to biomass burning emission, as organic anions are molecular tracers for biomass burning. The signal seen in Fig-

ure 4.18 might be overlapping with other analytes as well as being under the detection quantification limit. This gives further evidence to a low affection of biomass burning to Svalbard snow.

4.7 Sampling Remarks and Sources of Error

The environmental phase under study in this thesis is snow, as the goal is to investigate the capture mechanisms of mercury in snow during mercury depletion events. Svalbard was selected for study as a siting criterion to investigate the continental effects of long-range transported pollutants. It is an easily accessed area of the Arctic and is suited to investigate AMDEs during the springtime sun return. Sampling was performed near the city of Longyearbyen, with relatively few emission sites, and in the more remote location Ny-Ålesund. To investigate the marine effects on mercury depletion, the snow was sampled with increasing distance from the ocean. While sampling, avoiding breathing directly on the snow under study is important to avoid personnel contamination of the sample, as well as avoiding touching the snow with bare hands or outside gloves. A fingerprint is enough to cause interference in the ICP-MS analysis. Nitrile gloves were not used due to practical reasons.

Sample container was selected with respect to the properties under study. Metal-free polythene tubes do not interfere with elemental composition, which was used for snow samples for ICP-MS analysis. However, the polyethylene bags used for snow sampling may interfere for the analysis of organic components. Samples for elemental analysis by ICP-MS was preserved with a few drops of nitric acid (HNO_3) to prevent adhesion of the dissolved compounds to the sample container walls. The sample containers are airtight to ensure a closed system and prevent any interaction between the sample and the environment during transportation.

After melting the larger snow samples, the melted water was transferred to prewashed $500\,\mathrm{mL}$ aluminium bottles. The aluminium bottles were completely filled to negate oxidisation effects. An unexpected chemical process occurred in some of the aluminium bottles during travelling and storage prior to analysis. Some samples were carbonated and the water was cloudy and white after a few weeks of storage. The opaqueness could be explained by formation of $CaCO_3$, since many of the similar samples were high in calcium. The source of carbon dioxide is still unknown.

Initial TOC and DOC analysis of pure sample yielded concentrations right above the limit of quantification and below, respectively. Freeze-drying the samples from $250\,\mathrm{mL}$ to $25\,\mathrm{mL}$ was used to concentrate the analytes and more conveniently assess the level of organics in the snow. Freeze-drying should in theory not remove analytes of interest, but the transfer between several different sample containers could affect the final result. Another disadvantage of this concentration method is that inorganic constituents will concentrate as well. This might cause interference in the instrumentation and yield imprecise results.

ICP-MS analysis revealed a low concentration of most elements in the snow. This is advantageous, as there are fewer challenges during analysis compared to other sam-

ple compositions, and the simple matrix causes less interference with analytes of interest. However, matrix effects might still have an effect on the results. Several elements showed a relatively high $RSD\%$, including mercury, cadmium, and arsenic. Mercury is the main compound of interest and had a relative high average $RSD\%$ of $12\,\%$ in period 3. However, a correlation between mercury with marine halogens was observed in all sampling periods, indicating significant values for mercury even at values near the quantification detection limit (Mercury detection limit at $0.0050\,\mu\mathrm{g\,L^{-1}}$, found in Table B.7 in Appendix C).

4.8 Further work

The level of organic carbon was found to be relatively low, in the range of $0.429\,\mathrm{Cmg/L}$ - $0.595\,\mathrm{Cmg/L}$. Further work could be to do additional purification and concentration processes and look into the composition of organic matter, to differentiate between humic and fulvic acids in snow, if any. Also, quantification of methylmercury in snow could be of interest to investigate the methylation process of deposited mercury.

A high correlation was found between mercury and chlorine. It could be interesting to further investigate the complexation process of mercury and chloride, and look into differences in reemission rates of mercury in presence and absence of chloride. This could provide further knowledge in capture mechanisms of mercury in Arctic snow.

Chapter 5

Conclusion

Snow sampled during several different seasons in Longyearbyen and Ny-Ålesund have been investigated for elemental pollutants. The main focus has been on finding supporting evidence of atmospheric mercury depletion events occurring during the sampling in March 2019. In addition, organic matter in the snow has been assessed to look at possible capture mechanisms of mercury during AMDEs.

ICP-MS analysis of snow sampled in 4 periods, November 2018 (period 1), January and February 2019 (period 2), March 2019 (period 3), and May 2017 (period 4), revealed an increased fluctuation in mercury concentration during March 2019, which suggests AMDEs were occurring during the sampling period 3. Mercury concentrations in period 2 and 4 were considerably lower than for period 3, and period 1 had some higher observations of mercury. Data of GEM measured at Zeppelin Observatory (Ny-Ålesund) revealed a decrease in gaseous mercury during sampling days in March 2019, supporting the statement of AMDEs occurring these days.

Investigating particulates and calculating crustal enrichment factors of the elements in Svalbard snow revealed a mainly crustal source of Cr, Mn, Fe, Ni, Cu and Pb. The CEF values also indicate that Cd, Hg, Zn and As have a non-crustal source in snow sampled March 2019.

Organic matter was assessed by TOC/DOC and UV-Vis analyses, to measure the level of organics in the snow and for evaluating the fraction of humic matter. Organic carbon was observed in the range $0.429\,\mathrm{mg\,L^{-1}}$ - $0.595\,\mathrm{mg\,L^{-1}}$. SUVA values suggested the main fraction of the water samples was non-humic matter. No correlation was found between mercury and neither DOC or POC. This might indicate the level of either mercury and organics is too low for complexation to occur, or the theory of NOM-mercury complexation do not apply on snow, as the phases in the snow-air system might have different properties than a liquid water system. However, the high correlation found between mercury and halogens could indicate mercury is hindered to reemit and retained in the snow by chlorine, bromine, or a combination of both. The capturing of mercury in snow results in larger amounts of mercury being released to the marine biota during springtime snowmelt, resulting in future exposure of dietary mercury to the food chain.

Bibliography

Aiken, G. R., Hsu-Kim, H., Ryan, J., March 2011. Influence of dissolved organic matter on the environmental fate of metals, nanoparticles, and colloids. Environmental science & technology 45, 3196–201.

Aksnes, K., 2018. Mørketid / polar night. (last updated: 18.12.18, accessed: 10.06.2019).
URL https://snl.no/m%C3%B8rketid

Alsberg, B. K., 2018. Chemometrics (version 0.50). Course compendium TKJ4175, Norwegian University of Science and Technology, Trondheim.

Barr, S., 2019. Ny-Ålesund. (last updated: 03.04.19, accessed: 10.06.19).
URL https://snl.no/Ny-%C3%85lesund

Barrie, L. A., Delmas, R. J., Prinn, R. G., 1994. Polar Atmosphere and Snow Chemistry. Springer US, Boston, MA, Ch. 9, pp. 149–164.
URL https://doi.org/10.1007/978-1-4615-2524-0_9

Bartels-Rausch, T., Huthwelker, T., Jöri, M., Gaeggeler, H., Ammann, M., October 2008. Interaction of gaseous elemental mercury with snow surfaces: Laboratory investigation. Environmental Research Letters 3, 045009.

Bartels-Rausch, T., Krysztofiak, G., Bernhard, A., Schläppi, M., Schwikowski, M., Ammann, M., 2011. Photoinduced reduction of divalent mercury in ice by organic matter. Chemosphere 82 (2), 199 – 203.
URL http://www.sciencedirect.com/science/article/pii/S0045653510011525

Berg, T., Steinnes, E., 1997. Recent trends in atmospheric deposition of trace elements in norway as evident from the 1995 moss survey. Science of The Total Environment 208 (3), 197 – 206.
URL http://www.sciencedirect.com/science/article/pii/S0048969797002532

Budnik, L., Casteleyn, L., 2018. Mercury pollution in modern times and its socio-medical consequences. Science of the Total Environment 654, 720–734.
URL https://www.scopus.com/inward/record.uri?eid=2-s2.0-85056589642&doi=10.1016%2fj.scitotenv.2018.10.408&partnerID=40&md5=2ab784cbe0bfc9fe9e09660e09d516da

Budnik, L. T., Casteleyn, L., 2019. Mercury pollution in modern times and its socio-medical consequences. Science of The Total Environment 654, 720 – 734.
URL http://www.sciencedirect.com/science/article/pii/S0048969718343080

Chemistry Libratexts, 2019. Phase diagrams. (last updated: 27.04.19, accessed: 10.05.2019).
URL https://chem.libretexts.org/Bookshelves/General_Chemistry/Map%3A_General_Chemistry_(Petrucci_et_al.)/12%3A_Intermolecular_Forces%3A_Liquids_And_Solids/12.4%3A_Phase_Diagrams

Donohoue, D., Bauer, D., Cossairt, B., Hynes, A., June 2006. Temperature and pressure dependent rate coefficients for the reaction of hg with br and the reaction of br with br: A pulsed laser photolysis-pulsed laser induced fluorescence study. The journal of physical chemistry. A 110, 6623–32.

Douglas, T. A., Sturm, M., Simpson, W. R., Brooks, S., Lindberg, S. E., Perovich, D. K., 2005. Elevated mercury measured in snow and frost flowers near arctic sea ice leads. Geophysical Research Letters 32 (4).

Fraser, A., Dastoor, A., Ryzhkov, A., September 2017. How important is biomass burning in canada to mercury contamination? Atmospheric Chemistry and Physics Discussions, 1–39.

Gu, B., Bian, Y., L Miller, C., Dong, W., Jiang, X., Liang, L., January 2011. Mercury reduction and complexation by natural organic matter in anoxic environments. Proceedings of the National Academy of Sciences of the United States of America 108, 1479–83.

Haitzer, M., Aiken, G., Ryan, J., 2002. Binding of mercury(ii) to dissolved organic matter: The role of the mercury-to-dom concentration ratio. Environmental Science & Technology 36 (16), 3564–3570.
URL http://search.proquest.com/docview/230144305/

Halbach, K., Øyvind Mikkelsen, Berg, T., Steinnes, E., 2017. The presence of mercury and other trace metals in surface soils in the norwegian arctic. Chemosphere 188, 567 – 574.
URL http://www.sciencedirect.com/science/article/pii/S0045653517314285

Hald, S. J. K., 2014. Kartlegging og studie av metaller og naturlig organisk materiale i elver på svalbard. Master's Thesis, Norwegian University of Science and Technology.
URL http://hdl.handle.net/11250/2351949

Han, S., Gill, G., 2005. Determination of mercury complexation in coastal and estuarine waters using competitive ligand exchange method. Environmental Science & Technology 39 (17), 6607–6615.
URL http://search.proquest.com/docview/17403613/

International Organization for Standardization, November 1997. Water analysis - Guidelines for the determination of total organic carbon (TOC) and dissolved organic carbon (DOC). Standard, International Organization for Standardization.

International Organization for Standardization, November 2016. Water quality - Sampling - Part 14: Guidance on quality assurance and quality control of environmental water sampling and handling. Standard, International Organization for Standardization.

Kaleschke, L., Richter, A., Burrows, J., Afe, O., Heygster, G., Notholt, J., Rankin, A. M., Roscoe, H. K., Hollwedel, J., Wagner, T., Jacobi, H. W., 2004. Frost flowers on sea ice as a source of sea salt and their influence on tropospheric halogen chemistry. Geophysical Research Letters 31 (16).

Lai, A., M. Shafer, M., E. Dibb, J., Polashenski, C., J. Schauer, J., May 2017. Elements and inorganic ions as source tracers in recent greenland snow. Atmospheric Environment 164.

Lalonde, J. D., Amyot, M., Doyon, M.-R., Auclair, J.-C., 2002. Photo-induced hg(ii) reduction in snow from the remote and temperate experimental lakes area (ontario, canada). Journal of Geophysical Research: Atmospheres 108 (D6).
URL https://agupubs.onlinelibrary.wiley.com/doi/abs/10.1029/2001JD001534

National Center for Biotechnology Information, 2019. Mercury. (accessed: 28.01.2019).
URL https://pubchem.ncbi.nlm.nih.gov/compound/23931

Nilsson, A., 1997. Arctic Pollution Issues. AMAP.
URL http://urn.nb.no/URN:NBN:no-nb_digibok_2009111004037

NILU, 2018. Ebas database of environmental observations. (accessed: 28.05.2019).
URL http://ebas.nilu.no/Pages/DataSetList.aspx?key=088CDD034E6840C2914431EF3D535A47

NILU, 2019. Ebas database of environmental observations. (accessed: 28.05.2019).
URL http://ebas.nilu.no/Pages/DataSetList.aspx?key=088CDD034E6840C2914431EF3D535A47

Norwegian Enironment Agency - Norwegian PRTR, 2019. Facilities with permit. (accessed: 06.02.2019).
URL https://www.norskeutslipp.no/en/Lists/Virksomheter-med-utslippstillatelser/?SectorID=90&f=21

Norwegian Meteorological Institute, 2019. Accessed: 28.05.19.
URL https://www.yr.no/place/Norway/Svalbard/Ny-%C3%85lesund_observation_site/almanakk.html?dato=2019-03-15

Norwegian Polar Institute, 2019a. Svalbardskartet / thematic map of svalbard. (accessed: 04.02.2019).
URL http://www.npolar.no/en/services/maps/interactive/

Norwegian Polar Institute, 2019b. Svalbardskartet / thematic map of svalbard. (accessed: 04.02.2019).
URL http://www.npolar.no/en/services/maps/interactive/

Norwegian Polar Institute, 2019c. Svalbardskartet / thematic map of svalbard. (accessed: 04.02.2019).
URL http://www.npolar.no/en/services/maps/interactive/

Norwegian Polar Institute, 2019d. Topographic map of Svalbard. (accessed: 09.03.2019).
URL https://toposvalbard.npolar.no/

Outridge, P., Stow, J., Munthe, J., Goodsite, M., Douglas, T., Stern, G., Braune, B., Dietz, R., Pacyna, J., Donaldson, S., Krümmel, E., Leech, T., 2011. AMAP Assessment 2011: Mercury in the Arctic. Arctic Monitoring and Assessment Programme (AMAP). Arctic Monitoring and Assessment Programme (AMAP), Oslo, Norway.

R. Stephens, C., Shepson, P., Steffen, A., W. Bottenheim, J., Liao, J., Greg Huey, L., Apel, E., Weinheimer, A., Hall, S., Cantrell, C., Sive, B., Knapp, D., Montzka, D., S. Hornbrook, R., July 2012. The relative importance of chlorine and bromine radicals in the oxidation of atmospheric mercury at barrow, alaska. Journal of Geophysical Research (Atmospheres) 117.

Schroeder, W. H., Munthe, J., 1998. Atmospheric mercury—an overview. Atmospheric Environment 32 (5), 809 – 822, atmospheric Transport, Chemistry and Deposition of Mercury.
URL http://www.sciencedirect.com/science/article/pii/S1352231097002938

Sharma, S., Maeng, S., Nam, S.-N., Amy, G., 2011. 3.15 - characterization tools for differentiating natural organic matter from effluent organic matter. In: Treatise on Water Science, Four-Volume Set. Elsevier, Oxford, pp. 417–427.
URL http://www.sciencedirect.com/science/article/pii/B9780444531995000683

Sillanpää, M., Matilainen, A., Lahtinen, T., 2015. Chapter 2 - characterization of nom. In: Sillanpää, M. (Ed.), Natural Organic Matter in Water. Butterworth-Heinemann, pp. 17 – 53.
URL http://www.sciencedirect.com/science/article/pii/B9780128015032000021

Simpson, W., Carlson, D., Honninger, G., Douglas, T., Sturm, M., Perovich, D., Platt, U., 2007a. First-year sea-ice contact predicts bromine monoxide (bro) levels at barrow, alaska better than potential frost flower contact. Atmospheric Chemistry And Physics 7, 621–627.

Simpson, W. R., von Glasow, R., Riedel, K., Anderson, P., Ariya, P., Bottenheim, J., Burrows, J., Carpenter, L. J., Frieß, U., Goodsite, M. E., Heard, D., Hutterli, M., Jacobi, H.-W., Kaleschke, L., Neff, B., Plane, J., Platt, U., Richter, A., Roscoe, H., Sander, R., Shepson, P., Sodeau, J., Steffen, A., Wagner, T., Wolff, E., 2007b. Halogens and their role in polar boundary-layer ozone depletion. Atmospheric Chemistry and Physics 7 (16), 4375–4418.
URL https://www.atmos-chem-phys.net/7/4375/2007/

Skoog, D. A., West, D. M., Holler, F. J., Crouch, S. R., 2014. Fundamentals of analytical chemistry.

Skov, H., Brooks, S. B., Goodsite, M. E., Lindberg, S. E., Meyers, T. P., Landis, M. S., Larsen, M. R., Jensen, B., McConville, G., Christensen, J., 2006. Fluxes of reactive gaseous mercury measured with a newly developed method using relaxed eddy accumulation. Atmospheric Environment 40 (28), 5452 – 5463.
URL http://www.sciencedirect.com/science/article/pii/S1352231006004262

Statistics Norway, 2018. Population of svalbard. (accessed: 04.02.2019).
URL https://www.ssb.no/en/befolkning/statistikker/befsvalbard/halvaar

Steffen, A., Douglas, T., Amyot, M., Ariya, P., Aspmo, K., Berg, T., Bottenheim, J., Brooks, S., Cobbett, F., Dastoor, A., Dommergue, A., Ebinghaus, R., Ferrari, C., Gardfeldt, K., Goodsite, M., Lean, D., Poulain, A., Scherz, C., Skov, H., Sommar, J., Temme, C., 2008. A synthesis of atmospheric mercury depletion event chemistry in the atmosphere and snow. Atmospheric Chemistry And Physics 8 (6), 1445–1482.

Steinnes, E., Berg, T., Uggerud, H. T., 2011. Three decades of atmospheric metal deposition in norway as evident from analysis of moss samples. Science of The Total Environment 412-413, 351 – 358.
URL http://www.sciencedirect.com/science/article/pii/S0048969711011570

Thuesen, N. P., Barr, S., 2009. Svalbard. (accessed: 04.02.2019).
URL https://snl.no/Svalbard

UN environment, September 2017a. Minamata convention on mercury. Annex C & D.

UN environment, September 2017b. Minamata convention on mercury.

Uyguner Demirel, C., Bekbolet, M., Swietlik, J., January 2007. Natural organic matter: Definitions and characterization. Control of Disinfection By-Products in Drinking Water Systems, 253–277.

Walpole, R. R., Myers, R. H., Myers, S. L., Ye, K., 2012. Probability & Statistics for Engineers & Scientists, 9th Edition. Pearson Education.

Wang, P., 2015. Atmospheric mercury speciation and aerosol properties at ny-Ålesund, svalbard. Master's Thesis, Norwegian University of Science and Technology.
URL https://ntnuopen.ntnu.no/ntnu-xmlui/handle/11250/2351958

Wedepohl, K. H., 1995. The composition of the continental crust. Geochimica et Cosmochimica Acta 59 (7), 1217 – 1232.
URL http://www.sciencedirect.com/science/article/pii/0016703795000382

You, C., Song, L., Xu, B., Gao, S., 2016. Method for determination of levoglucosan in snow and ice at trace concentration levels using ultra-performance liquid chromatography coupled with triple quadrupole mass spectrometry. Talanta 148, 534 – 538.
URL http://www.sciencedirect.com/science/article/pii/S0039914015304847

Appendix A

Sampling locations

A Sampling in Adventdalen, Longyearbyen

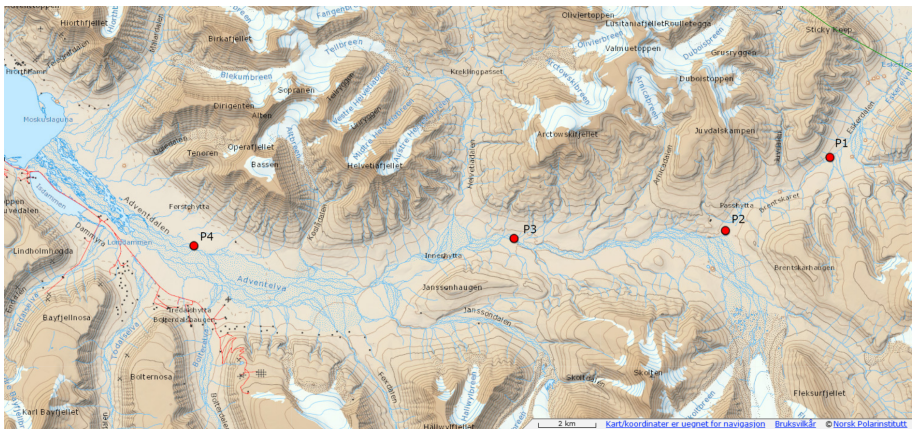

Figure A.1: Snow sample locations in Adventdalen, Longyearbyen (Norwegian Polar Institute, 2019d). Date: 06.03.19. Time: 10-13.

Table A.1: Snow sampling coordinates in Adventdalen, Longyearbyen. Date: 06.03.19. Time: 10-13.

Sample	Coordinates
P1	N 78° 12.9919′ E 16° 56.4646′
P2	N 78° 11.6979′ E 16° 46.6119′
P3	N 78° 11.6403′ E 16° 27.1082′
P4	N 78° 11.6461′ E 15° 57.7263′

B Sampling in Brøggerdalen, Ny-Ålesund

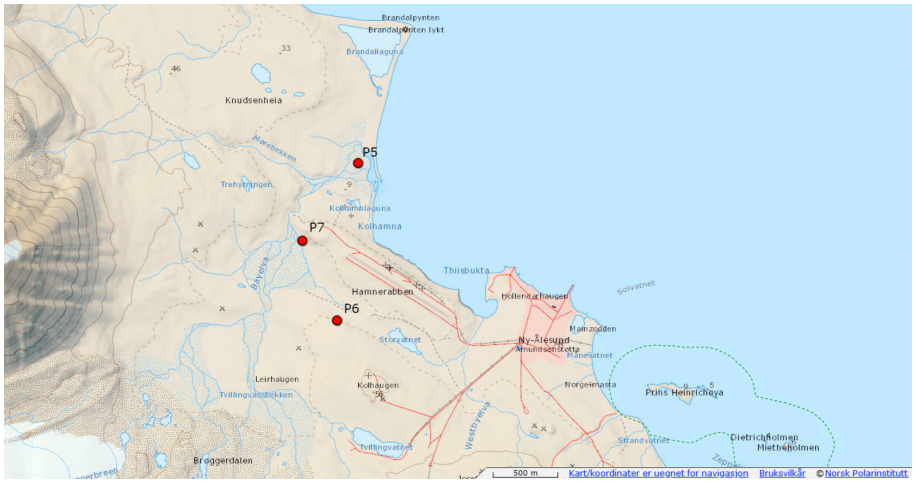

Figure A.2: Snow sample locations in Bayelva area, Ny-Ålesund (Norwegian Polar Institute, 2019d). Date: 16.03.19. Time: 12-16.

Table A.2: Snow sampling coordinates in Bayelva area, Ny-Ålesund. Date: 16.03.19. Time: 12-16.

Sample	Coordinates
P5	N 78° 56.1639′ E 11° 51.4651′
P6	N 78° 55.5021′ E 11° 51.1895′
P7	N 78° 55.8265′ E 11° 50.3501′

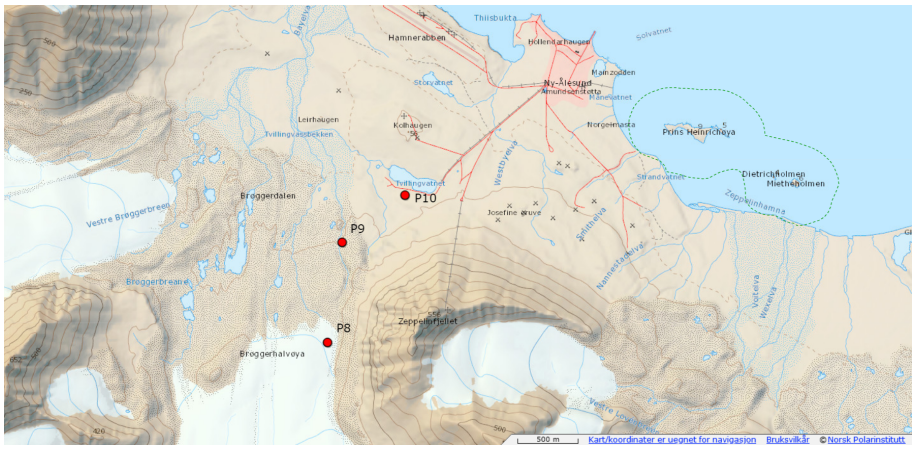

Figure A.3: Snow sample locations in Brøggerdalen, Ny-Ålesund (Norwegian Polar Institute, 2019d). Date: 19.03.19. Time: 9-12.

Table A.3: Snow sampling coordinates in Brøggerdalen, Ny-Ålesund. Date: 19.03.19. Time: 9-12.

Sample	Coordinates
P8	N 78° 54.2612′ E 11° 50.4732′
P9	N 78° 54.7017′ E 11° 50.6770′
P10	N 78° 54.9277′ E 11° 52.0756′

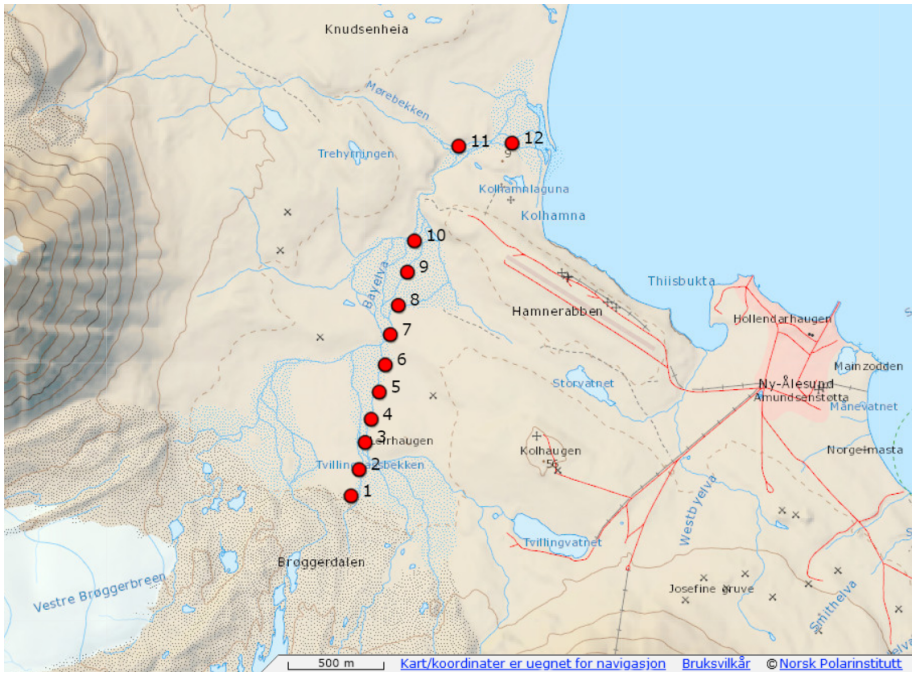

Figure A.4: Snow sample following a marine gradient in the Bayelva area, Ny-Ålesund (Norwegian Polar Institute, 2019d). Date: 21.03.19. Time: 9-11.

Table A.4: Snow sampling coordinates following the marine gradient in the Bayelva area, Ny-Ålesund. Date: 21.03.19. Time: 9-11.

Sample	Coordinates	Sample	Coordinates
1	N 78° 55.0855′ E 11° 49.2665′	7	N 78° 55.5440′ E 11° 49.7179′
2	N 78° 55.1587′ E 11° 49.3705′	8	N 78° 55.6285′ E 11° 49.8189′
3	N 78° 55.2364′ E 11° 49.4406′	9	N 78° 55.7247′ E 11° 49.9243′
4	N 78° 55.3028′ E 11° 49.5084′	10	N 78° 55.8142′ E 11° 50.0001′
5	N 78° 55.3806′ E 11° 49.5987′	11	N 78° 56.0864′ E 11° 50.5715′
6	N 78° 55.4581′ E 11° 49.6772′	12	N 78° 56.1043′ E 11° 51.3601′

Appendix B

Analytical results

A UV-Vis

Table B.1: UV-Vis measurements at $\lambda = 254\,\mathrm{nm}$ for both pure filtered samples and concentrated filtered samples.

Sample (Pure sample)	Absorbance	Sample (Conc. $\times \sim 10$)	Absorbance
P1	0.000	P1*	0.005
P2	0.000	P2*	0.001
P3	0.002	P3*	0.004
P4	0.001	P4*	0.004
P5	0.001	P5*	0.013
P6	0.001	P6*	0.002
P7	0.001	P7*	0.015
P8	0.002	P8*	0.011
P9	0.001	P9*	0.017
P10	0.001	P10*	0.004

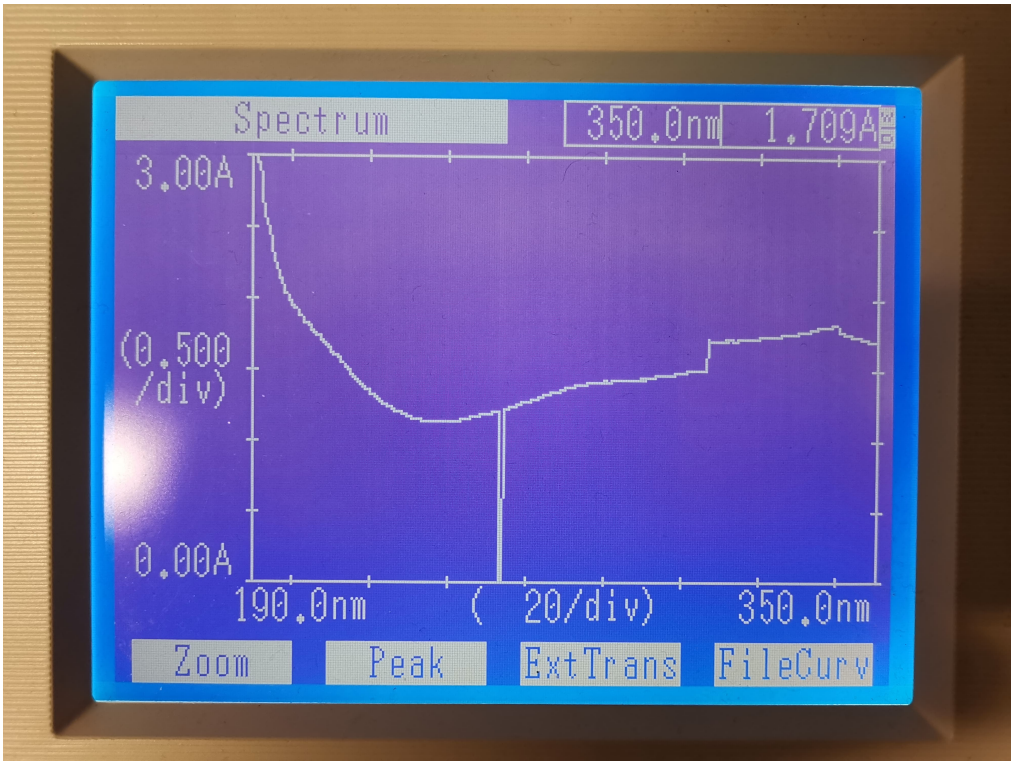

Figure B.1: UV scan of sample P1 from 190 nm to 350 nm.

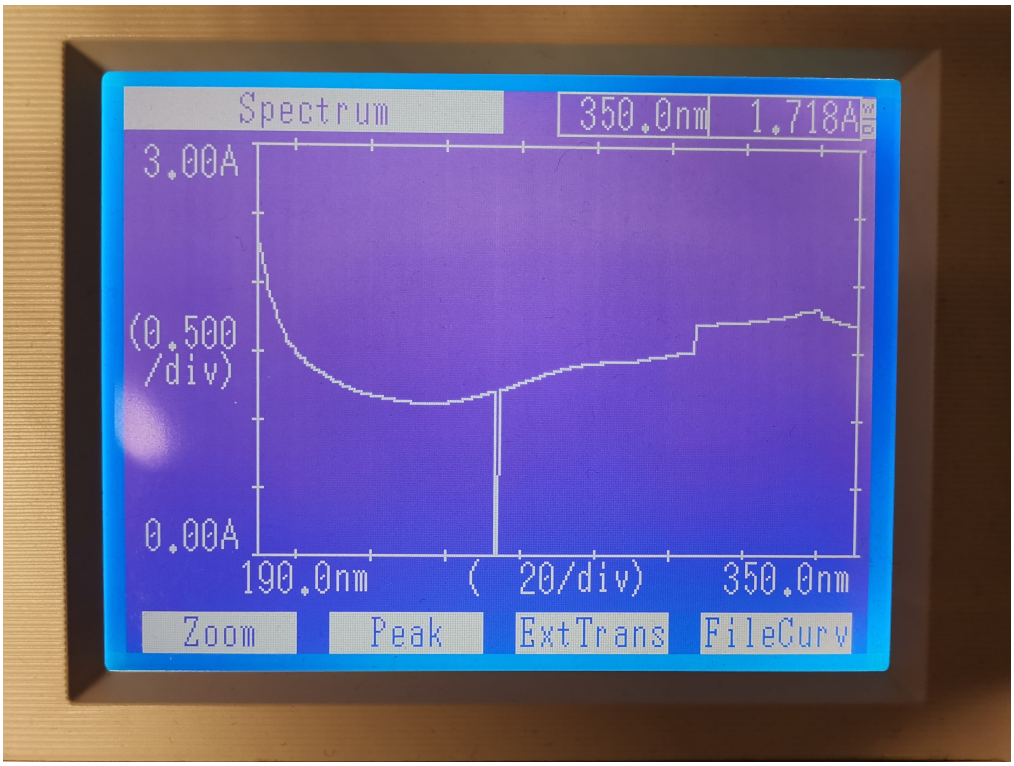

Figure B.2: UV scan of sample P2 from 190 nm to 350 nm.

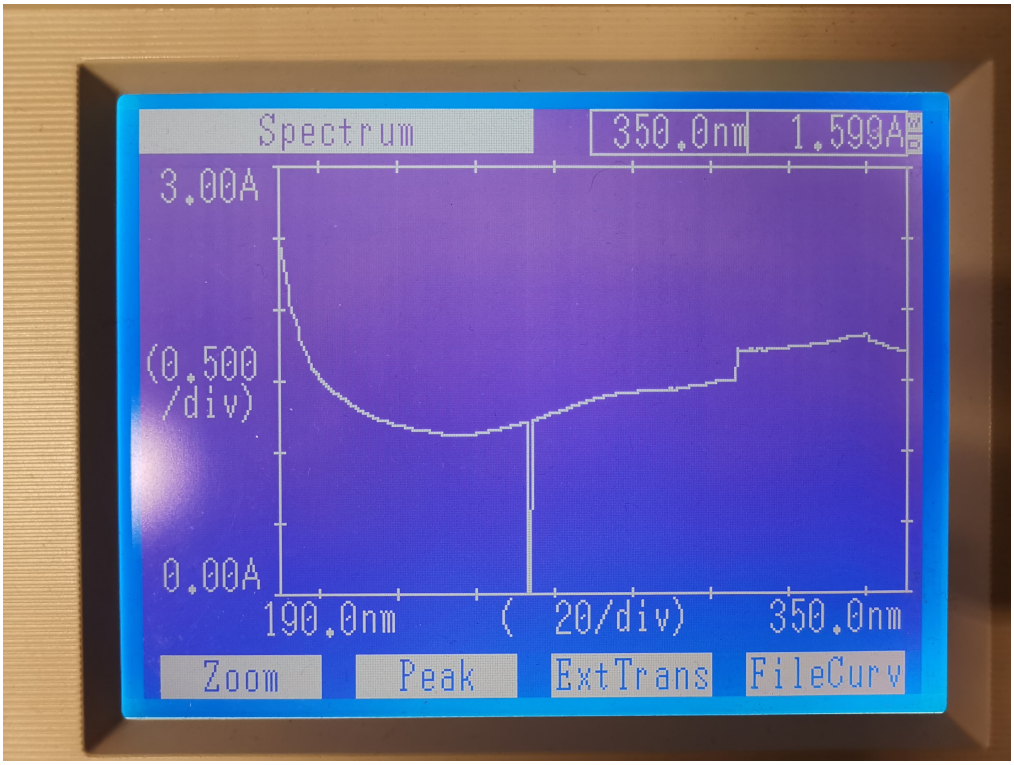

Figure B.3: UV scan of sample P3 from 190 nm to 350 nm.

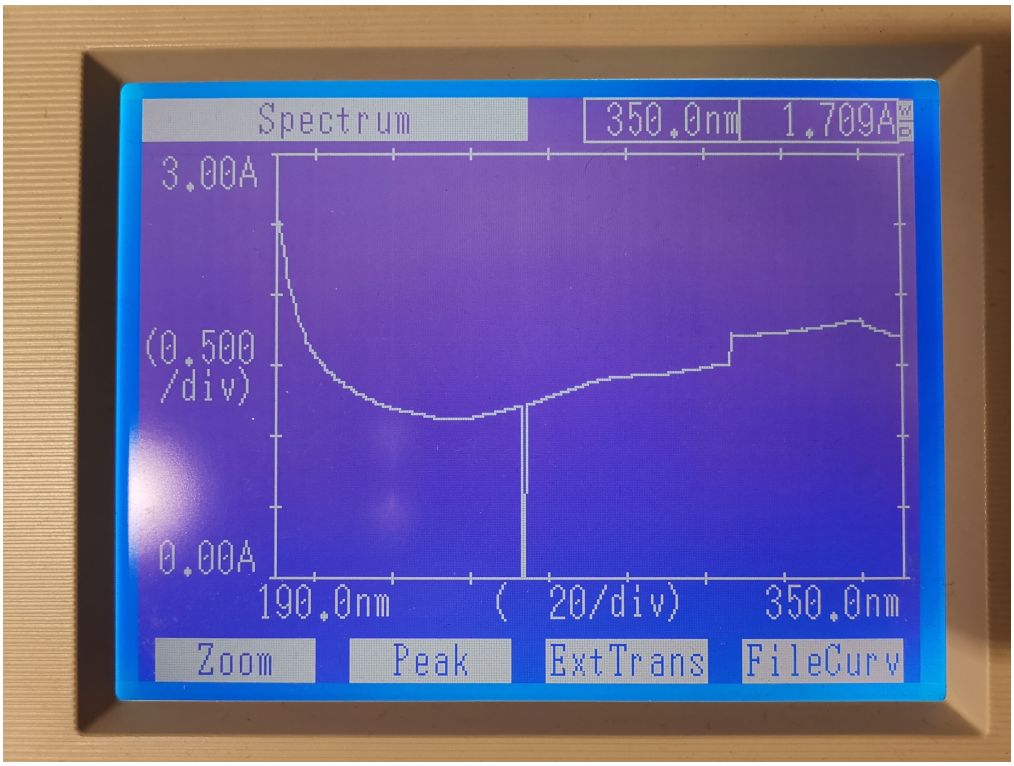

Figure B.4: UV scan of sample P4 from 190 nm to 350 nm.

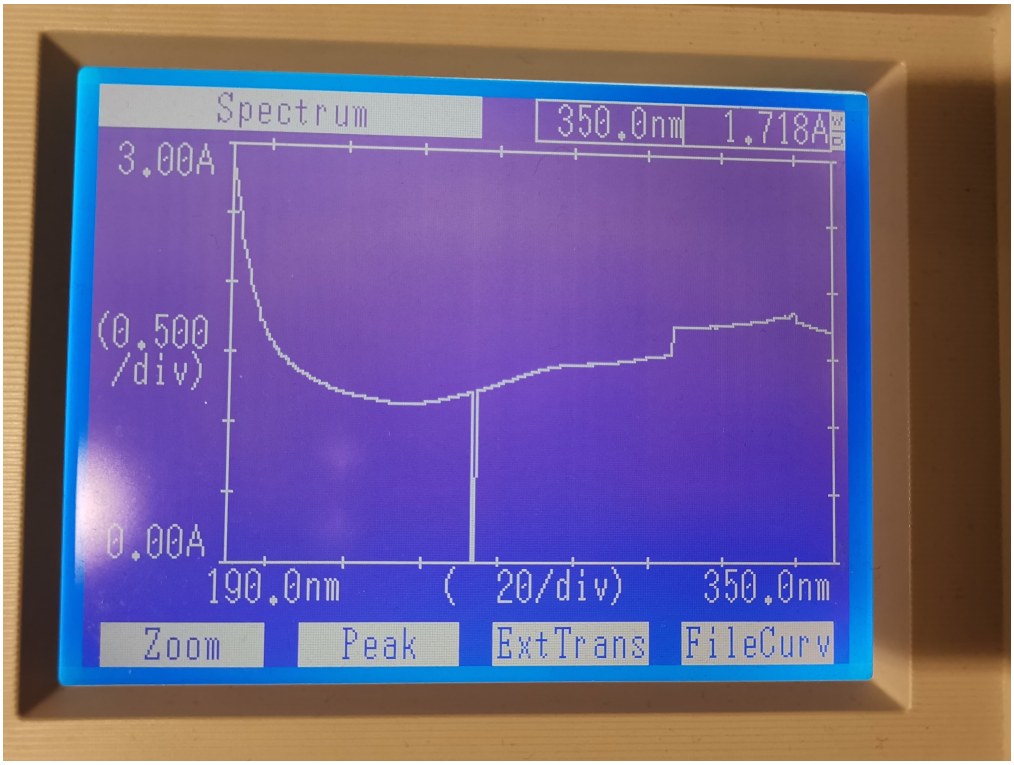

Figure B.5: UV scan of sample P5 from 190 nm to 350 nm.

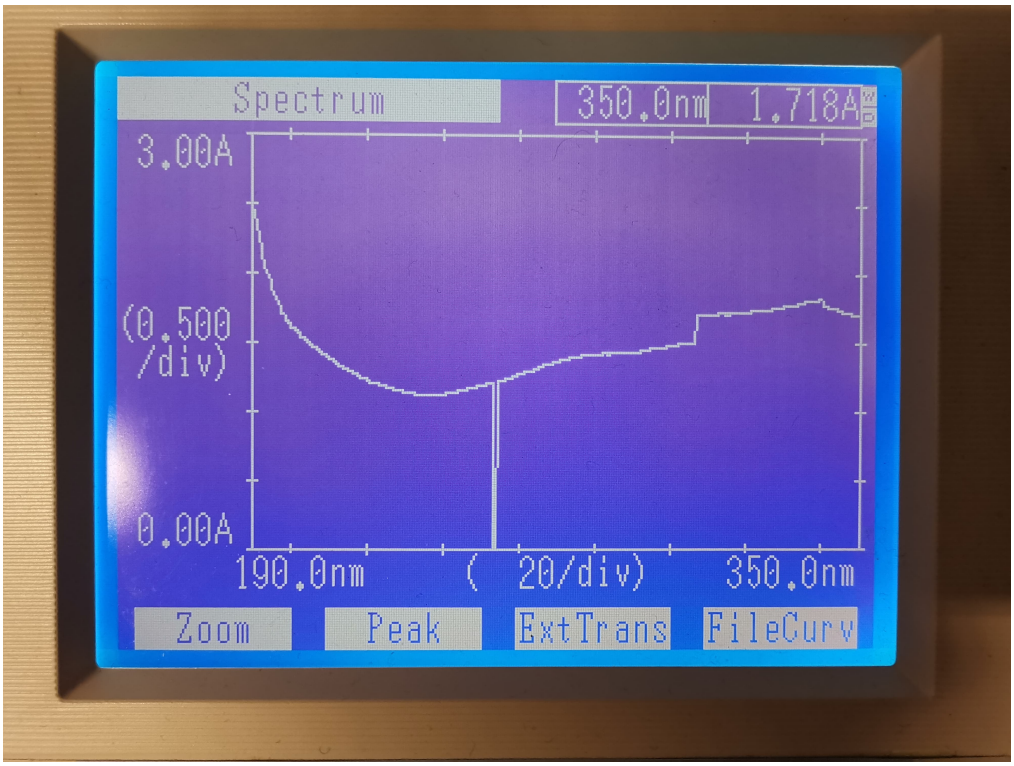

Figure B.6: UV scan of sample P6 from 190 nm to 350 nm.

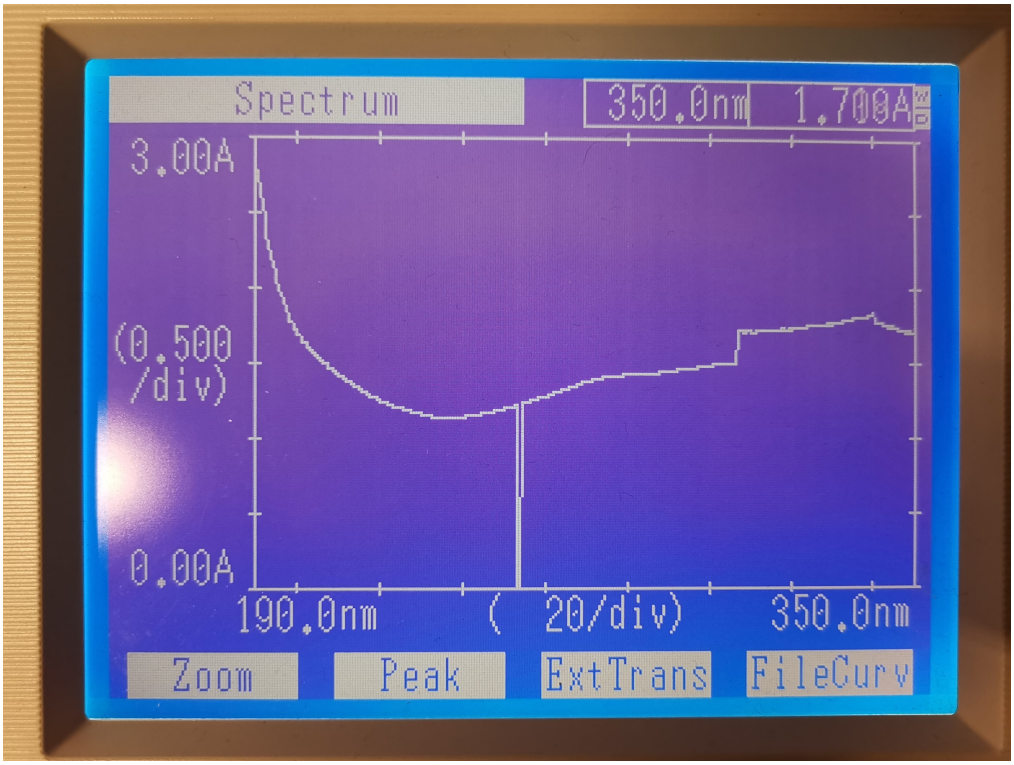

Figure B.7: UV scan of sample P7 from 190 nm to 350 nm.

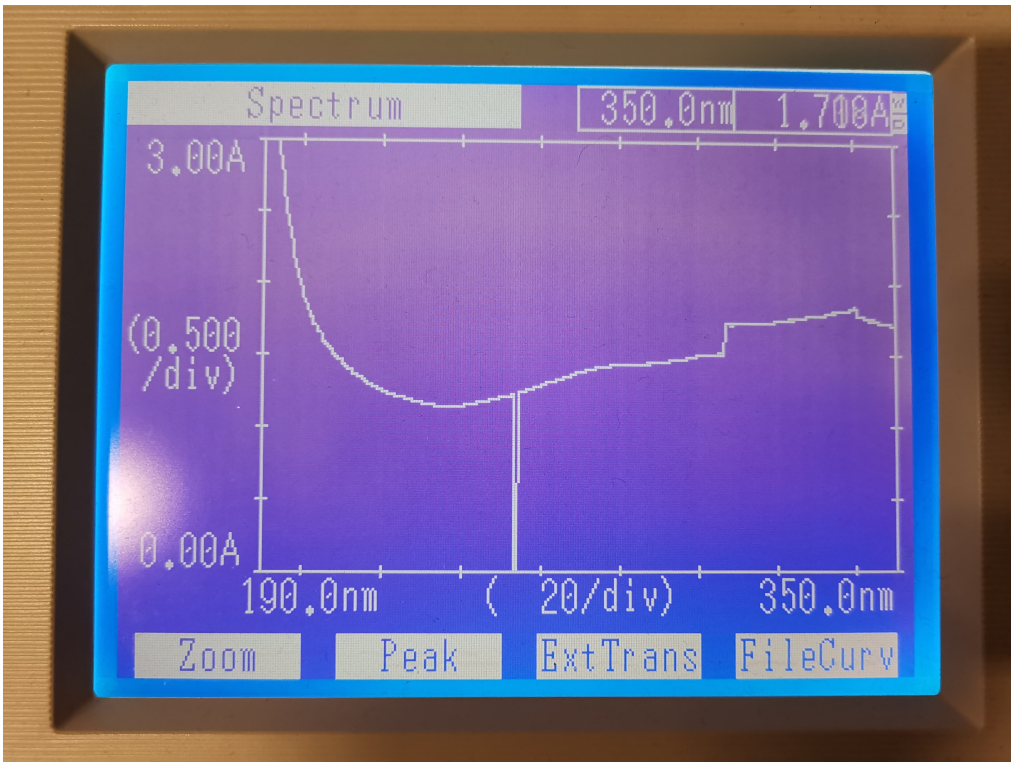

Figure B.8: UV scan of sample P8 from 190 nm to 350 nm.

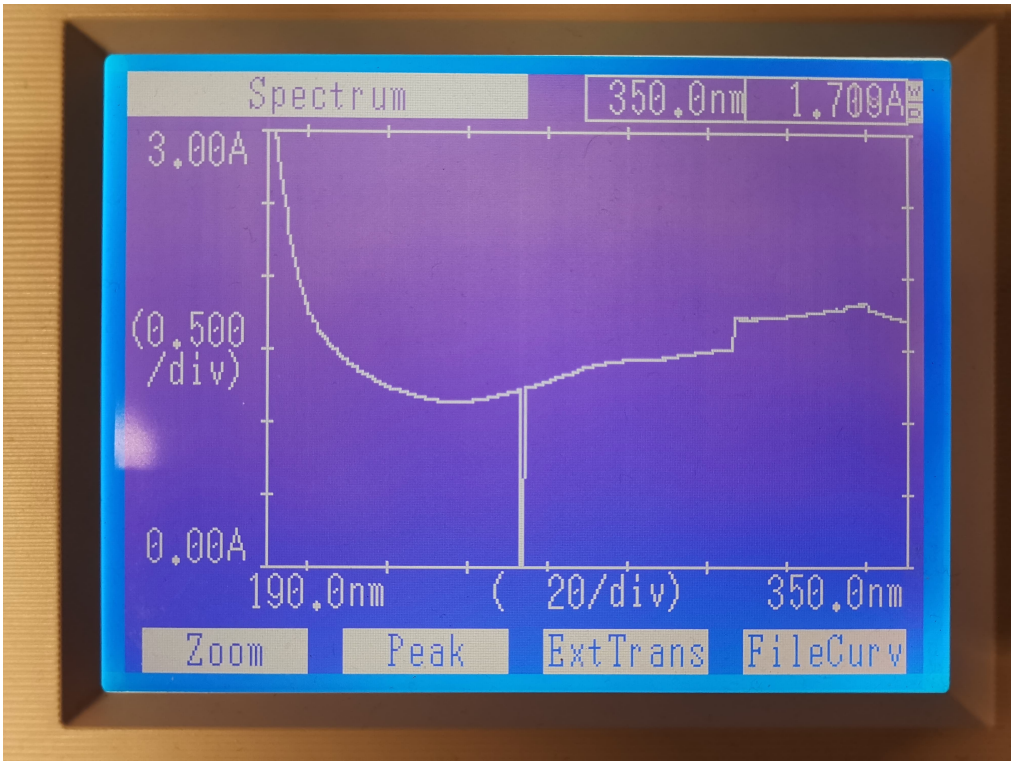

Figure B.9: UV scan of sample P9 from 190 nm to 350 nm.

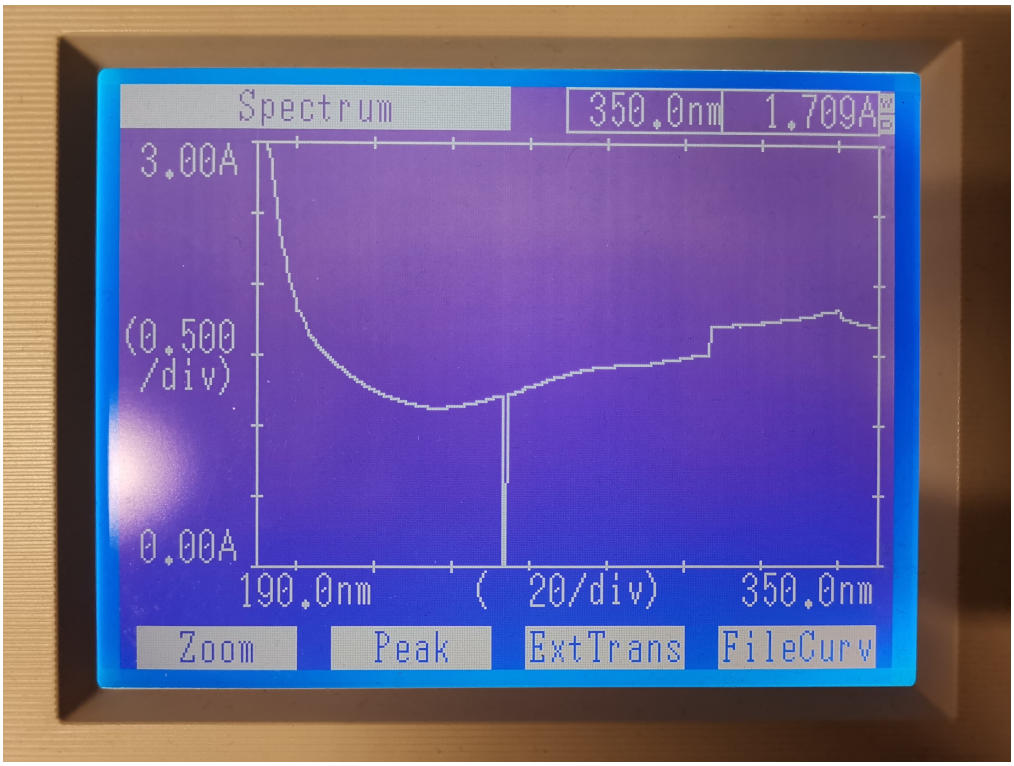

Figure B.10: UV scan of sample P10 from 190 nm to 350 nm.

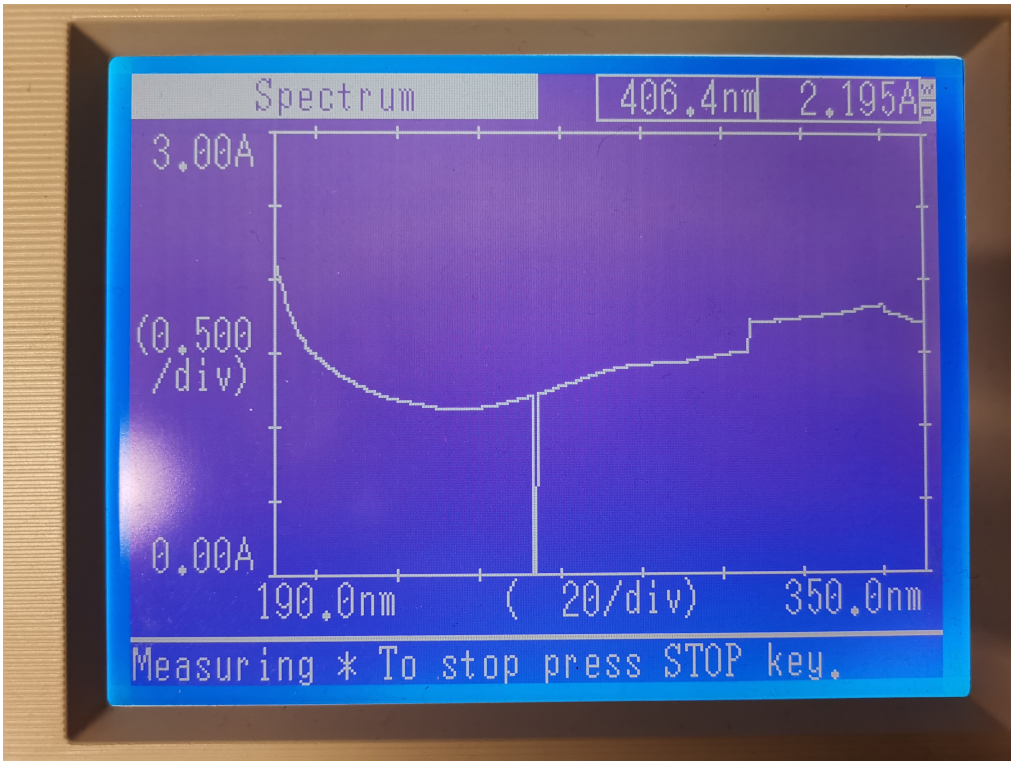

Figure B.11: UV scan of blank sample B1 from 190 nm to 350 nm.

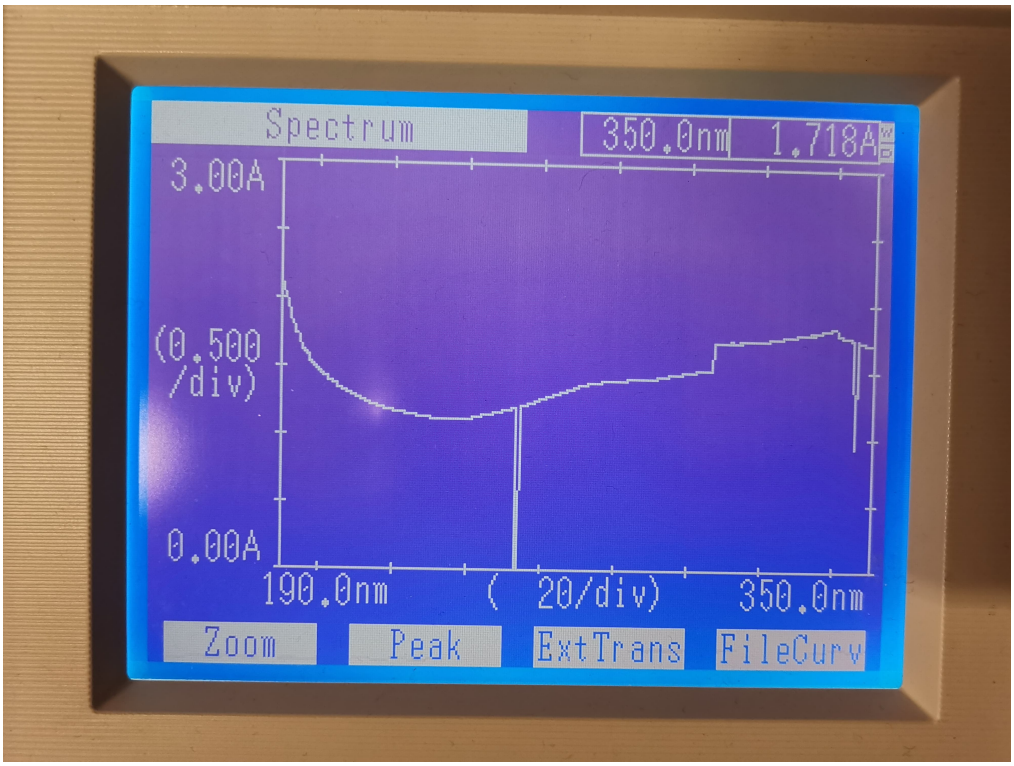

Figure B.12: UV scan of blank sample 2 from 190 nm to 350 nm.

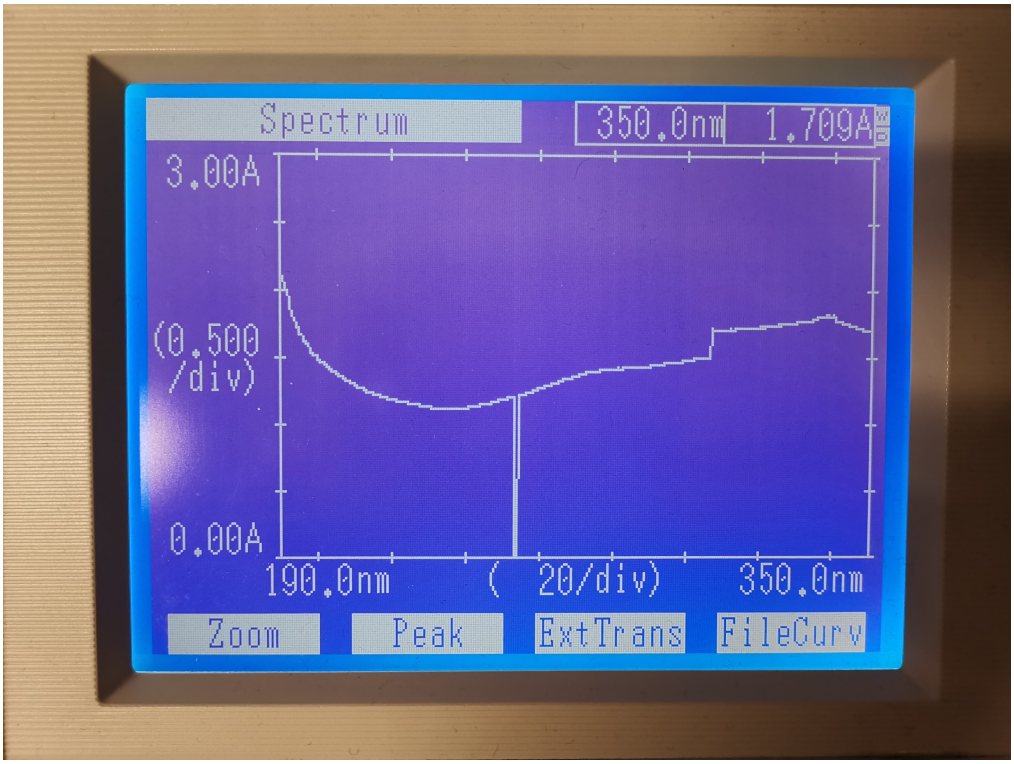

Figure B.13: UV scan of blank sample 3 from 190 nm to 350 nm.

B Ion Chromatography

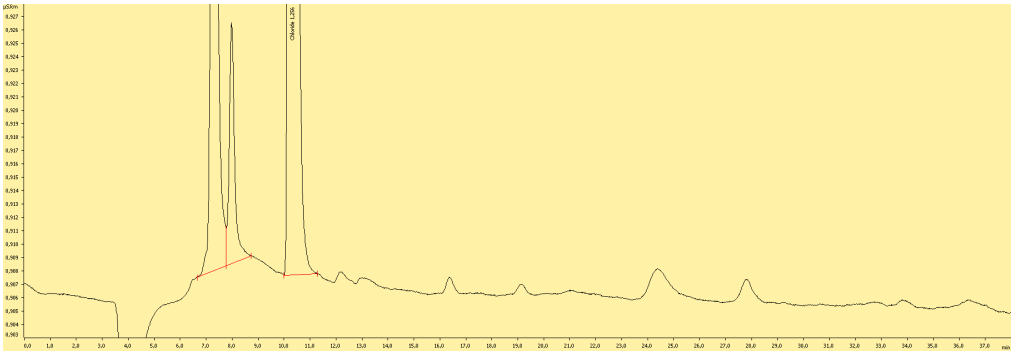

Figure B.14: Ion chromatogram for sample P1.

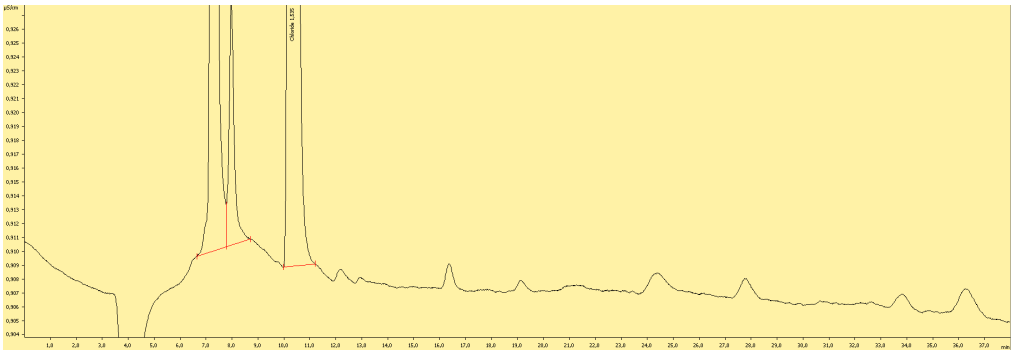

Figure B.15: Ion chromatogram for sample P2.

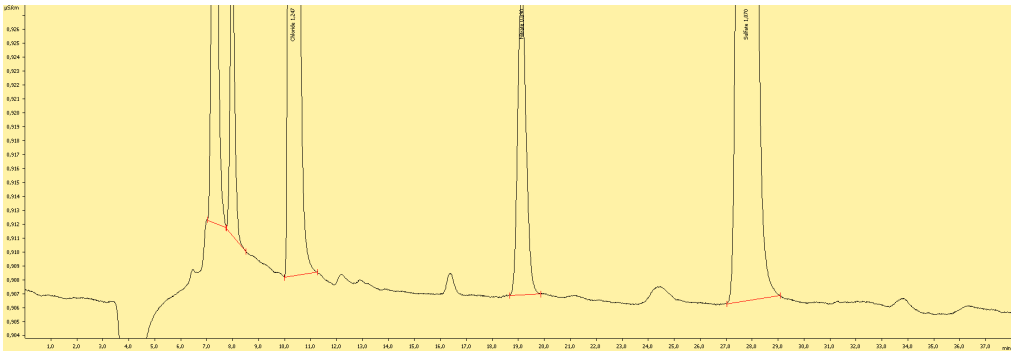

Figure B.16: Ion chromatogram for sample P3.

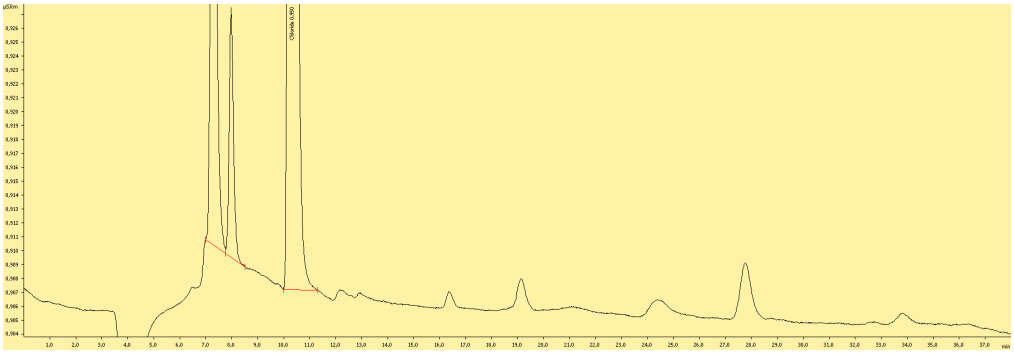

Figure B.17: Ion chromatogram for sample P4.

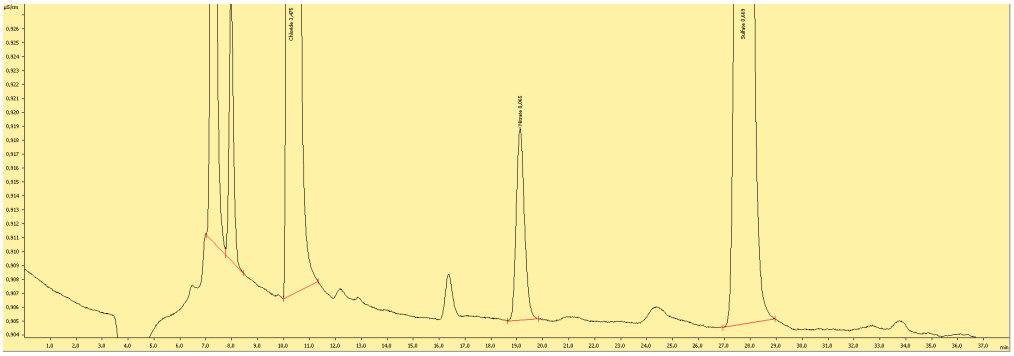

Figure B.18: Ion chromatogram for sample P5.

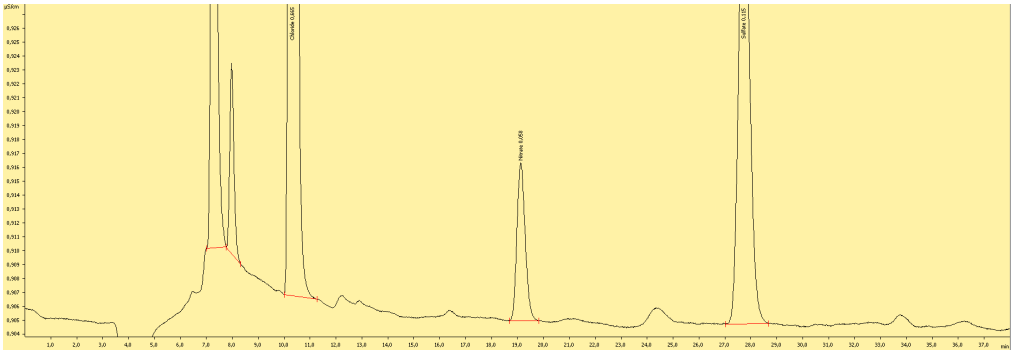

Figure B.19: Ion chromatogram for sample P6.

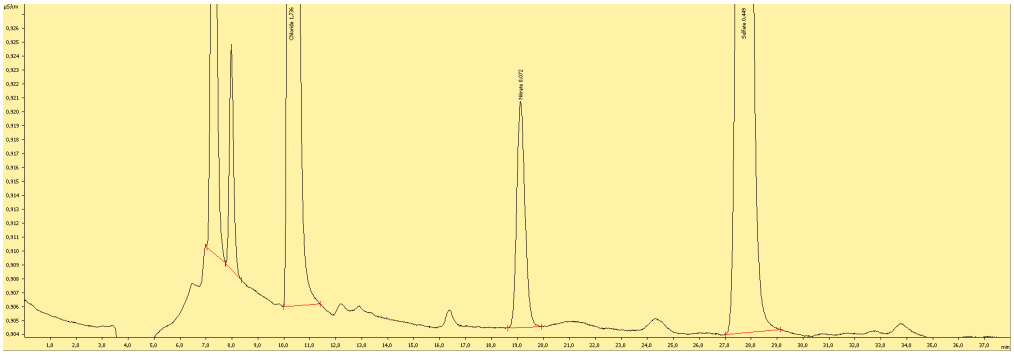

Figure B.20: Ion chromatogram for sample P7.

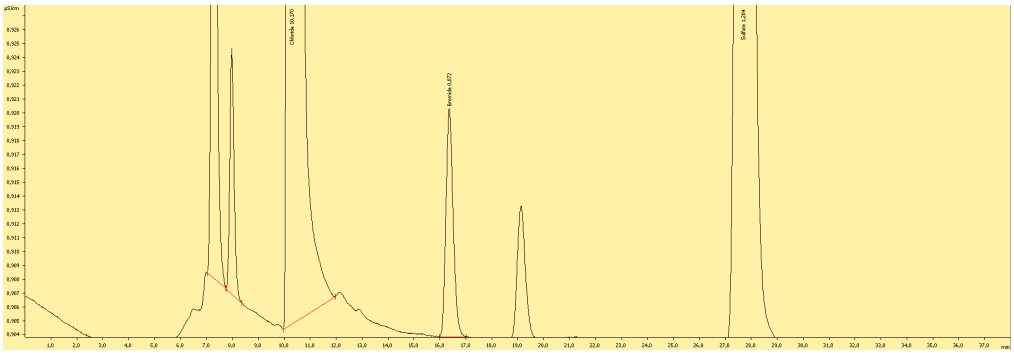

Figure B.21: Ion chromatogram for sample P8.

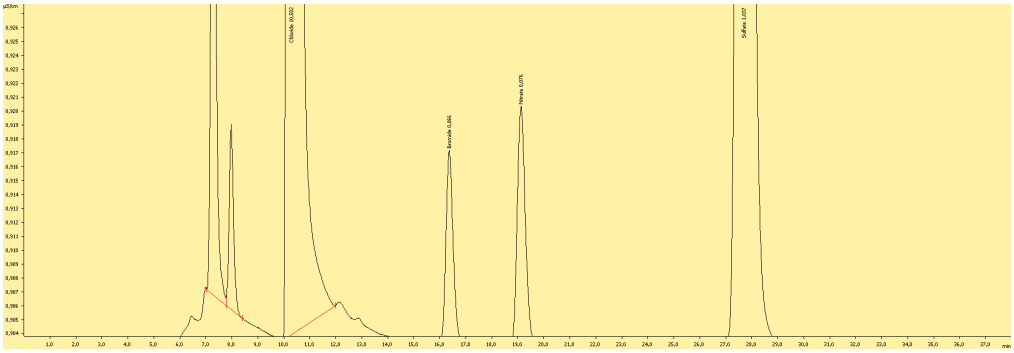

Figure B.22: Ion chromatogram for sample P9.

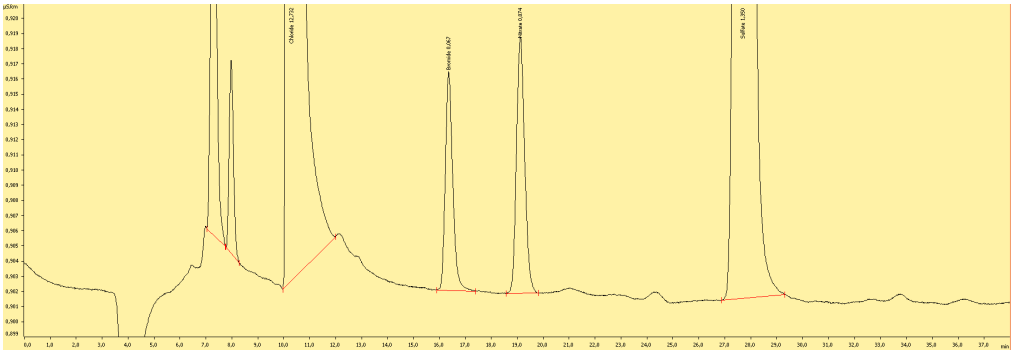

Figure B.23: Ion chromatogram for sample P10.

Table B.2: Ion concentration analysis by Ion Chromatography.

Sample	F^- [mg L^{-1}]	Cl^- [mg L^{-1}]	$NO_2{}^-$ [mg L^{-1}]	Br^- [mg L^{-1}]	$NO_3{}^-$ [mg L^{-1}]	$PO_4{}^{3-}$ [mg L^{-1}]	$SO_4{}^{2-}$ [mg L^{-1}]
P1	0.00	1.26	0.00	0.00	0.00	0.00	0.00
P2	0.00	1.54	0.00	0.00	0.00	0.00	0.00
P3	0.00	1.25	0.00	0.00	0.09	0.00	1.07
P4	0.00	0.95	0.00	0.00	0.00	0.00	0.00
P5	0.00	3.48	0.00	0.00	0.07	0.00	0.67
P6	0.00	0.67	0.00	0.00	0.06	0.00	0.12
P7	0.00	1.74	0.00	0.00	0.07	0.00	0.45
P8	0.00	12.74	0.00	0.07	0.00	0.00	1.20
P9	0.00	8.46	0.00	0.07	0.08	0.00	1.04
P10	0.00	6.51	0.00	0.07	0.07	0.00	1.35

C ICP-MS

Table B.3: Concentration summary of ICP-MS analysis of snow samples from Ny-Ålesund, November 2018. Reported as the mean concentration with one standard deviation ($N = 44$).

Element	Concentration [$\mu g\, L^{-1}$]	Element	Concentration [$\mu g\, L^{-1}$]
Li	0.0584 ± 0.0837	P	6.14 ± 5.01
B	0.355 ± 0.605	S	89 ± 172
Se	NDA	Cl	1390 ± 3050
Y	0.0083 ± 0.0283	K	32.2 ± 74.2
Cd	0.00109 ± 0.00149	Ca	158 ± 305
Mo	0.00516 ± 0.00358	V	0.0186 ± 0.0150
Sn	0.00254 ± 0.00319	Cr	0.0252 ± 0.0178
Cs	0.00126 ± 0.00278	Mn	0.58 ± 1.32
Ce	NDA	Fe	4.2 ± 10.9
Pr	NDA	Co	0.0144 ± 0.0185
W	0.000557 ± 0.000631	Ni	0.0405 ± 0.0589
Hg	0.00888 ± 0.00553	Cu	0.0607 ± 0.0635
Tl	0.000320 ± 0.000668	Zn	4.37 ± 2.93
Pb	0.0151 ± 0.0448	Sr	0.72 ± 1.53
Th	NDA	Ag	NDA
U	0.00088 ± 0.00235	Sb	0.2340 ± 0.00782
Na	806 ± 2020	Ba	0.391 ± 0.366
Mg	133 ± 314	As	0.0154 ± 0.0122
Al	3.48 ± 6.35	Br	4.98 ± 9.93
Si	28.0 ± 14.6		

Table B.4: Concentration summary of ICP-MS analysis of snow samples from Longyearbyen, January and February 2019. Reported as the mean concentration with one standard deviation ($N = 25$).

Element	Concentration [µg L^{-1}]	Element	Concentration [µg L^{-1}]
Li	NDA	P	12.5 ± 11.2
B	NDA	S	1150 ± 781
Se	0.261 ± 0.166	Cl	12800 ± 7440
Y	0.029 ± 0.117	K	438 ± 420
Cd	0.01100 ± 0.00653	Ca	788 ± 974
Mo	0.0399 ± 0.0581	V	0.124 ± 0.110
Sn	0.00946 ± 0.00904	Cr	0.0695 ± 0.0535
Cs	0.00328 ± 0.00267	Mn	6.02 ± 9.78
Ce	0.0298 ± 0.0958	Fe	5.79 ± 7.31
Pr	0.0047 ± 0.0147	Co	0.191 ± 0.418
W	0.0301 ± 0.0695	Ni	0.317 ± 0.681
Hg	0.00493 ± 0.00326	Cu	1.46 ± 2.87
Tl	0.00218 ± 0.00106	Zn	19.7 ± 20.3
Pb	0.160 ± 0.115	Sr	7.70 ± 7.19
Th	0.000900 ± 0.000685	Ag	NDA
U	0.00280 ± 0.00328	Sb	0.0906 ± 0.0494
Na	6930 ± 4010	Ba	2.69 ± 3.25
Mg	927 ± 622	As	0.131 ± 0.228
Al	12.9 ± 34.1	Br	41.8 ± 24.7
Si	43.5 ± 21.9		

Table B.5: Concentration summary of ICP-MS analysis of snow samples from Longyearbyen and Ny-Ålesund, March 2019. Reported as the mean concentration with one standard deviation ($N = 28$).

Element	Concentration [$\mu g\, L^{-1}$]	Element	Concentration [$\mu g\, L^{-1}$]
Li	0.385 ± 0.292	P	6.34 ± 5.39
B	6.71 ± 6.02	S	1440 ± 1160
Se	NDA	Cl	27100 ± 25100
Y	0.0149 ± 0.0311	K	548 ± 482
Cd	0.01350 ± 0.00793	Ca	732 ± 451
Mo	0.0302 ± 0.0249	V	0.091 ± 0.121
Sn	0.00782 ± 0.00533	Cr	0.069 ± 0.138
Cs	0.0068 ± 0.0114	Mn	2.16 ± 3.81
Ce	NDA	Fe	29.0 ± 85.1
Pr	NDA	Co	0.0446 ± 0.0768
W	0.00199 ± 0.00459	Ni	0.147 ± 0.328
Hg	0.00673 ± 0.00703	Cu	0.195 ± 0.251
Tl	0.00459 ± 0.00367	Zn	11.70 ± 9.48
Pb	0.354 ± 0.297	Sr	10.60 ± 8.75
Th	NDA	Ag	NDA
U	0.00474 ± 0.00466	Sb	0.0210 ± 0.0116
Na	14500 ± 13000	Ba	0.750 ± 0.624
Mg	1820 ± 1580	As	0.0871 ± 0.0738
Al	17.6 ± 50.2	Br	114.0 ± 94.9
Si	43.0 ± 95.9		

Table B.6: Concentration summary of ICP-MS analysis of snow samples from Ny-Ålesund, May 2017. Reported as the mean concentration with one standard deviation ($N = 39$).

Element	Concentration [µg L^{-1}]	Element	Concentration [µg L^{-1}]
Li	0.103 ± 0.166	P	5.43 ± 7.33
B	1.230 ± 0.918	S	514 ± 469
Se	0.0694 ± 0.0293	Cl	6780 ± 6470
Y	0.0264 ± 0.0868	K	232 ± 342
Cd	0.00724 ± 0.00424	Ca	526 ± 410
Mo	0.0103 ± 0.0144	V	0.143 ± 0.456
Sn	0.00460 ± 0.00480	Cr	0.134 ± 0.485
Cs	0.00760 ± 0.02610	Mn	6.6 ± 16.6
Ce	0.135 ± 0.502	Fe	57 ± 228
Pr	0.0152 ± 0.0550	Co	0.095 ± 0.250
W	0.00130 ± 0.00280	Ni	0.170 ± 0.403
Hg	0.00180 ± 0.000140	Cu	0.57 ± 1.01
Tl	0.00197 ± 0.00421	Zn	11.6 ± 15.4
Pb	0.144 ± 0.238	Sr	3.57 ± 2.76
Th	0.00637 ± 0.02630	Ag	0.083 ± 0.579
U	0.00437 ± 0.00815	Sb	0.0111 ± 0.0110
Na	3340 ± 3270	Ba	1.47 ± 2.26
Mg	498 ± 443	As	0.0386 ± 0.0522
Al	31 ± 119	Br	14.1 ± 16.8
Si	51 ± 175		

Table B.7: Quantification detection limits for ICP-MS analysis.

Element	Isotope	Resolution	Quantification detection limit [μg L^{-1}]
Al	27	Mr	0.20
Sb	121	Mr	0.0020
As	75	Hr	0.025
Ba	137	Mr	0.013
Be	9	Lr	0.0020
Bi	209	Lr	0.0010
B	11	Lr	0.050
Br	81	Hr	3.0
Cd	114	Lr	0.0020
Ca	44	Mr	2.0
Cl	35	Mr	100
Cr	53	Mr	0.0200
Co	59	Mr	0.0040
Cu	63	Mr	0.030
Fe	56	Mr	0.020
Pb	208	Lr	0.0020
Li	7	Lr	0.005
Mg	25	Mr	0.50
Mn	55	Mr	0.0060
Hg	202	Lr	0.0050
Mo	98	Mr	0.020
Ni	60	Mr	0.015
K	39	Mr	1.0
Se	82	Lr	0.05
Si	29	Mr	10.0
Na	23	Mr	10.0
Sr	88	Mr	0.025
S	32	Mr	5.0
S	34	Mr	20
Tl	205	Lr	0.0003
Sn	118	Lr	0.001
Ti	47	Mr	0.020
U	238	Lr	0.0003
V	51	Mr	0.0030
Zn	66	Mr	0.025

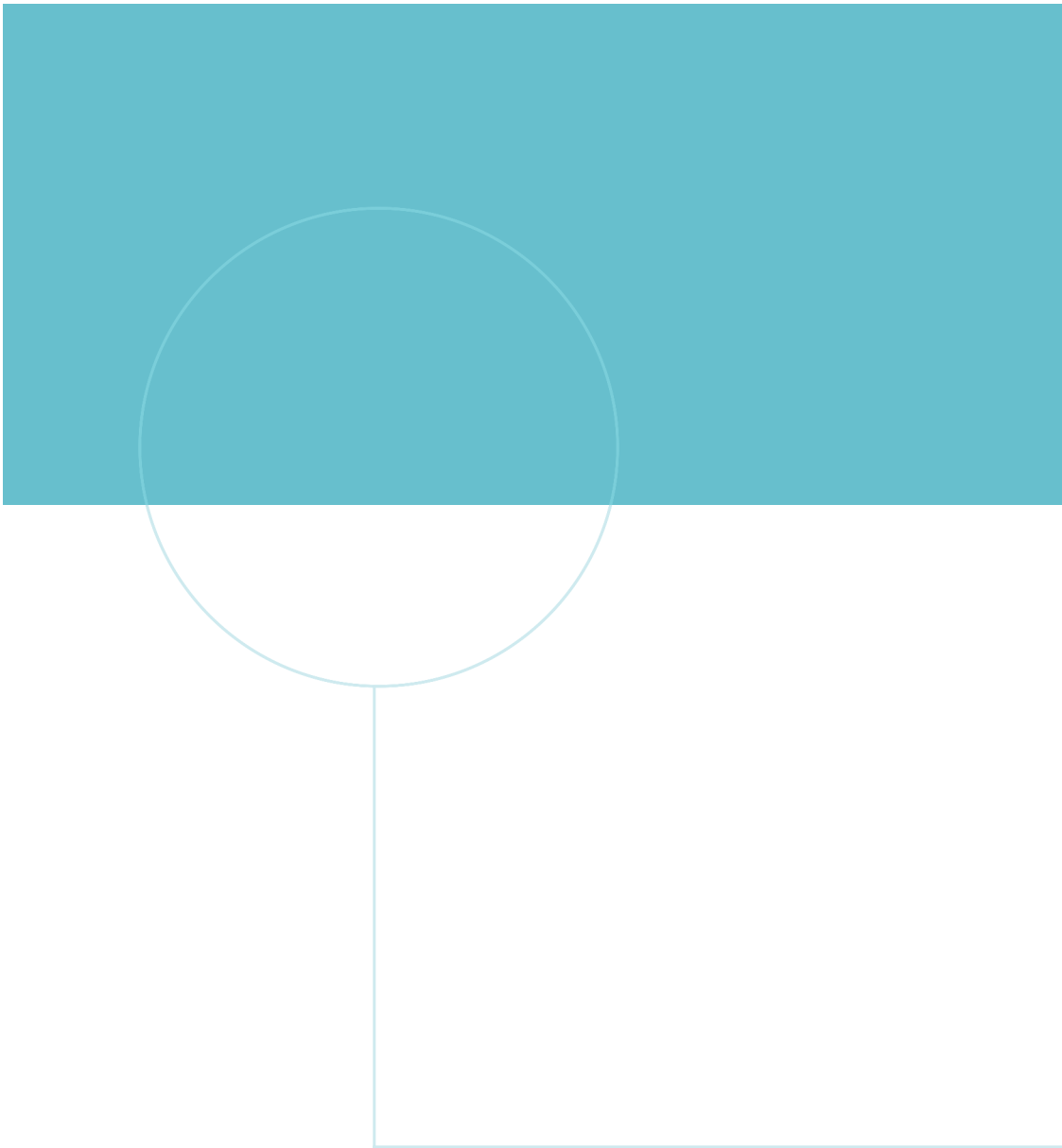

NTNU
Norwegian University of
Science and Technology

UNIS
The University Centre in Svalbard